Electroabsorption & Electrorefraction

in

InP/InAsP & GaAs/AlGaAs

Multiple Quantum Well

Waveguides

By

REZA MANI, MSc

A Thesis
Submitted to the school of graduate studies
for the degree of
Master of Engineering

McMaster University

February 1993

MASTER OF ENGINEERING(1993)
(Engineering Physics)

MCMASTER UNIVERSITY
Hamilton,Ontario

TITLE: Electroabsorption & Electrorefraction in Inp/InAsP & GaAs/AlGaAs multiple quantum well waveguides.

AUTHOR: Reza Mani, MSc. (Indian Institute of Technology, New Delhi, India).

SUPERVISOR: Dr. P.E. Jessop

NUMBER OF PAGES: 117

ABSTRACT

Electroabsorption and electrorefraction were studied in GaAs/AlGaAs and InP/InAsP multiple quantum well waveguides. Measurements of changes of the absorption coefficient and the refractive index with wavelength and bias voltage were made. Switching ratios of up to 18 dB were obtained for the GaAs/AlGaAs material. The Kramers-Kronig relation was used to calculate the theoretical phase shifts from the absorption coefficient data.

ACKNOWLEDGEMENTS

First of all, I would like to express my appreciation to my supervisor Dr.P.E.Jessop for his supervision and encouragement throughout this work.

Secondly, I would like to thank Doug Bruce (for processing the material and providing information), Mike Daly (for his useful discussions), Don Hargreaves (for his helpful information on wordperfect 5.1), and Bruce Takasaki (for reading my thesis and making helpful comments).

Finally I want to thank my uncle Fariborz Saheli and my friend Hossein Sharif for their support and encouragement.

TABLE OF CONTENTS

LIST OF FIGURES

LIST OF TABLES

CHAPTER 1

INTRODUCTION

1.1-Chapter Introduction

The focus of this thesis is on electroabsorption and electrorefraction effects in multiple quantum well waveguides. Upon the application of an electric field these two effects produce a change in the absorption coefficient and refractive index of the material, respectively. In a semiconductor they can be used as the basis for the operation of phase and intensity modulators which are needed in optical communications and related technologies.

1.2-Historical development

In order to understand the importance of phase and intensity modulators, one has to review the historical development of optical communication systems and the field of integrated optics. Modern interest in optical communications started with the invention of the laser in the early 1960's.

The laser is a source of monochromatic light with frequencies 10,000 times higher than frequencies used in radio communication systems. Since the information capacity of any communication system is directly proportional to the frequency of the carrier wave, lasers offer, in principle, an increase in bandwidth of four orders of magnitude and therefore, the information capacity increases substantially.

After realizing this potential of lasers, atmospheric communications began using laser beams as carrier waves and the atmosphere as the guiding medium. However, the dependence on clear atmosphere, the necessity of line of sight between the transmitter and the receiver, and the possibility of eye damage to anyone crossing the path of the laser light were some major drawbacks of this means of communication.

The development of low loss optical fibers in the 1970's was the solution to most of these problems. The invention of semiconductor lasers that are compact and compatible with fibers around the same time, finally made optical communications a feasible and efficient system. Present optical communication technology is capable of transmitting information at a rate of a few billion bits per second over hundreds of kilometers through optical fibers with a negligible error rate[5]. This huge capacity makes optical communications probably the most important means of communication for the future.

1.3-Phase and Intensity modulators

In order to impose the information on the laser carrier frequency, one can directly modulate the semiconductor laser, or alternatively use an external modulation scheme. Direct modulation of lasers has certain disadvantages which make external modulation preferable. First, there are degrading effects on the laser linewidth and stability. Secondly, certain modulation schemes such as phase modulation are not effectively feasible through direct modulation[1]. External modulation of the carrier wave makes these modulation schemes much more feasible. Phase and intensity modulation, both analog and digital, are two modulation schemes that can be accomplished by external modulation. An optical waveguide geometry is usually preferred for these modulators due to compatibility with fibers and more efficient modulation.

Different types of phase and intensity modulators exist as will be explained in detail in chapter 3. For intensity modulators, these include electroabsorption modulators[4] and the class of intensity modulators that rely on changes of refractive index, e.g, Mach-Zehnder and directional coupler types[5].

For phase modulators, there are several physical effects that can be employed for their principle of operation. These are electrooptic effect, electrorefraction, band filling and plasma effects [8]. The first two are field related effects and the last two are carrier related effects. Since both the materials which were used in the work described in this thesis had a p-i-n structure, the carrier related effects are insignificant and only the field related effects cause the observed phase shift (Refer to chapter 2).

1.4-Object of thesis

This thesis reports on an experimental investigation of electrorefraction and electroabsorption in two materials which are GaAs/AlGaAs and Inp/InAsP multiple quantum well waveguides. The second material is strained due to the lattice mismatch between InP and InAsP.

Several measurements were taken from these materials. The photocurrent and transmission measurements were taken simultaneously and data obtained shows consistency in the band edge shift due to application of an electric field. Phase shift measurements were taken for both forward and reverse bias. Both DC and pulsed methods of operation were employed to distinguish between thermally induced phase shifts and genuine electrorefraction effects.

The information obtained from these measurements is widely applicable to many devices, such as modulators, switches, phase shifters, detectors and even lasers. For the phase shift measurements, the method used involved beating the waveguided beam with a frequency shifted beam produced by an acousto-optic modulator. The optical phase shift in the waveguided beam is converted to an rf phase shift in the beat signal. This is not only a convenient way to measure the phase shift but it also relates directly to an important application, which is the use of optical methods for phased array microwave antennas[20].

1.5-Outline of thesis

In chapter 2, first the different physical effects which change Δn are described fully followed by the Franz-Keldysh effect, Quantum well theory and Quantum Confined Stark effect.

Afterwards, the Kramers-Kronig relation which calculates changes of refractive index from absorption coefficient change, and also the phase shift expected under forward bias are considered. Chapter 3 reviews various phase and intensity modulation schemes and the phased array radar application. Chapter 4 is the description of the experimental set-up and chapter 5 contains the results and discussion of the obtained data and a comparison to theoretical calculations, followed by conclusions.

CHAPTER 2

PHYSICAL EFFECTS

2.1-Chapter Introduction

In this chapter, the physical mechanisms which cause a change of index of refraction or absorption coefficient in a semiconductor device are discussed. The basic quantum well theory and the difference between the effects of two orthogonal polarizations, i.e, TE and TM, on the location of the absorption edge are also considered. The Kramers-Kronig relation, which relates the change of absorption coefficient to change of index, is a theoretical check on the experimental results of phase shift measurements and will be described.

2.2-Physical mechanisms responsible for Δn

There are basically four physical mechanisms by which the refractive index can change upon the application of an electric field. These are a) electrooptic effect b) electro-refraction c) band filling d) plasma effect[8].

All these effects exist in semiconductor materials and depending on the wavelength of operation, they have different degrees of strength. Electrooptic effect is also present in some insulating crystals such as $LiNbO_3$, KDP(potassium dihydrogen phosphate), etc, but the other three effects are exclusive to semiconductor materials.

A complete theory that describes these effects is necessary to design more efficient modulators and switches which are major components of integrated optical devices [8]. Each of these effects is described in detail and the relative strength of each one is considered. A few examples of the state of the art devices using these effects are also mentioned. In the case of the electrooptic effect, both GaAs and $LiNbO_3$ will be considered.

2.2.1- Electrooptic effect

The electrooptic effect is present in a certain class of crystals that do not possess an inversion symmetry. In general, the application of the field can alter the birefringence property of these crystals or can induce birefringence in an otherwise isotropic crystal. If the change of index is proportional to the electric field, it is called Pockel's effect and if it is proportional to the square of the field it is termed the Kerr effect. If both of these effects are present in a material the net index change would be the sum of the quadratic and linear terms. Since the magnitude of the kerr effect is much smaller than the Pockel's effect, it is neglected and only the linear term is considered. The propagation of light through the anisotropic media and the index changes by the electrooptic effect, are most conveniently described by introducing the concept of the index ellipsoid [2]. The index ellipsoid is a football shape geometrical figure, use of which, will allow one to find the indices of refraction for a wave propagating along an arbitrary direction in the crystal. For any anisotropic medium, the plane perpendicular to the direction of propagation and passing through the center will subtend an ellipse with the ellipsoid. The minor and major axes of this ellipse will define the ordinary and extraordinary index of refraction. The equation of the index ellipsoid, when the crystallographic axes are chosen as the principal axes, is given by

$$\frac{x^2}{n_x^2}+\frac{y^2}{n_y^2}+\frac{z^2}{n_z^2}=1 \tag{2.1}$$

For a uniaxial crystal, equation 1 changes to

$$\frac{x^2}{n_o^2}+\frac{y^2}{n_o^2}+\frac{z^2}{n_e^2}=1 \qquad (2.2)$$

where n_o and n_e are referred to as the ordinary and extraordinary indices of refraction.

When an electric field is applied to the electro-optic crystal, changes will be induced in the index ellipsoid and equation 2.2 will transform to a new equation which is given by

$$\frac{x^2}{n_1^2}+\frac{y^2}{n_2^2}+\frac{z^2}{n_3^2}+2\frac{yz}{n_4^2}+2\frac{xz}{n_5^2}+2\frac{xy}{n_6^2}=1 \qquad (2.3)$$

This equation shows us that x,y,z are no longer the principal axes and therefore index changes are induced in the crystal which can be described in a tensor form as

$$\Delta\left(\frac{1}{n_i^2}\right)=\sum_{i=1}^{3} r_{ij}E_j \qquad (2.4)$$

where r_{ij} is the electrooptic tensor and E_j is the component of the electric field.

The r_{ij} tensor is a 6x3 tensor. Some of its elements are zero and some of the other elements are equal or opposite in sign as a result of crystal symmetry consideration. Hence for materials of practical interest, there is only one or a few non-vanishing elements. Here, the electro-optic effect is examined in two crystals, $LiNbo_3$ and GaAs.

$LiNbO_3$ is a negative uniaxial crystal. The only non zero elements of the electrooptic tensor are r_{22}, $r_{13,}r_{51}$ and r_{33}. Its largest e.o coefficient is r_{33} whose magnitude is 30.9×10^{-12} m/v [2]. Hence to get maximum refractive index change one makes use of this coefficient. Electrooptic modulators based on $LiNbo_3$ are very fast and efficient.

GaAs belongs to the zincblende class of crystals. It is an optically isotropic crystal at zero field, but upon the application of an electric field, a birefringence is induced in it.

The equation of the index ellipsoid in the presence of the field is

$$\frac{1}{n_o^2}(x^2+y^2+z^2)+2r_{41}(E_x yz+E_y xz+E_z xy)=1 \tag{2.5}$$

With zero field applied, the ellipsoid is a sphere and the principal axes are the same as the crystal axes. With the application of a field the sphere changes to an ellipsoid and the principal axes are no longer the crystal axes. As a result of this change, index changes will be induced which are given by

$$n_{x'}=n_o-\frac{n_o^3}{2}r_{41}E_z \tag{2.6}$$

$$n_{y'}=n_o+\frac{n_o^3}{2}r_{41}E_z \tag{2.7}$$

The orientation of x′,y′ axes are at 45° with respect to the original axes. For GaAs, (100) substrates are often used and the cleavage planes are (110) and $(1\bar{1}0)$.

The value of r_{41}, the only non-vanishing element of the electrooptic tensor is given by 1.1×10^{-12} m/v [2].

For one of the materials which were used in our experiment (GaAs/AlGaAs,MQW) the electrooptic normalized phase shift was calculated. The material parameters used for this calculation were, wavelength $\lambda=.9$ μm, refractive index $n_0=3.6$, electrooptic coefficient $r_{41}=1.1\times10^{-12}$ and depletion region width $d=.538\mu$m.

Using the following formula, the normalized phase shift was calculated

$$\Delta\Phi/v.mm=\frac{\pi}{\lambda d}n_o^3 r_{41} \tag{2.8}$$

The value of the normalized phase shift was found to be 19°/v.mm.

Electrooptic effect is weaker in GaAs than in $LiNbO_3$, as indicated by a 6 to 1 advantage in the electrooptic figure of merit for the latter[7].

But on the other hand, for integrated optics applications GaAs based materials are more suitable due to the possibility of monolithic integration with lasers[19].

2.2.2- Electrorefraction

The second important field related effect which was mentioned is electrorefraction and it exists in III-V compounds such as GaAs and InP.

As mentioned in the previous section, the linear electro-optic effect is also present in III-V compounds but the size of this effect is relatively small. The electrorefractive effect, under certain conditions is much stronger than the Pockel's effect and can be utilized to obtain larger phase shifts. For example, when the wavelength of operation is close to the bandedge, this effect can produce larger phase shifts than the electrooptic effect. The relative sizes of the two effects will be discussed in section 2.3.

Electrorefraction is an accompanying effect to electro-absorption whenever the latter occurs. The complex refractive index has a real part, the refractive index n, and an imaginary part k which is related to the absorption coefficient α by the relation $\alpha=4\pi k/\lambda$. The change in the imaginary part of the complex refractive index will cause a change in the real part, and hence changes in the absorption coefficient $\Delta\alpha$ will be accompanied by changes in the refractive index Δn.

This relation is expressed in terms of the Kramers-Kronig relation given by [8]

$$\Delta n(E) = \frac{hc}{\pi}\int_0^\infty \frac{\Delta\alpha(\acute{E})}{(\acute{E}^2-E^2)}d\acute{E} \qquad (2.9)$$

where E is the energy.

The changes of the absorption coefficient due to the applied field, both in bulk and quantum well materials (Franz-Keldysh and quantum confined Stark effects) will be described in the following sections of this chapter. It is only necessary to point out that use of quantum well materials causes a much larger change in the absorption coefficient than the bulk material (upto 50 times) [19] which leads to greater index changes for the same applied field.

The magnitude of the index change due to electrorefraction is wavelength dependent. If the wavelength of operation is close to the bandedge it is much larger and when it is farther away it becomes relatively smaller. But to make efficient phase modulators, it is not only critical to have large index changes but it is also important to have small absorption. Moving closer to the band edge will increase both index and absorption change. Hence, another figure of merit has been defined for the phase modulators which is the ratio of the index change to absorption change $\Delta n/\Delta k$, where n and k were defined before. To find the best operating wavelength for the phase modulator, one has to optimize both Δn and $\Delta n/\Delta k$ which guarantees small absorption and large index change.

2.2.3-Band filling effect

This effect is due to the removal of carriers in the depletion region. The presence of the free carriers in a doped region will have a negative contribution to the refractive index as given by [21]

$$\Delta n=-\frac{e^2\lambda^2}{8\pi^2c^2n\epsilon_\circ}\frac{N}{m^*} \qquad (2.10)$$

Where N is the free carrier density.

Whenever a reverse bias is applied to a p-n junction, the carriers are removed from the depletion region, and as a result the absorption coefficient of the depletion region will change. The fundamental absorption edge will shift to lower energies causing a positive change in $\Delta\alpha$. This positive variation in $\Delta\alpha$ causes a positive change in the refractive index through the Kramers-Kronig relation.

For the materials used in this project, the depletion region is the intrinsic region of a p-i-n diode and therefore its carrier concentration is relatively small compared to a doped region. Since the magnitude of the band-filling effect is directly proportional to the number of free carries in the depletion region, this effect will have a negligible contribution. In order to prove the above statement, we refer to an approximate expression[8] which is used to calculate the index change due to the band-filling effect and calculate the index change for one of the materials used for the thesis research(GaAs/AlGaAs,MQW).

This expression is given by

$$\Delta n(BF) \approx B(\lambda)N \tag{2.11}$$

where N is the free carrier density and B(λ) is the proportionality constant which is wavelength dependent.

For a wavelength of .9μm the value of B(λ) is $1.5\times10^{-20}/cm^3$ [8] and approximating the carrier concentration of the intrinsic region to be equal to that of GaAs($2\times10^6/cm^3$) we find that the value of Δn is calculated to be 3×10^{-14}. This index change will cause negligible phase shifts and hence the bandfilling effect is ignored.

2.2.4- Plasma effect

Plasma effect is due to the intraband absorption of free carriers and finds its importance at longer wavelengths where the energy of the absorbed photon is small. Free carrier absorption will induce a corresponding index variation Δn.

An approximate expression for index change in the n doped GaAs due to the contribution of the intraband electron absorption in the conduction band is given by[8]

$$\Delta n_{n\text{-}GaAs}(intra) \approx 9.6\times10^{-21}\frac{N}{nE^2} \tag{2.12}$$

where E is the photon energy and n is the refractive index.

For p type material this expression changes to [8]

$$\Delta n_{p_{GaAs}}(intra) \approx 1.8\times10^{-21}\frac{P}{nE^2} \qquad (2.13)$$

Once again we calculate the contribution of this effect to the index change for one of the materials used (GaAs/AlGaAs MQW) and prove that it has negligible contribution. As stated before, the waveguiding region of this material is the intrinsic region of a p-i-n diode. Using the intrinsic carrier concentration of GaAs($2x10^6/cm^3$), a refractive index value of 3.558 (this index is the weighted average of the MQW region), and a photon energy of 1.43eV corresponding to a photon wavelength of .9μm and substituting in equation 2-12, the value of Δn is calculated to be $2.63x10^{-12}$. This small index change causes a negligible phase shift and is ignored.

2.3-Comparison of magnitude of the physical effects

In the previous sections, all the physical effects which change Δn were described. It was found that since the waveguiding region of the material used for thesis research (MBE#856,GaAs/AlGaAs,MQW) was made of an intrinsic material, the band-filling and plasma effects have negligible contributions to the index change and hence the normalized phase shift. The electrooptic normalized phase shift was calculated to be 19°/v.mm. The electro-refractive normalized phase shifts will be calculated in chapter 5 and will be compared to the size of the electro-optic effect.

In order to compare the magnitudes of these physical effects, we refer to a structure used by Mendoza-Alvarez[8]. This structure was a N-AlGaAs/n-GaAs/P-AlGaAs waveguide modulator with $3x10^{17}/cm^3$ doping of the n-GaAs waveguiding region, 100μm length and 0.25μm depletion region width.

We now examine the effect of the operating wavelength on the relative contributions of these four effects. As the wavelength approaches the bandgap, the relative contribution of the four effects will change but all contributions have the same sign for any operating wavelength. For a wavelength of λ=1.06 μm, the percentage contribution to Δn is as follows;LEO(linear electrooptic effect)=46%, ER=14%, PL=12%,BF=28%. This wavelength is relatively far from the bandgap and hence the LEO is stronger than the other effects.

For a wavelength of .9 μm which is closer to the bandgap, the individual contributions will change to LEO=21%, ER=27%, PL=4%,BF=48%. This is due to the fact that the ER effect increases substantially at wavelenghts close to the bandedge.

Hence using these observations, the wavelength dependence of the physical effects which change the refractive index was demonstrated.

2.4- Franz-Keldysh Effect

The Franz-Keldysh effect is responsible for the operation of the electro-absorption modulators described in chapter 3.

Whenever a strong electric field is applied to a semi-conductor, its absorption edge shifts to longer wavelengths. Because of the steepness of the absorption edge in a direct bandgap material such as GaAs, very large changes in the absorption of wavelength near the band edge can be produced by application of electric field. As an example, the absorption coefficient of GaAs under the presence of a field of 1.3×10^5 V/cm and for a wavelength of 9000 Å increases from $25 cm^{-1}$ to 10^4 cm^{-1} [4].

The mechanism responsible for Franz-Keldysh effect can be described directly by referring to the energy band diagram. Fig(2.1.a) shows the band diagram in the absence of the field. In this case the bands are flat and a photon can be absorbed only if it has enough energy to lift the electron across the bandgap. Fig(2.1.b) shows the band diagram in the presence of the field and as seen bands are tilted. In this case a transition can occur in which a photon energy is sufficient to lift the electron partly across the gap. Ordinarily such a transition could not occur because there would be no allowed

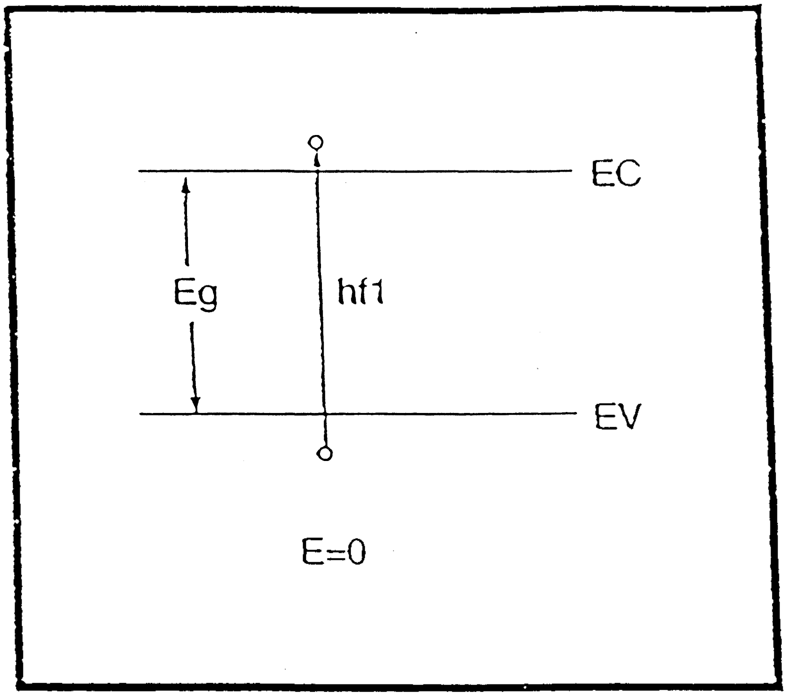

FIG 2.1.a The energy level diagram for E=0

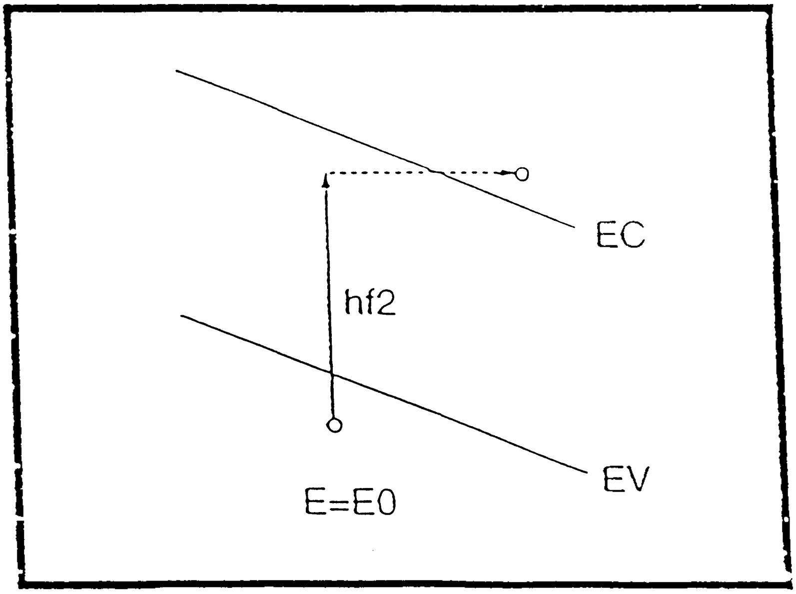

FIG 2.1.b The energy level diagram for E=E0

electron states within the bandgap. However, the electric field effectively broadens the states of the conduction band so that there is a finite probability to find the electron within the gap. This in turn increases the probability of tunnelling, reduces the effective bandgap of the material and hence the absorption edge is shifted to longer wavelength. It can be shown that the effective change in bandgap energy ΔE is given by [4]

$$\Delta E=\frac{3}{2}(m^{*})^{-\frac{1}{3}}\left(\frac{qh\xi}{2\pi}\right)^{\frac{2}{3}} \tag{2.14}$$

where ξ is the electric field.

Since ΔE depends on the electric field strength and since α is a very strong function of ΔE, a very effective electro-absorption modulator can be made for light whose wavelength is in the vicinity of the bandgap wavelength [16].

2.5-Quantum Well Theory

Recent techniques for depositing epitaxial layers such as MBE have made it possible to make very thin layers of semiconductor materials deposited on top of each other.

When a thin layer of a small bandgap material is sandwiched between two layers of large bandgap materials, a quantum well is formed. Since the carriers are confined in the well, they can have only discrete energy levels or eigen-values which are found by solving the finite potential well Schördinger equation. Solving the eigenvalue equation will yield a zero point energy solution for both valence band and conduction band which is purely a quantum mechanical result. This carrier confinement will also create a two dimensional density of states [19].

When a photon of suitable energy is supplied to the quantum well, the electrons make a transition from the valence to the conduction band and an electron-hole pair is formed which is called an exciton. The photon energy associated with the exciton absorption is given by

$$E_a = E_g + E_{e1} + E_{h1} - B \tag{2.15}$$

where E_g is the bandgap energy, E_{e1} is the zero point energy of the electron in the conduction band, E_{h1} is the zero point energy of holes in the valence band, B is the binding energy of the exciton, and E_a is the absorbed energy. For quantum well materials this binding energy is large enough so that room temperature excitons can exist. In the bulk materials these excitons are easily dissociated by thermal phonons.

For obtaining a larger interaction length, the MQW modulators are used in a waveguide geometry. The absorption of light in this geometry is polarization dependent. For TE light the electric field is parallel to the plane of the waveguide. The selection rules will allow both the heavy and light hole transitions [19]. On the other hand, for the TM polarization the electric field is perpendicular to the plane of the waveguide and only the light hole transitions are allowed. Since the lowest energy light hole transition is at a higher energy than the corresponding hh transition, the transmission spectra will show a red shift for TE with respect to TM. This difference is obvious in the experimental results of transmission measurements in chapter 5.

2.6-Quantum Confined Stark Effect

This effect is analogous to the Franz-Keldysh effect but happens in quantum well materials. Fig 2.2.a shows the wavefunctions of conduction and valence bands with zero field. The zero point energies are visible for both bands and the wavefunctions are symmetric.

Fig 2.2.b depicts the bands as an electric field is applied perpendicular to the plane of the layers. The band edges are tilted due to the application of the field and the wavefunctions are displaced from their original positions as seen in the figure[19]. The zero point energies are reduced and therefore the effective bandgap of the material will be lowered. This causes a shift of the absorption edge to

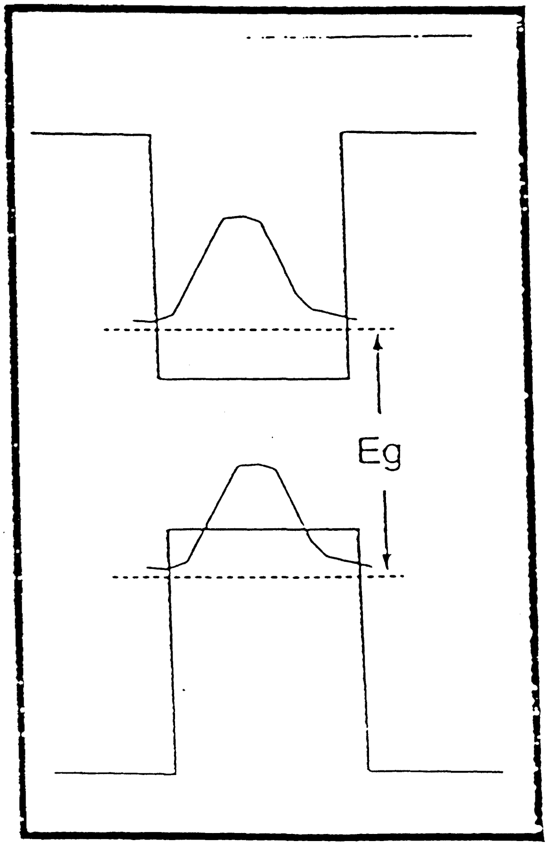

FIG 2.2.a-Band diagram for E=0

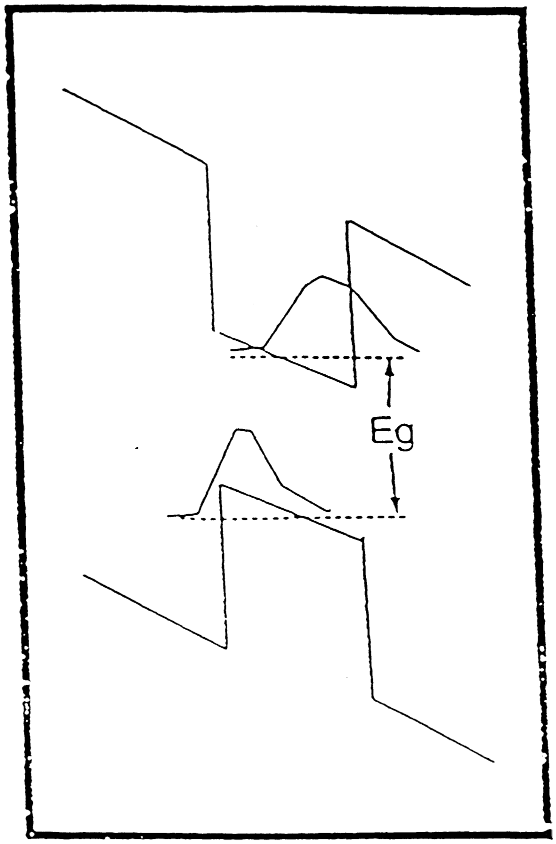

Fig 2.2.b-Band diagram for $E=E_{\ell}$

longer wavelengths.

The steepness of the absorption edge for quantum well materials causes an absorption coefficient change $\Delta\alpha$ which is typically 50 times larger than in bulk material[19]. This is an advantage for quantum wells since it gives better control and lower operating voltages for electroabsorption modulators. Again, the change of the absorption coefficient will give rise to a change in the index of refraction that must be larger than in bulk materials[14].

2.7-Kramers-Kronig relation

This relation was already given by equation 2.9, but in that equation the variable of integration was energy. In terms of frequency this relation is given by

$$\Delta n=\frac{c}{\pi}\int_{0}^{\infty}\frac{\Delta\alpha(\nu')\,d\nu'}{\nu'^{2}-\nu^{2}} \qquad (2.16)$$

but $\nu=c/\lambda$ and hence $d\nu=-c/\lambda^{2}d\lambda$.

Therefore changing the variable of integration from ν' to λ' we get

$$\Delta n=\frac{1}{\pi}\int_{0}^{\infty}\frac{\lambda^{2}\Delta\alpha(\lambda')\,d\lambda'}{\lambda^{2}-\lambda'^{2}} \qquad (2.17)$$

where λ is the wavelength.

The singularity in the integrand is avoided by employing a numerical integration procedure in which the location of the grid is chosen to allow the singularity to be skipped.

The limits of integration will be changed later on to λ_1 and λ_2 where these two wavelengths are on the two sides of the bandedge and far away from it on both sides. This modified form will be used to evaluate changes of n from α. $\Delta\alpha$ values will be taken directly from the experimental results of transmission and photocurrent measurements and theoretical index changes will be calculated.

2.8-Forward bias phase shift

It is well known that the injection of current or carriers into a semiconductor material will change the optical absorption properties of the material and there will be a corresponding Δn change[15].

For GaAs/AlGaAs multiple quantum well waveguides, optical phase shifting with current injection has been demonstrated by Chuang et al [15]. In that work, they have used a waveguide structure with a 0.155μm active region(made of 10 layers of 10nm GaAs quantum wells with 11 layers of 5nm $Al_{.2}Ga_{.8}As$ barriers)and 400μm length. Measurements were made to obtain phase shifts for input light at different wavelengths and injected currents.

It is found that large phase shifts (upto 6π) can be achieved if the operating wavelength is closer to the bandedge. However the transmission of the device is very low at these wavelengths. With large enough detuning from the bandedge, the absorption is smaller at the cost of larger injected current for a given phase shift value. Hence, just as in the reverse bias case, there is a trade-off between large phase shift and small absorption.

For one of the materials used in this thesis research (MBE#856,refer to chapter 4) the forward bias phase shift has been measured, using a pulsed method of operation to avoid thermal effects.

CHAPTER 3

DEVICE APPLICATIONS

3.1-Chapter Introduction

In this chapter the different kinds of phase and intensity modulators will be discussed. There are two types of intensity modulators. One type relies on changes of the absorption coefficient and the other relies on the changes of the refractive index. The latter is utilized in various modulation schemes which will be explained in detail. Finally one particular application related to the phase shift measurements which is the phased-array antenna application will be discussed.

3.2-Phase modulator

The phase modulator's principle of operation is simply based on the electric field induced changes of the refractive index. Fig 3.1 shows a typical phase modulator. The waveguide geometry is usually preferred due to increased interaction length which will give rise to larger phased shifts. The two electrodes are placed on the sides of the waveguide and application of an electric field will change the

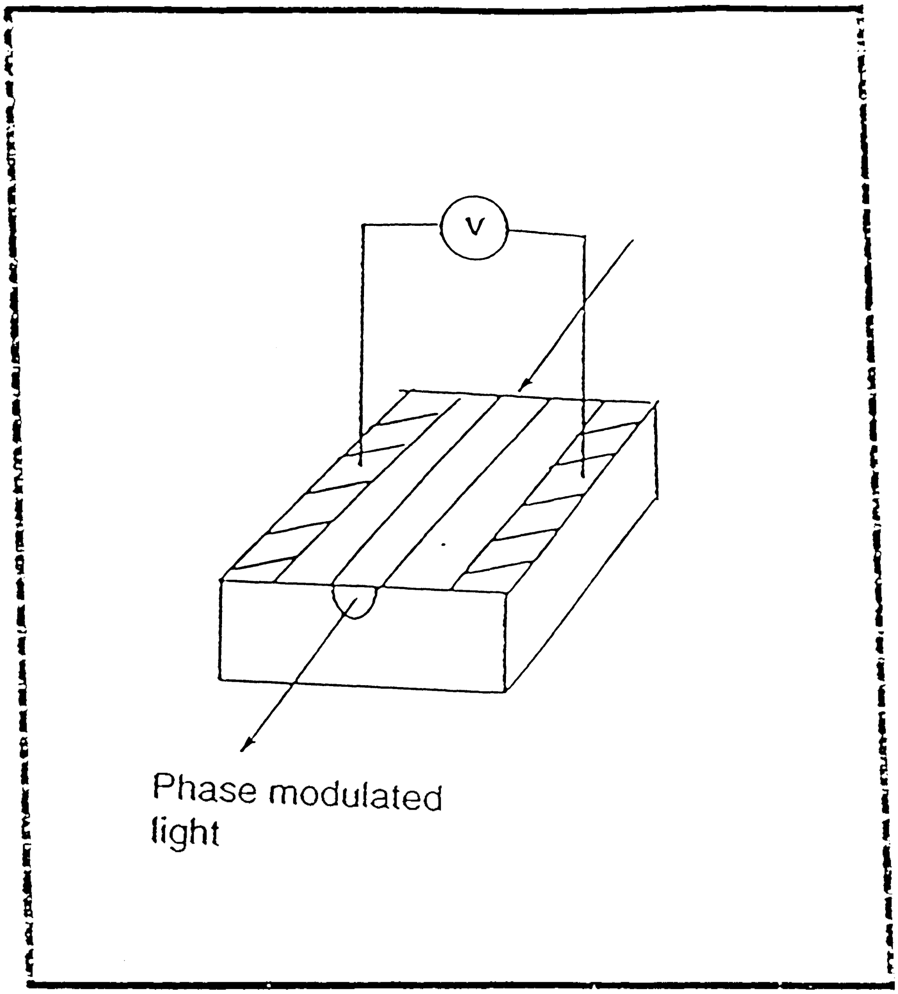

Fig 3.1- A typical waveguide phase modulator

refractive index of the guiding medium due to the electro-optic effect[7]. For a practical undoped waveguide, the electric field is uniform over the waveguiding region and the phase and the index change are related to each other by the following equation[13]

$$\Delta\Phi = \frac{2\pi}{\lambda}\Delta n L \Gamma \tag{3.1}$$

where L is the length of the strip waveguide and Γ is the confinement factor.

Utilizing this electric field induced change of index, one can modulate the phase of the propagating light beam and therefore impose the information on the carrier optical wave.

3.3-Intensity modulators based on $\Delta\alpha$

There is one type of intensity modulator called the electroabsorption modulator which employs the electric field induced changes of the absorption coefficient to intensity modulate the optical signal[4]. The Franz-Keldysh effect and Quantum Confined Stark Effect, which were described in the previous chapters are the physical mechanisms that give rise to the change in absorption coefficient and are employed by electroabsorption modulators [9],[11].

An important consideration in designing this type of modulator is the wavelength of operation. The changes of the absorption coefficient are much larger when the operating wavelength is close to the absorption edge. Hence, electrical switching from low absorption states to high absorption states is possible.

3.4-Intensity modulators based on Δn

These modulators typically use the linear electro-optic effect and are employed in different geometries that convert a change in phase to a change in intensity. Two important geometries are the Mach-Zehnder type and the dual channel coupler type of modulator [3], [4], [5].

Fig 3.2 shows a typical Mach-Zehnder type intensity modulator. In this scheme of modulation, the incident beam is split between two waveguiding branches that are the two interferometric arms and later are recombined. The two arms are made of electro-optic materials. When no voltage is applied to either of the arms, the two split signals are in phase and recombine constructively. When a field is applied to one of the arms a path difference could be introduced which causes destructive interference and the signals cancel each other. Hence intensity modulation could be performed by applying the signal to one arm of the interferometer[5].

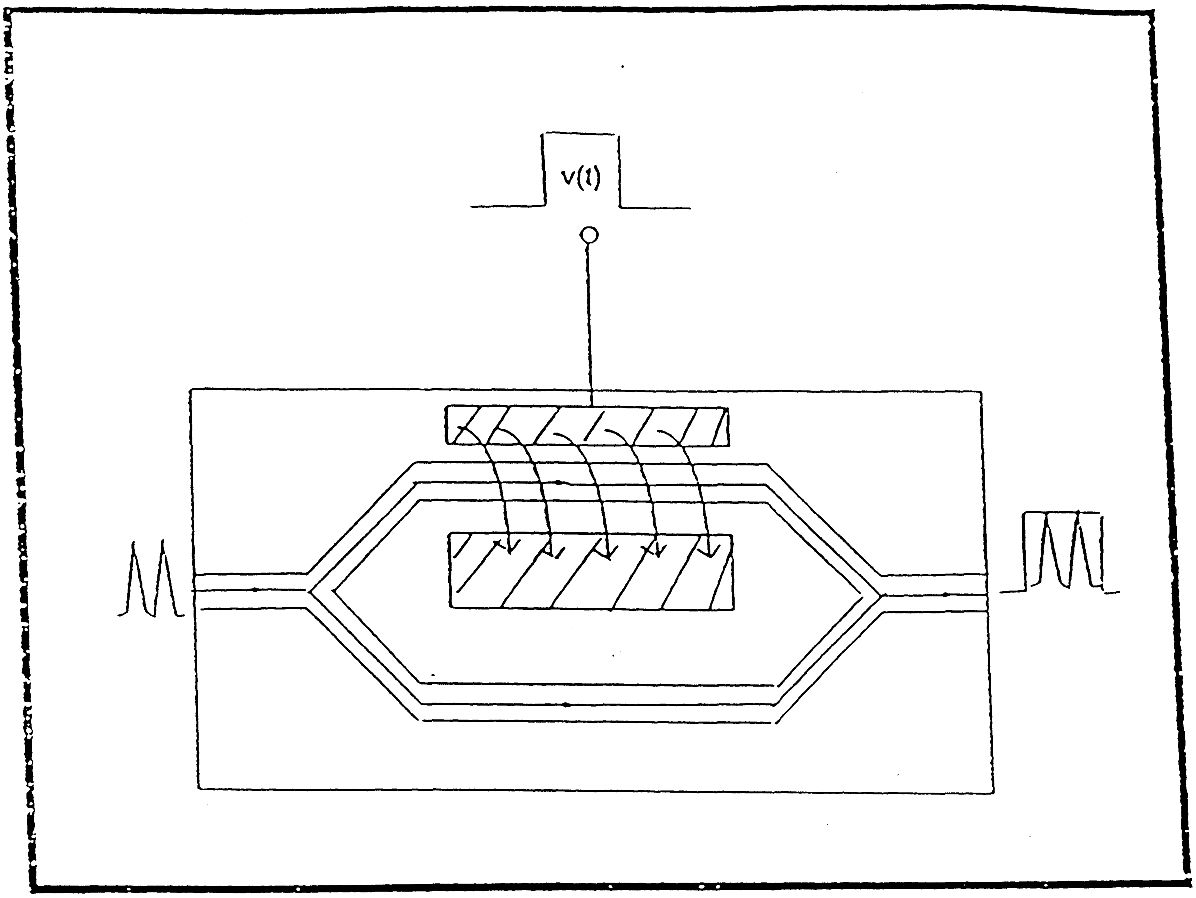

Fig 3.2-Mach-Zehnder type Intensity modulator

Another scheme of intensity modulation employs a dual channel waveguide coupler which is shown in Fig 3.3. If the two waveguides are placed close enough to each other, the optical energy can couple from one to another due to overlap of the evanescent fields. Over a certain length one can transfer all of the energy from one to the other if the two waveguides are similar. With zero volts applied, the coupling length of the dual channel coupler is chosen to be an even multiple of the exchange period, so that all of the optical energy incident on one waveguide input could exit from the same waveguide output. By applying an appropriate field to the electro-optic waveguides, one can vary the coupling length to be an odd multiple of the exchange period and hence all the optical energy incident on one input exits from the other waveguide output[5].

Applying the modulating signal to this dual channel coupler will cause an intensity modulation of the carrier signal from one of the two output channels.

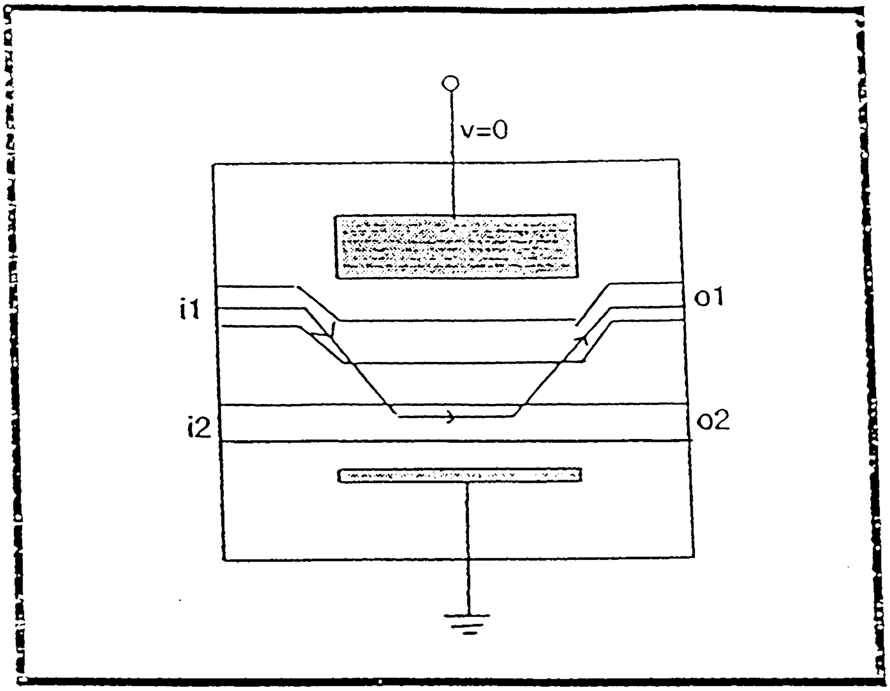

Fig 3.3.a-Directional coupler intensity modulator E=0

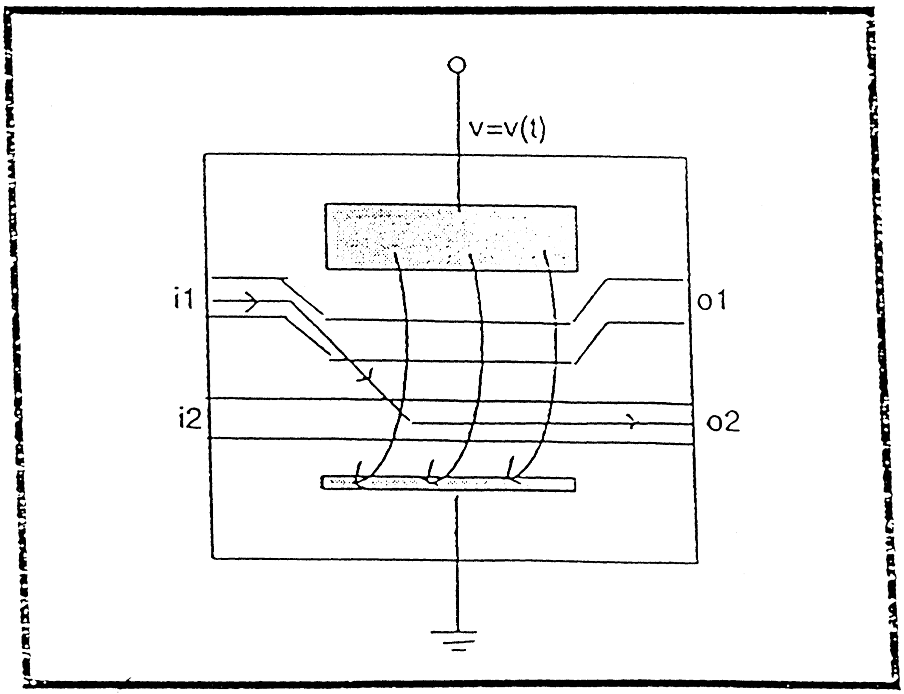

Fig 3.3.b- Directional coupler intensity modulator $E=E_0$

3.5-Phased array antenna application

In this section the phased array antenna application is discussed. This is an application which uses an optical phase modulator to control the phase of an optically generated rf or a microwave signal.

A phased array antenna consists of several radiating elements as shown in figure 3.4 and all these elements radiate at the same time [17]. If the emanating microwaves are all in phase, constructive interference will take place only along the line perpendicular to the plane of these radiating elements and along any other direction there will be destructive interference. Hence the beam is pointed towards the central axis and only the objects along this direction can be detected. The detailed shape of the output beam is controlled by the amplitude distribution in the array elements [17]. Now, if a uniform phase difference is introduced between these radiating elements, the direction at which constructive interference is taking place will be at an angle with respect to the central axis depending on the phase shift introduced. Hence it will be possible to steer the beam to different angles by introducing an appropriate relative phase shift between the array elements[17].

The phase and amplitude control would give the phased

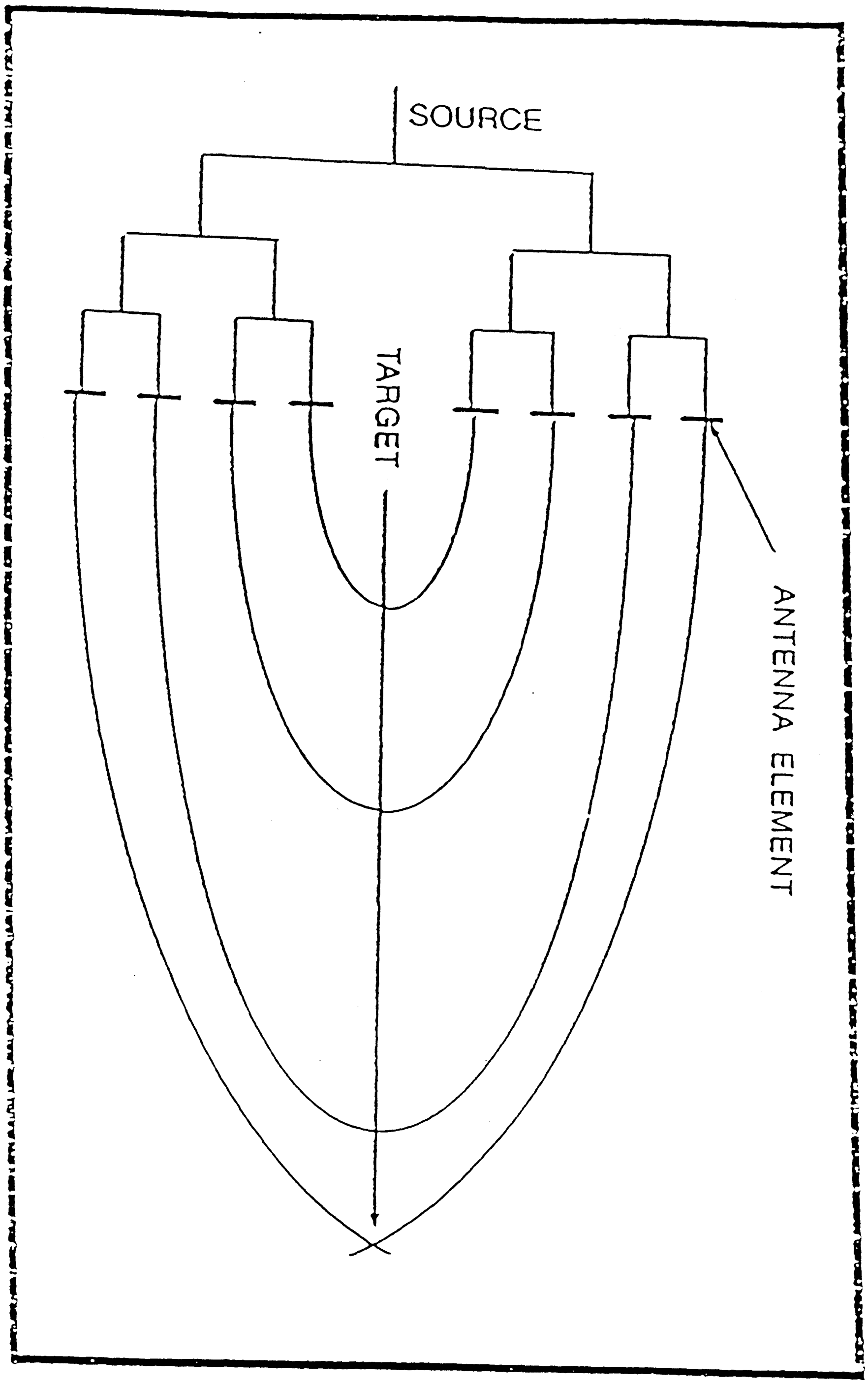

Fig 3.4 Phased array antenna elements

array radar a great advantage over the conventional radar systems since there is no need for a mechanical movement of the radar dish. The other important advantages are reduction of weight in case of airborne applications and higher scanning speeds.

Now that the principle of operation of the phased array antenna has been discussed, the optical generation and control of microwave signals will be considered [18]. This can be implemented by heterodyning two highly stable signals whose frequency difference falls in the microwave frequency range.

In our experiment, the two lasers were simulated by a Ti:Sapphire laser which was split into two beams. One of the beams is incident on an acousto-optic modulator and a frequency offset of 50 MHz was imparted to the first order diffracted beam by the acousto-optic modulator. When this frequency shifted beam is recombined with the other beam a 50MHz beat signal is generated.

Figure 3.5 shows the experimental arrangement for optical generation of an rf or a microwave signal. Heterodyning of this kind has already been implemented[18]. The two lasers have a frequency difference falling in the microwave regime. The phase shifter located in one arm changes the phase of the optical signal upon the application

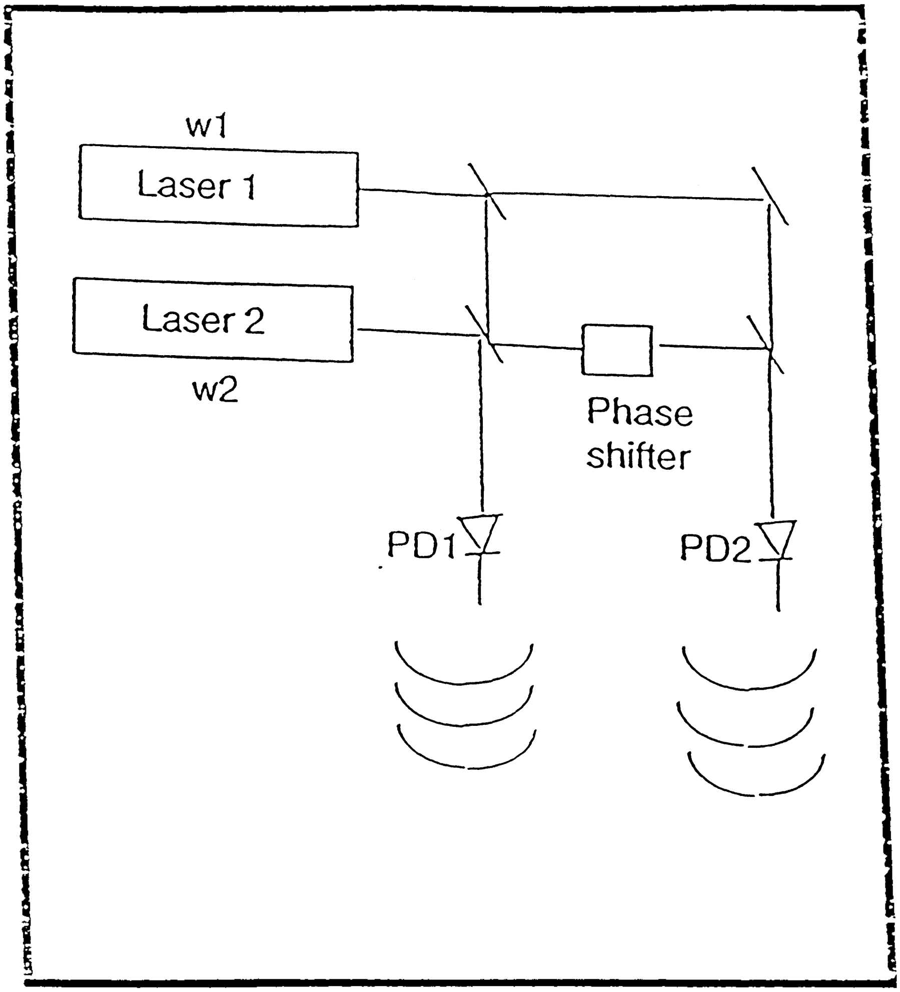

Fig 3.5–Optical generation and phase control of microwaves

of an electric field and as a result, the phase of the optically generated microwave signal will change. The two optical beams are made collinear by means of beam splitters. Each output beam is represented by a field and the sum of the two fields is described by an equation. This equation will be given in chapter 4, where the phase shift measurement setup is discussed.

In conclusion, this scheme will allow the optical generation, as well as phase and amplitude control of microwave signals.

CHAPTER 4

EXPERIMENT

4.1-Chapter Introduction

In this chapter the experimental arrangements and the materials used are discussed. In section 4.2 the structures of the two materials are shown and in section 4.3 the device fabrication and the I-V characteristics are discussed. Section 4.4 contains the calibration curves of the Ti:Sapphire laser and its power spectrum. In section 4.5, the experimental arrangement for the transverse transmission experiment is described. Section 4.6 is the description of the set-up for photocurrent and transmission measurements. In section 4.7 the Mach-Zehnder Interferometer set-up with an Acousto-Optic modulator placed in one arm, which was used for phase shift measurements, is described. Finally section 4.8 contains the description of the experimental arrangement used for the pulsed mode of operation. This mode of operation was employed simply to avoid the effect of heating. Unfortunately, for the InP based material, the phase shift measurements could not be performed due to large reverse saturation currents.

4.2-Structure of the two materials

The two materials used in the electrorefraction and electroabsorption experiments are listed in the following table

TABLE 4.1

MATERIAL	STRUCTURE
MBE#244	$InP/InAs_{.11}P_{.89}$ MQW
MBE#856	$GaAs/Al_{.2}Ga_{.8}As$ MQW

Figure 4.1 shows the material structure for MBE#244 grown at McMaster by molecular beam epitaxy. This structure is a single mode waveguide. The waveguiding region of this material is a multiple quantum well region surrounded by 2 layers of .745μm thick undoped InP on each side. The MQW region consists of 7x100Å wide $InAs_{.11}P_{.89}$ wells and 6x400Å wide InP barriers. The waveguiding region is surrounded by n and p doped InP layers on each side. These doped layers have lower index due to free carrier concentration and hence make the waveguiding possible. The topmost region is heavily doped to make better ohmic contacts. The effective index of the waveguide was found by calculating the weighted average index

MBE #244

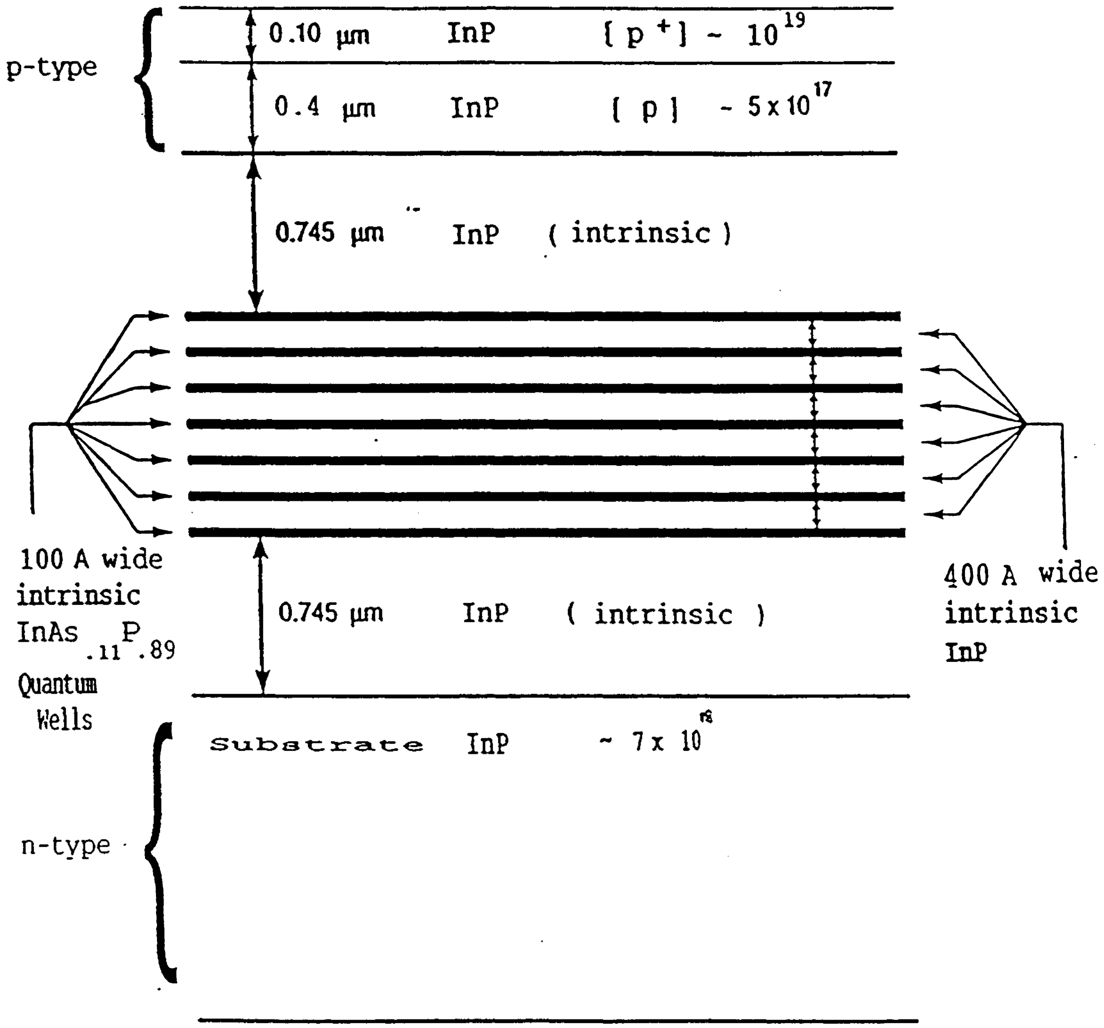

Figure 4.1-This diagram shows the material structure for MBE#244

of the MQW region and using a program called Waveguid(written by Neil Hunt). This program takes the values of thickness and index of all regions and calculates the effective index and the number of modes [12].

Figure 4.2 shows the material structure for MBE#856. This structure is also a single mode waveguide. The waveguiding region consists of 21x180Å $Ga_{.8}Al_{.2}As$ barriers and 20x80Å GaAs wells. This material was grown at BNR by molecular beam epitaxy.

4.3-Device Fabrication and I-V Characteristics

Figure 4.3 shows the I-V characteristics of the two materials.

As observed in this figure, the InP based material has a large reverse saturation current which reaches up to 1 mA at 5 volts reverse bias. The diodes used were 2mm long and 1mm wide. The contact area was the whole surface since no processing was done on this material. This large reverse current causes thermal effects which will induce an index change. Hence the phase shift measurement was more difficult to perform for this material since it was harder to distinguish between the thermal and field induced index change. Also, it is clear from the I-V curve that the sample is a poor diode since it does not show a distinct breakdown

MBE 856 Date:- January 29 1990

Single mode multiple quantum well modulator - for McMaster U.

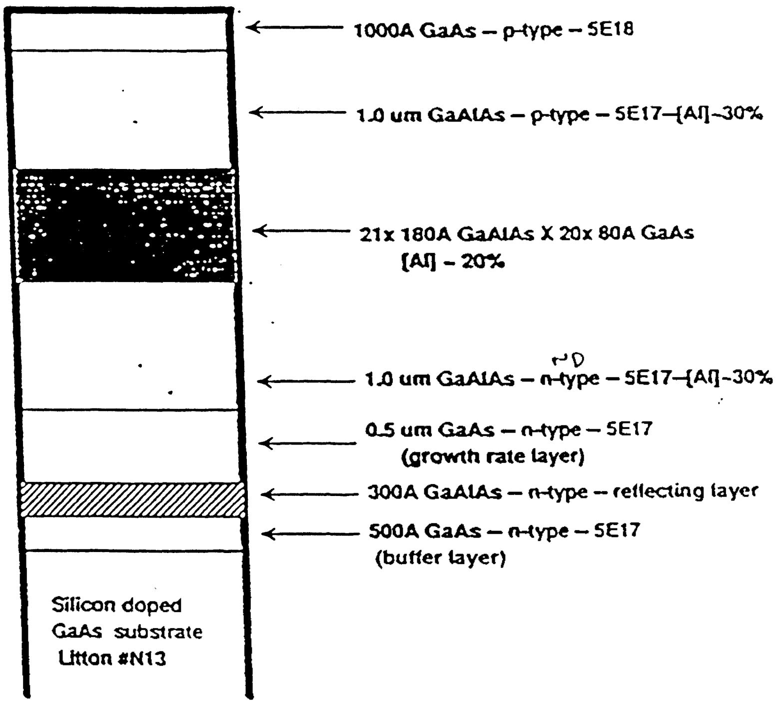

Comments :- The [Al] was measured during growth to be 28.3%, on the basis of the optical pyrometer temperature oscillations.

Figure 4.2-This diagram shows the material structure for MBE#856

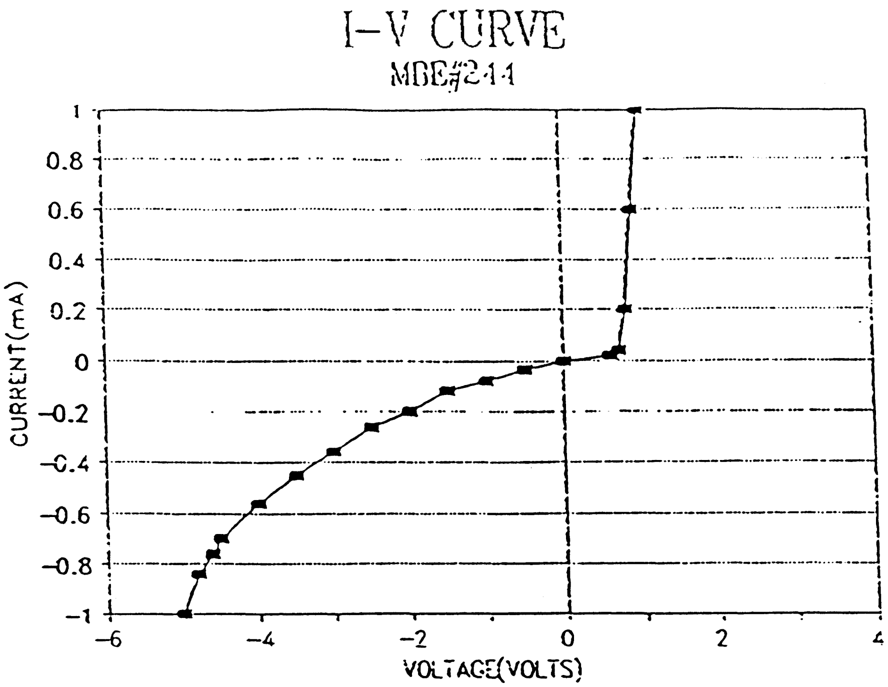

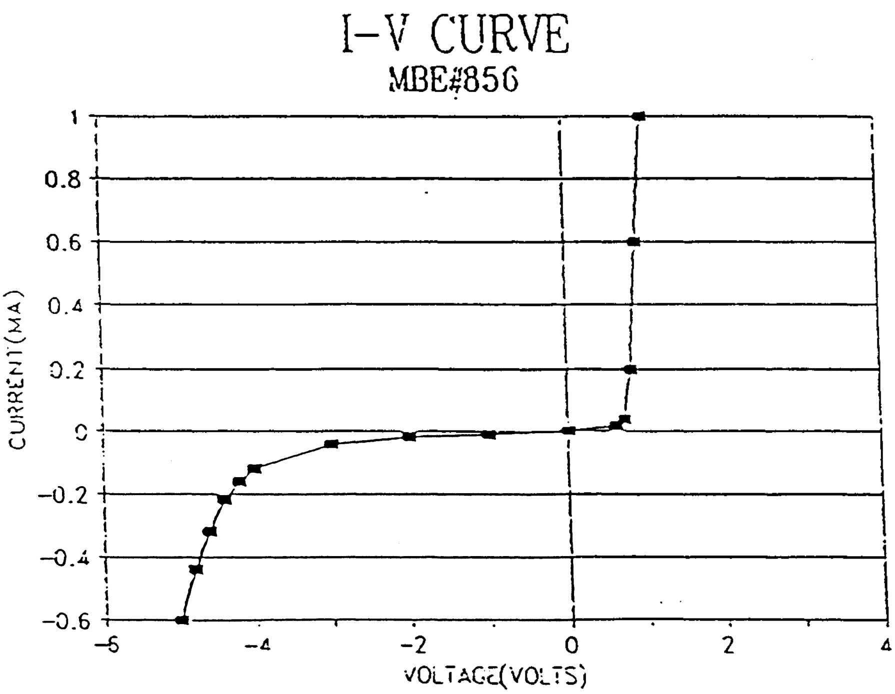

Figure 4.3-The I-V curves of MBE#856 & MBE#244

voltage.

On the other hand the GaAs/AlGaAs sample shows a good I-V characteristic. The reverse saturation current is only about 50μA upto 3 volt reverse bias and it shows a breakdown voltage at about -5 volts. These I-V characteristics are for the rib channel waveguides described in the following paragraph.

The rib waveguide channels were fabricated from MBE#856 by a mask and etch process. The central guiding rib is produced by covering the surface of the slab waveguide with a protective mask having a width equal to the desired rib and subsequently etching away material to either side. The etch used was 2.3 ml H_2SO_4, 18.4ml H_2O_2 and 184 ml H_2O.

The channels were 3μm and 10μm wide and the ribs were .8 μm in height. The lengths of the samples used were 1.5mm and all channels were electrically connected. Each sample had two 3μm wide and two 10μm wide channels. More detail on the device processing is available (contact Dr Doug Bruce).

4.4-Calibration and power spectrum of the Ti:Sapphire Laser

The Ti:Sapphire laser uses a birefringent filter as a tuning element to select a particular wavelength. A micrometer controls its rotation and therefore the wavelength of operation can be calibrated in terms of the micrometer reading.

The Ti:Sapphire Laser has three mirror sets which are the short range, intermediate range and the long range. These mirror sets would provide the laser with a wavelength tunable range of 690 to 1100 nm. For MBE#244 the long range and for MBE#856 the intermediate range mirror sets were used since they were suitable for the corresponding bandgap energies.

Figures 4.4.a and 4.4.b show the calibration curves for the long and intermediate range mirror sets respectively. A monochromator was used to find the wavelength corresponding to a particular micrometer reading.

The power spectrum of this laser for the intermediate mirror set is given in Figure 4.5. The maximum power obtained was .9 watts at 830nm. This power was generally very high for all experiments and neutral density filters(.6 D) were used to attenuate the power by a factor of 4.

4.5- Transverse transmission experiment

Figure 4.6 shows the experimental set-up for the transverse transmission experiment. The material used in this experiment was InP/InAsP (MBE#244). The source of tunable light used for this experiment was a Halogen-Tungsten lamp in conjunction with a monochromator. This source of light was used since the tunable Ti:Sapphire laser was not available at the time. The low light power was a drawback of this source of light and coupling into the Canstar coupler was difficult.

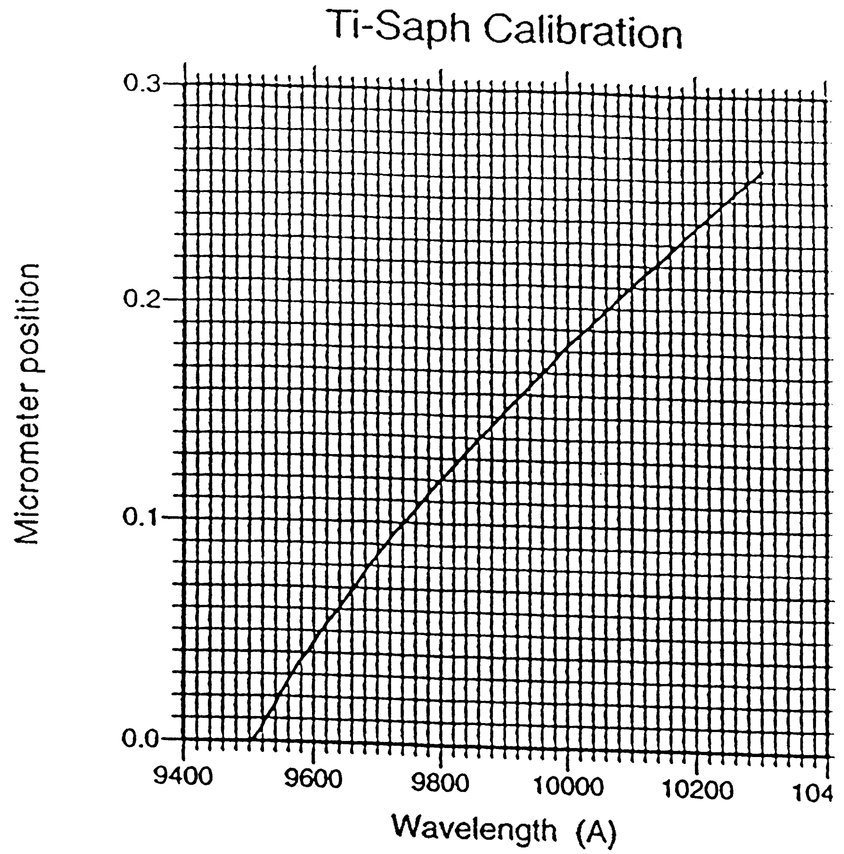

Figure 4.4.a–Calibration curve of Ti:Sapphire Laser for long range mirror sets

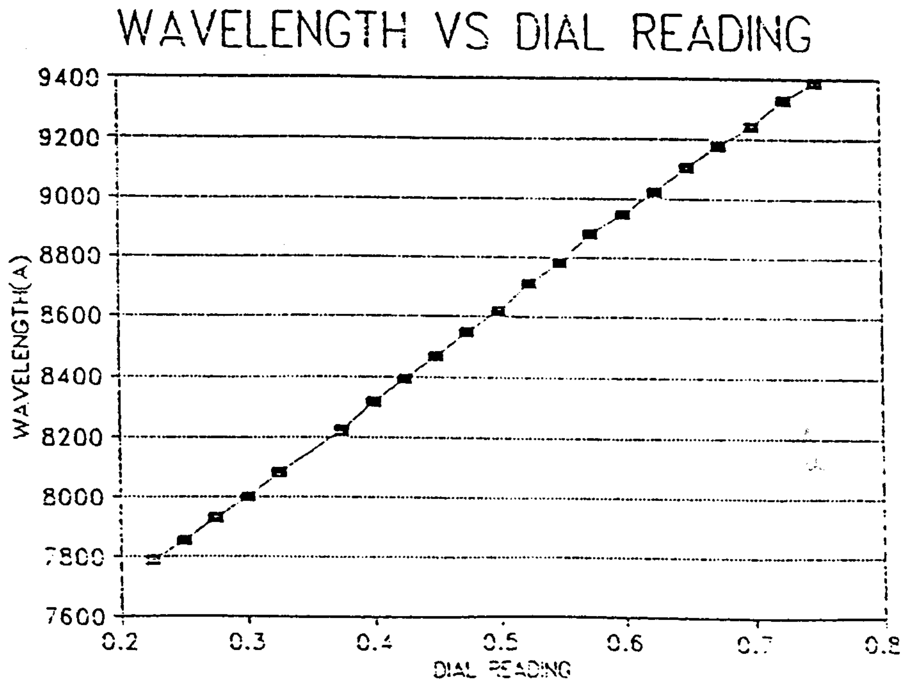

Figure 4.4.b–Calibration curve of Ti:Sapphire Laser for intermediate range mirror sets

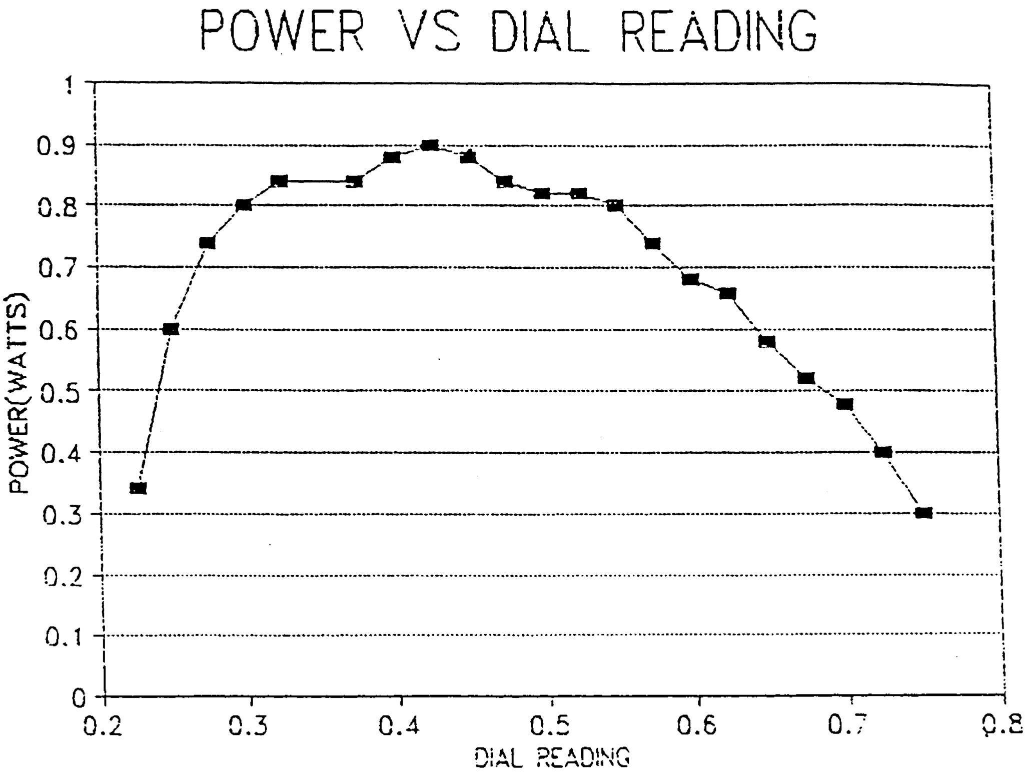

Figure 4.5-Power spectrum of Ti-Sapphire Laser

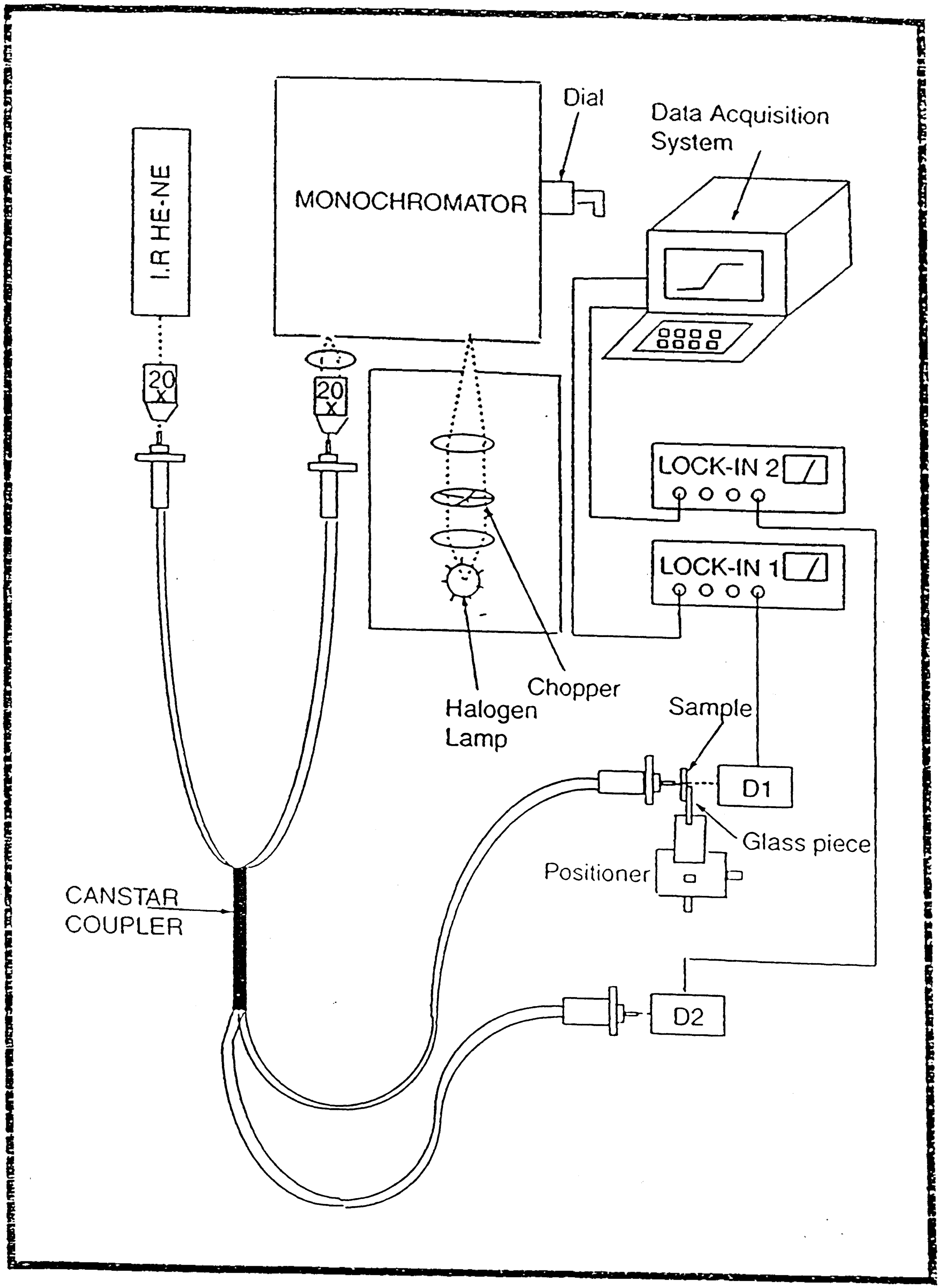

Figure 4.6- Experimental set-up for transverse transmission performed on MBE#244

The light from the white light source was collimated and focused on the entrance slit of a monochromator. The light of a selected wavelength emerging from the exit slit was collimated and focused by a 20x objective on one input of a Canstar 2x2 directional coupler.

The transverse geometry was used to shine the incident light perpendicularly to the quantum well layers. The sample was glued to a microscope slide and was held by a 3 dimensional positioner in front of one of the outputs of this coupler. For alignment purposes the I-R He-Ne was coupled into the other input of the coupler and the position for maximum transmitted intensity was found by adjusting the detector position in front of the output of the coupler. After finding this position of maximum intensity, the I.R He-Ne was turned off. The other output of the coupler was also placed in front of a second detector. This was done to monitor the incident intensity. The system had to be calibrated to correct for the spectral characteristics of the lamp, the coupler and the detectors.

The two detectors were connected to two lock-in amplifiers and the output of the lock-ins were received by the data acquisition system. The monochromator was scanned and the transmitted and the reference beams were both recorded and the former was divided by the latter to obtain the true transmission spectrum.

The sample used had a corner which had been shadowed during the MBE growth and was therefore only the substrate. After recording the spectrum for the quantum well layers this corner was placed in front of the coupler output and the transmitted spectrum was recorded to compare the "substrate only" with the quantum well spectrum.

The results of this experiment will be described in chapter Five.

4.7- Waveguide geometry photocurrent & transmission set-up

Figure 4.7 shows the experimental set-up for the transmission and photocurrent measurements. The sample is used in a waveguide geometry to increase the interaction length. In order to apply a voltage to the sample, it had to be metallized on both surfaces and wirebonded by a gold wire. The sample was mounted n-side down on a drill bit by silver paste and the drill bit is soldered into the center pin of a BNC bulkhead feed-through which is held by a plexiglass piece. The bond wire on the p-side is connected to the common side of the BNC feedthrough. The whole arrangement is mounted on a piezo-electric mount for the fine adjustment of the position.

The infrared beam from the Ti:Sapphire is directed towards the sample by a pair of mirrors. A beam splitter is placed in the path of the beam to pick off a reference which is incident on the detector D1. This is done to correct for

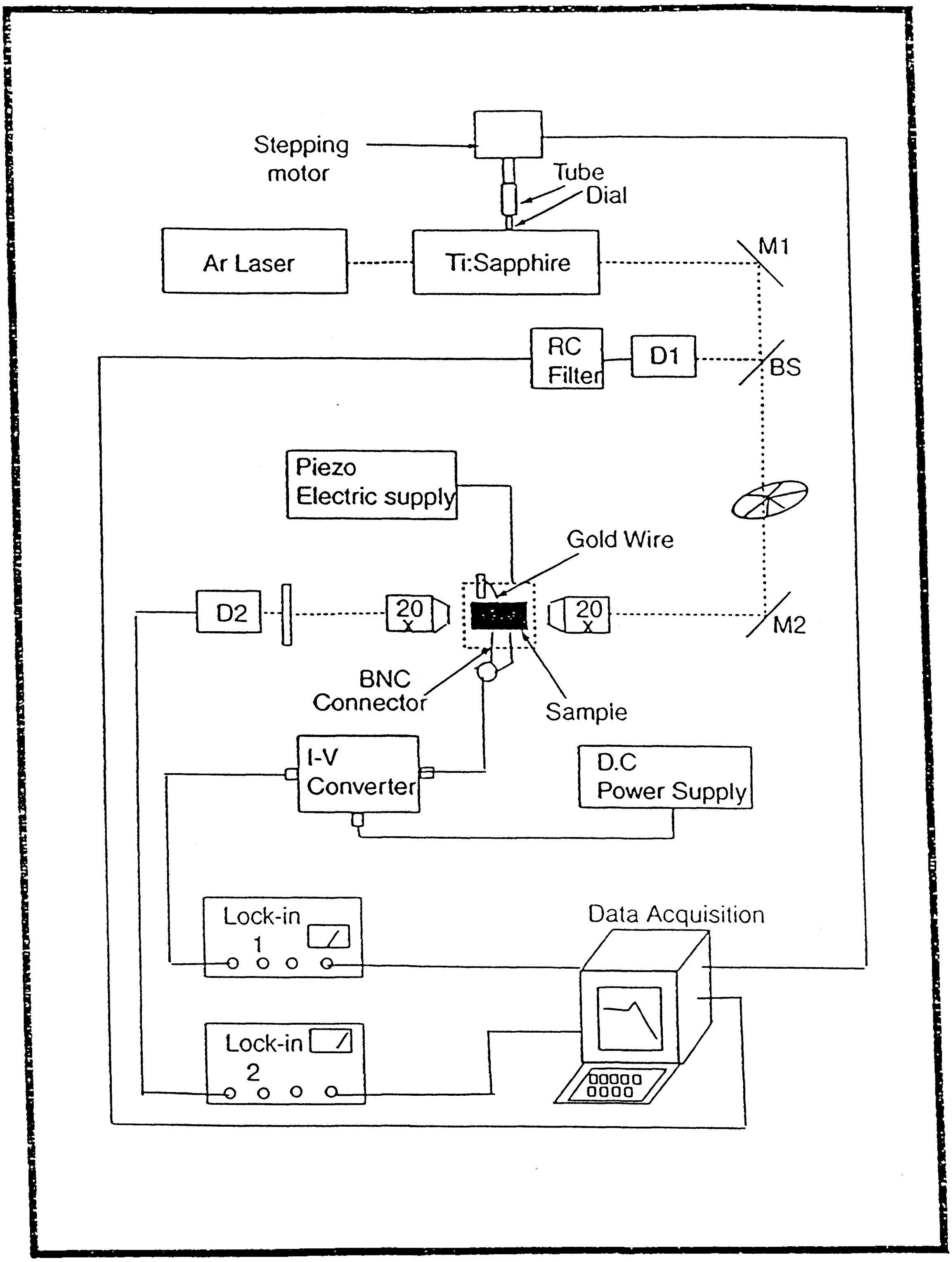

Figure 4.7–Experimental set-up for Photocurrent and Transmission measurements performed on MBE #856 and MBE#244

the wavelength dependence of the input power as depicted by the power spectrum of the Ti:Sapphire in figure 4.5.

Since the reference beam is not chopped, it contains some noise and to eliminate this noise the output of the detector D1 is sent to an RC low-pass filter. This filter will suppress all the high frequency noise and its output is sent to the data acquisition system.

The original beam transmitted through the beam splitter is chopped and is incident on a 20x microscope objective which focuses the light on the cleaved edge of the sample. The output is collected by another 20x microscope objective. Both objectives are mounted on three dimensional positioners.

The output light is passed through a slit to collect only the waveguided light and not the light transmitted through the substrate or the air above. A Silicon detector placed behind the slit detects the waveguided light, and its output is connected to a lock-in.

For photocurrent measurements the output of the BNC connector is connected to the input of a current to voltage converter[10]. A D.C power supply applies the desired voltage to the sample through the Op-Amp circuit. The current to voltage converter output sends the amplified photocurrent (Amplification 10 Volt/Amp) to a lock-in amplifier.

The wavelength of the Ti:Sapphire Laser is changed by a stepping motor controlled by the computer.

Both transmission and photocurrent signals are received from the lock-in amplifiers by the data acquisition system and are recorded at the same time. The results will be discussed in chapter 5.

4.7-Phase shift measurement set-up

The experimental set-up used for phase shift measurement is shown in figure 4.8. As explained earlier, the change of refractive index due to the application of an electric field causes a phase shift of the propagating light through the waveguide. Hence, by measuring this phase shift, one can find the index change using the equation

$$\Delta\Phi = \frac{2\pi}{\lambda}\Delta n \Gamma L \tag{4.1}$$

where L is the sample length.

In order to measure the phase shift, the sample was placed in one arm of a Mach-Zehnder interferometer. This arm also contains two 20x microscope objectives to focus the light into the waveguide and collect the waveguided light from the other end. A D.C power supply applies an electric field through a 50Ω resistor and the p-i-n diode is reverse biased.

The other arm of the interferometer has an acousto-optic modulator placed in it. Two lenses form a telescope to

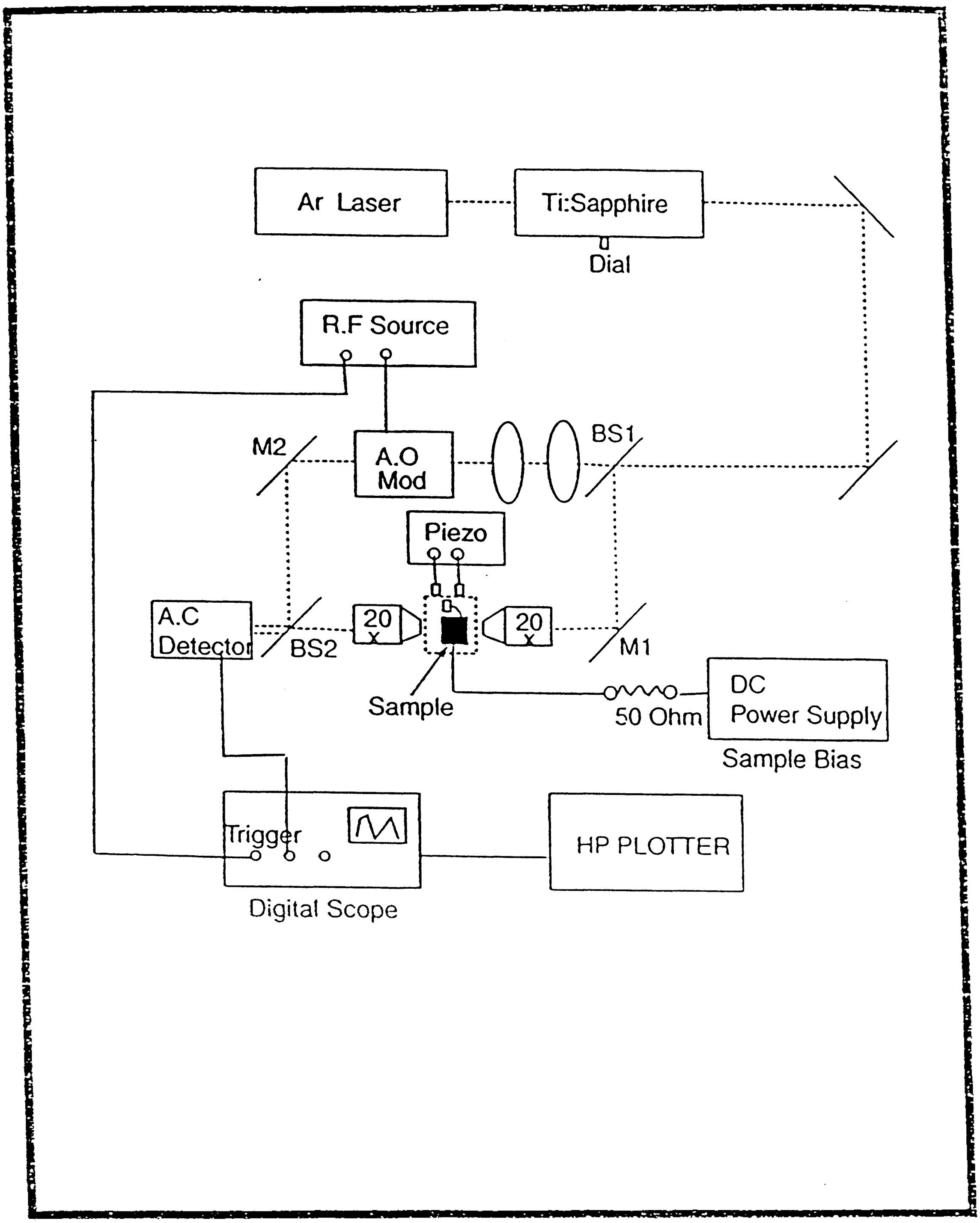

Figure 4.8- Experimental set-up for Phase Shift measurements performed on MBE#865

collimate and focus the infrared beam on the acousto-optic modulator. A R.F source applies a 50 MHz signal to the Acousto-Optic modulator and introduces a Doppler shift to the diffracted beam. When this frequency shifted beam is combined with the unshifted beam from the other arm of the interferometer, a 50 MHz beat signal is observed. Since the sample has been patterned into rib waveguide channels, the waveguided light through the channel has a circular shape and it is easier to overlap this spot with the frequency shifted beam. This is in comparison with the slab guided case where a stripe is overlapped with a spot. The two overlapping spots will form an interference pattern which oscillates at a frequency of 50 MHz.

The expression for the optical field at the detector is the superposition of two input fields and is given by[20]

$$SIGNAL \propto [E_0 Sin(\omega_{IR} t) + E_0 Sin[(\omega_{IR} + \omega_{RF})t + \Delta\phi_{IR}]]^2 \tag{4.2}$$

where $\Delta\Phi_{IR}$ is the phase difference between the RF signal and the waveguided light.

Squaring the terms in the bracket we get

$$SIGNAL \propto E_0^2 [1 + \cos(\omega_{RF} t + \Delta\phi_{RF})] \tag{4.3}$$

which shows that the optical phase shift is converted to the microwave phase shift.

The oscillating pattern is detected by a fast A.C coupled Germanium detector. This detector is a Ge AD 120 detector. It has a 500 MHz bandwidth and its rise time is less than 1ns. Its responsivity is 18 Amp/Watt measured at 1500 nm. It has been manufactured by Optoelectronics Ltd. The resulting output is detected by a digital scope which is triggered by the R.F generator. This triggering off the R.F source is done to have a reference such that when the field is applied to the sample, the phase shift could be observed as the lateral movement of a 50 MHz signal on the screen. The digital scope has several memories to store waveforms.

The procedure used to measure the phase shift was as follows. First the zero field pattern was stored in one memory. Then a field was applied to the sample and the phase shifted pattern was stored in another memory. Afterwards, both stored patterns were recalled and screen-dumped on an HP plotter. The phase shifts were directly measured from these plots as will be shown in chapter 5.

4.8- Pulsed mode of operation

Figure 4.9 shows the pulsed mode of operation for the phase shift measurement. This mode of operation was employed to distinguish between field induced phase shifts and any slow phase shift due to joule heating of samples. Heating was very

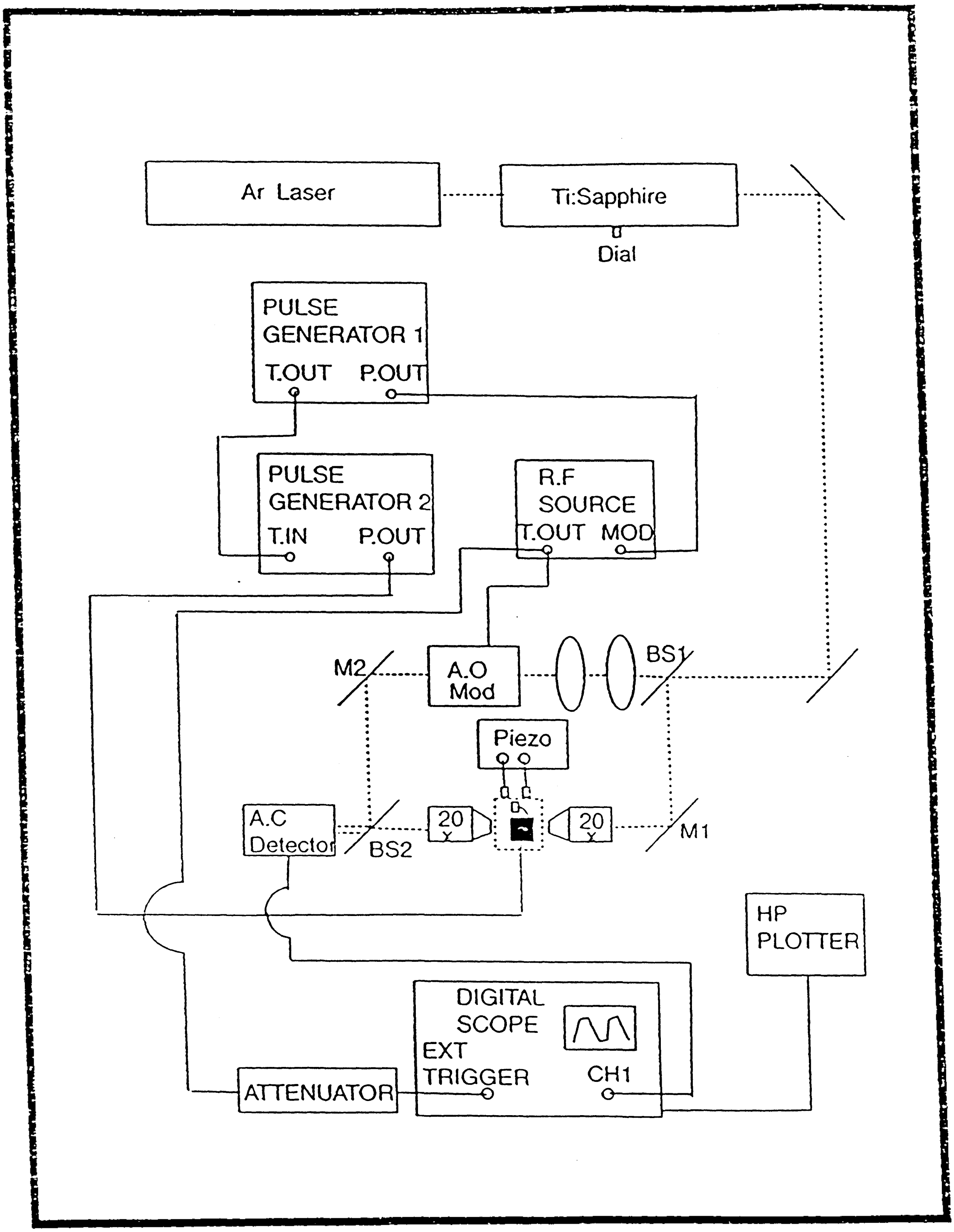

Figure 4.9- Pulsed mode of operation for phase shift measurements performed on MBE#856.

noticeable in samples with large reverse leakage currents.

As shown in the figure, two pulse generators are used. One pulse generator triggers the A.O modulator and the other pulse generator at the same time. The second pulse generator applies a low duty cycle voltage pulse to the sample. The A.O driver is turned off until it receives a trigger from the first pulse generator. The scope is triggered by the A.O driver as a reference signal.

The rest of the experimental arrangement is exactly the same as the D.C mode of operation. In this case both forward and reverse bias measurements were taken but most of the measurements were taken for the forward bias. This was done because the large currents passing through the device in the D.C forward bias cause large thermal phase shifts.

Figure 4.10 shows a typical scope trace of this mode of operation. As seen in this figure the r.f signal is superimposed on the pulse. By applying a voltage pulse to the sample the phase shift is observed in the pulsed region and in the unpulsed region no phase shift is observed. This indicates the absence of the thermal phase shifts.

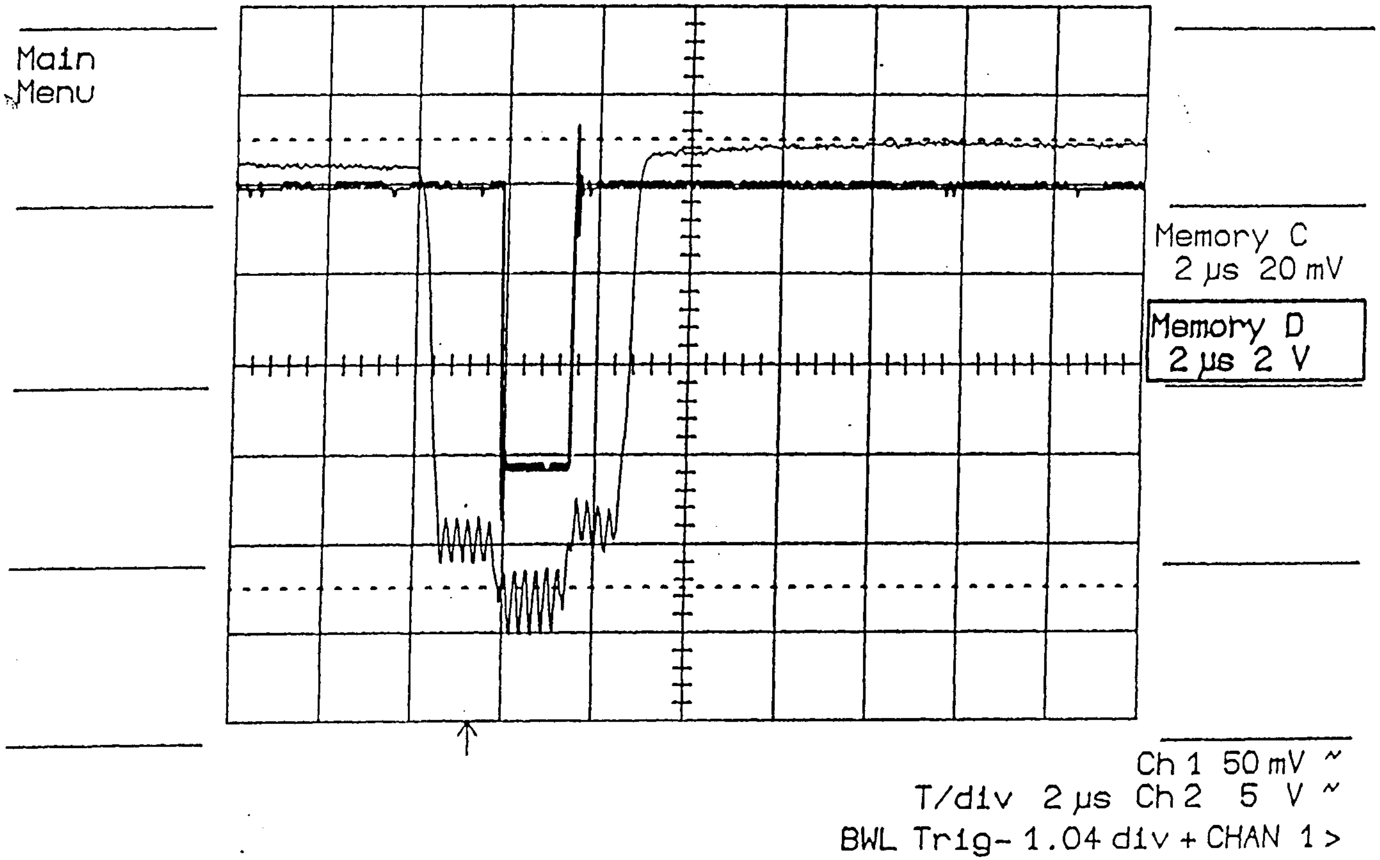

Figure 4.10-A typical scope trace for the pulse mode of operation

CHAPTER 5

RESULTS & DISCUSSION

5.1-Chapter Introduction

In this chapter the results of electroabsorption and electrorefraction experiments are presented. Section 5.2 contains the results of transverse transmission experiment and also the calculation of absorption coefficient corresponding to the quantum well transition. In section 5.3 the result of transmission measurements for MBE#244 is presented and the absorption coefficient is calculated from transmission data. Section 5.4 contains the results of transmission and photocurrent measurements for MBE#856. The absorption coefficient is calculated separately from each measurement and then a working value for α is chosen. In section 5.5 the results of reverse bias phase shifts for MBE#856 are presented. In section 5.6 a Kramers-Kronig calculation is used to predict the index changes from the experimentally measured values of the absorption coefficient for both materials. For MBE#856 the predicted phase shifts are compared to the experimental results. Section 5.7 contains the results of forward bias phase shift measurements. In section 5.8 the lasing operation of MBE#856, the L-I curve and the intensity profile of the emitted light will be described in detail. In section 5.9 the figures of merit for MBE#856 used as an electroabsorption intensity modulator are discussed. Finally section 5.10 summarizes the results of this chapter and concludes the thesis.

5.2-Transverse transmission results

Figure 5.1 shows the measured transmission for propagation perpendicular to quantum well layers for MBE#244. As the wavelength is increased by scanning the monochromator, a wavelength is selected which corresponds to the bandgap of the InP barrier and at that wavelength(λ=.92μm) the onset of transmission will appear. As the wavelength is further increased the transmitted power will rise till a wavelength is reached that corresponds to the transition between the heavy-hole ground state in the valence band and the electron ground state in the conduction band. At this particular wavelength the quantum well absorbs the incident photon and as a result a small dip is observed in the transmission curve at a wavelength of .996μm. By calculating the ratio of the transmitted power at this wavelength to the maximum transmission, i.e, T/T_0, the absorption coefficient at this wavelength can be found from the following formula

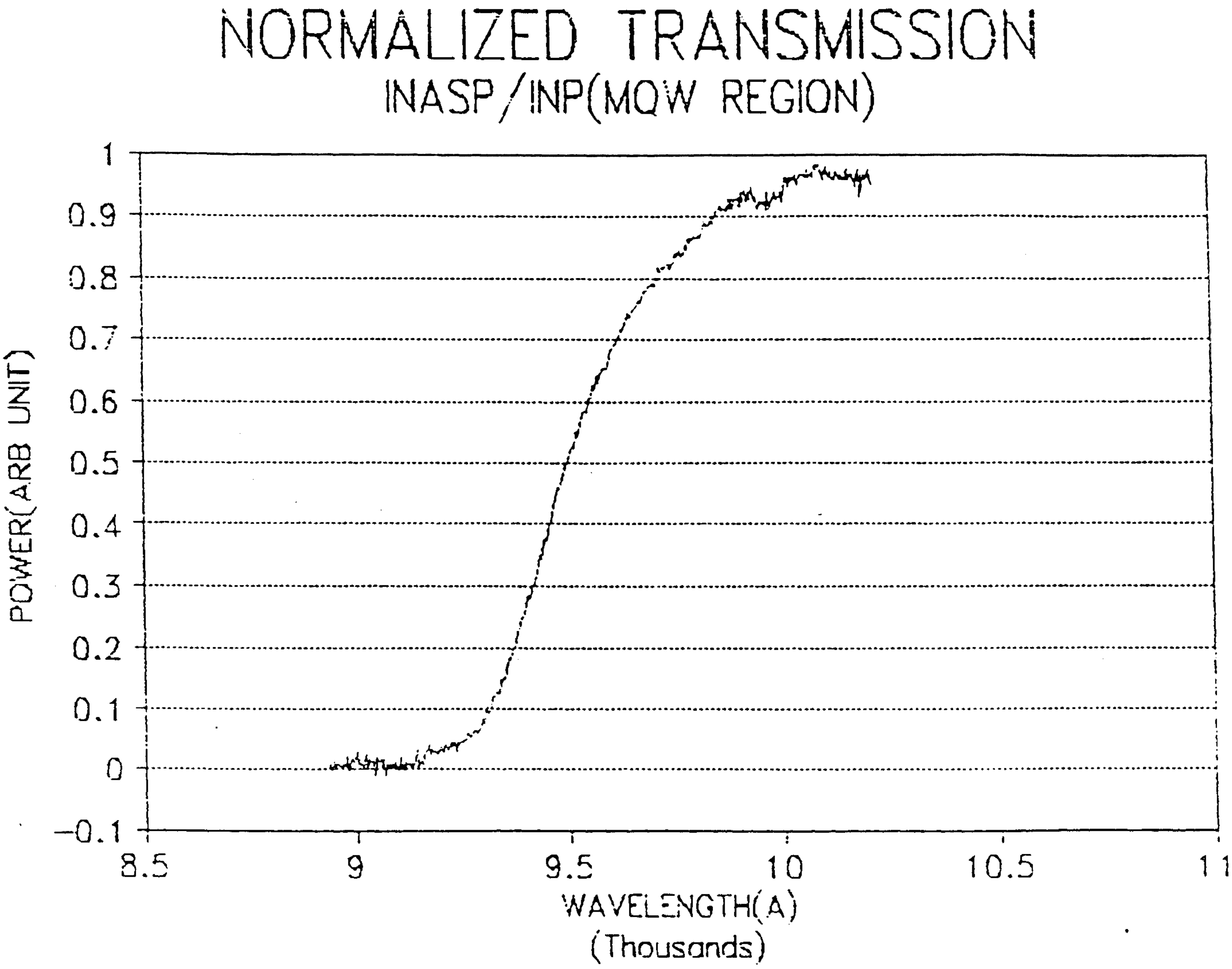

Fig 5.1-Transverse transmission spectrum through the multiple quantum well region

$$T=T_0e^{-\alpha L} \tag{5.1}$$

where L is the total width of the quantum well region. Table 5.1 contains the results of this calculation.

TABLE 5.1

Material	T/T_0	L(cm)	$\alpha(cm^{-1})$
MBE#244	97%	$3.1x10^{-5}$	982.55

In order to verify that the observed dip is due to the absorption by the quantum well region the result of the transmission through the InP substrate is also presented in Figure 5.2 and as seen in this figure, no dip is observed.

5.3- Waveguide transmission measurement results for MBE#244

Transmission measurements were performed on MBE#244 and the results are presented in this section. These measurements were made with both TE and TM polarizations to compare the effect of the two orthogonal polarizations on the transmission edge. The absorption coefficient is calculated directly from the transmission data.

For the waveguide geometry the relative transmission is related to the absorption coefficient by the relation 5.2, where Γ is the confinement factor.

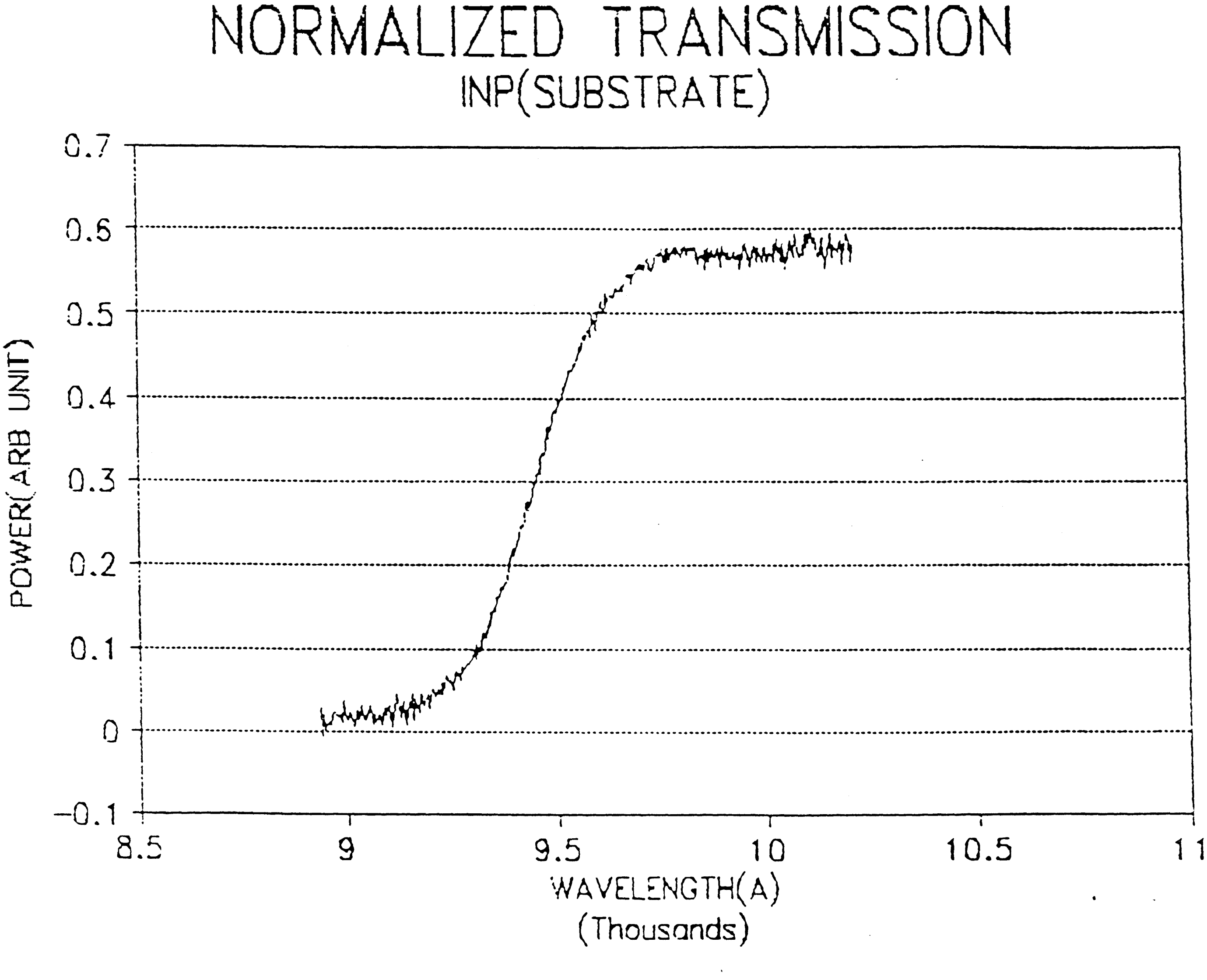

Fig 5.2-Transverse transmission spectrum through the substrate

$$T = T_0 e^{-\Gamma \alpha L} \tag{5.2}$$

Hence, before doing any calculations for the absorption coefficient, the confinement factor for this material has to be calculated. Referring to the structure of MBE#856 and using a program called Waveguid {Written by Neil Hunt}[12], this calculation has been done and the value of Γ was found to be Γ=.24. This calculated confinement factor is the fraction of power in the MQW region.

Figures 5.3 and 5.4 show the TE & TM transmission spectra for this material. As observed in these graphs the onset of the TE transmission curve is red shifted by 150Å with respect to the TM curve. The explanation for this red shift can be described in terms of heavy-hole and light-hole transitions. For TE polarization both heavy-hole and light-hole transitions are possible. The heavy-hole energy level is closer to the electron ground state in the conduction band than the light-hole energy level and hence the minimum photon energy required for the heavy-hole transition is less than that for the light-hole transition. For the TM polarization only the light-hole transition is possible and therefore the onset of the transmission curve for TM occurs at a shorter wavelength than for TE polarization.

By application of an electric field, the TE polarization red-shifts towards the region which goes beyond the tunable range of Ti:Sapphire laser. Hence the transmission data are

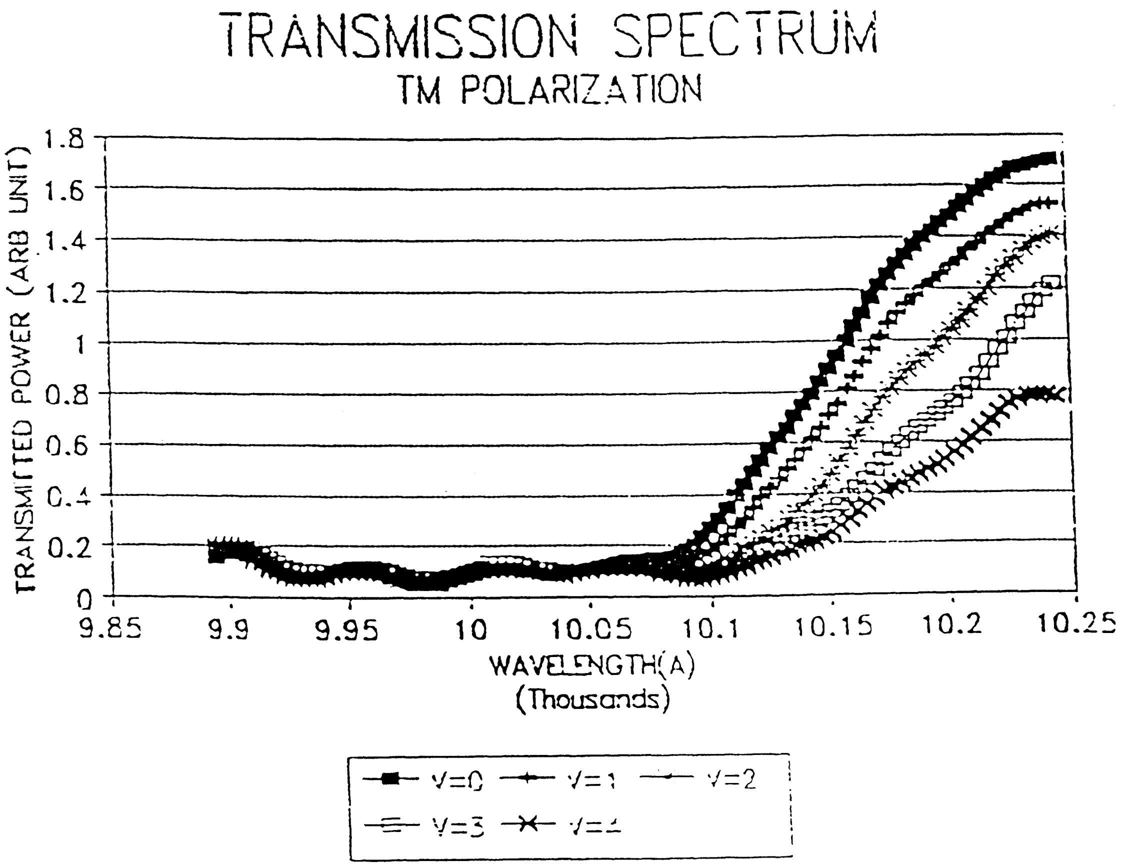

Fig 5.3-TM transmission spectrum in waveguide geometry for MBE#244

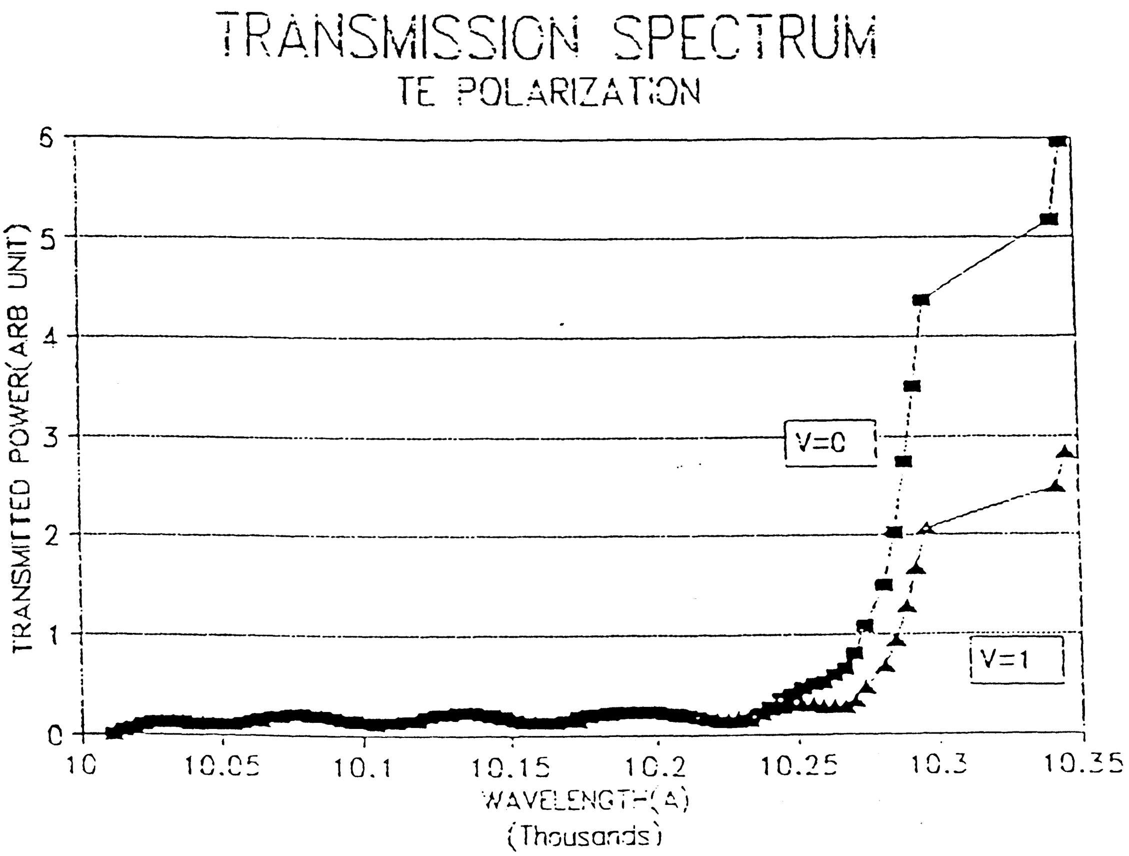

Fig 5.4-TE transmission spectrum in waveguide geometry for MBE#244

available only up to 1 volt.

Another feature which is observed in both figures 5.3 and 5.4, is a periodic variation of intensity at short wavelengths. The reason for this modulation is a zero offset light that has been subtracted from the transmission data at short wavelengths for both figures. This offset light was due to the light passing over the waveguide through the air. The modulation is similar to modulation which is often seen due to Fabry-Perot fringes induced by closely spaced surfaces in the optical system (for example the microscope objective's surface and the front face of the sample). However the observed fringe spacing(50A) would correspond to a path length in air of 0.1mm, which could not be associated with any components in our system.

Using these transmission data and the calculated confinement factor, the absorption coefficient is calculated from equation 5.2. The value of T_0 was chosen as the highest point in the transmission curve and the ratio T/T_0 was calculated.

Figures 5.5 and 5.6 show the variation of the absorption coefficient with wavelength for TM and TE polarizations, respectively. These data will be used to calculate the predicted phase shifts via the Kramers-Kronig relation in section 5.6.

MBE#244 has a structure which corresponds to a single

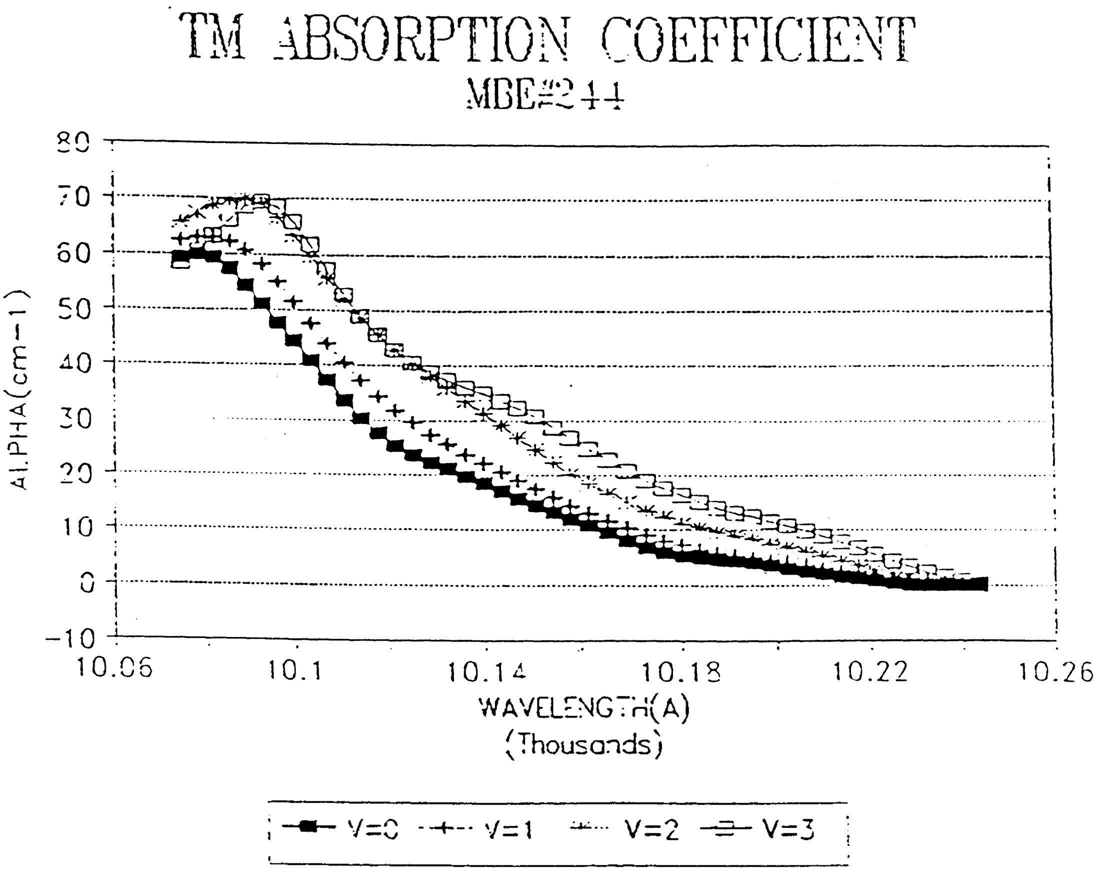

Fig 5.5-TM absorption coefficient spectrum for MBE#244

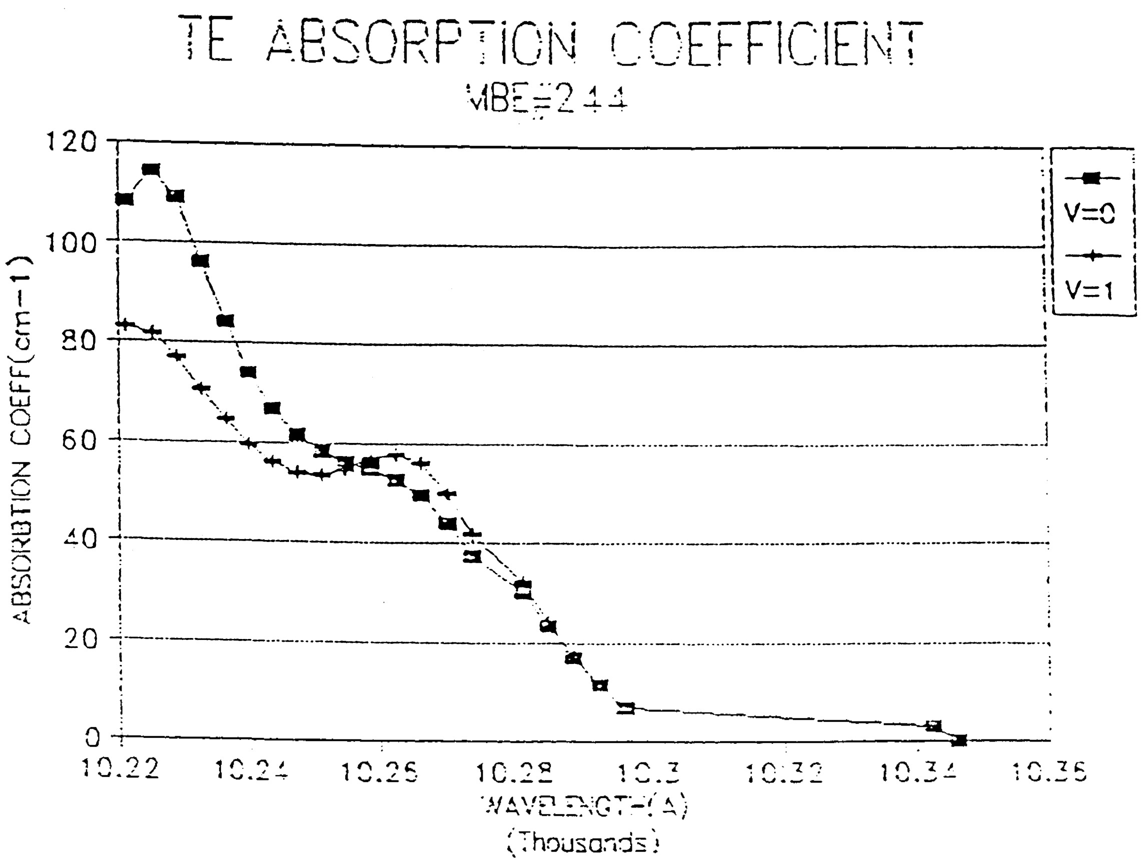

Fig 5.6-TE absorption coefficient spectrum for MBE#244

mode waveguide. Figure 5.7 shows the mode profile of this single mode waveguide.

5.4-Waveguide transmission & photocurrent measurement results for MBE#856

In this section the results of transmission and photocurrent measurements for MBE#856 are presented. The measurements were taken with both TE and TM polarized incident lights to compare the effects of the two orthogonal polarizations on the absorption edge. Since the quantum wells of this material are made of GaAs/AlGaAs, the wavelength tuning range of the Ti:Sapphire laser corresponding to InP based material (MBE#244) was not suitable for transmission/photo-current measurements. A new set of mirrors had to be installed to provide a wavelength tunability suitable for the bandgap of this material (λ_{gap}(GaAs)=.87μm). This was done by replacing one mirror at a time and optimizing the output power of the laser till all six mirrors are replaced.

The photocurrent/transmission data were taken at the same time to have similar conditions and to be able to compare the results from these two separate measurements.

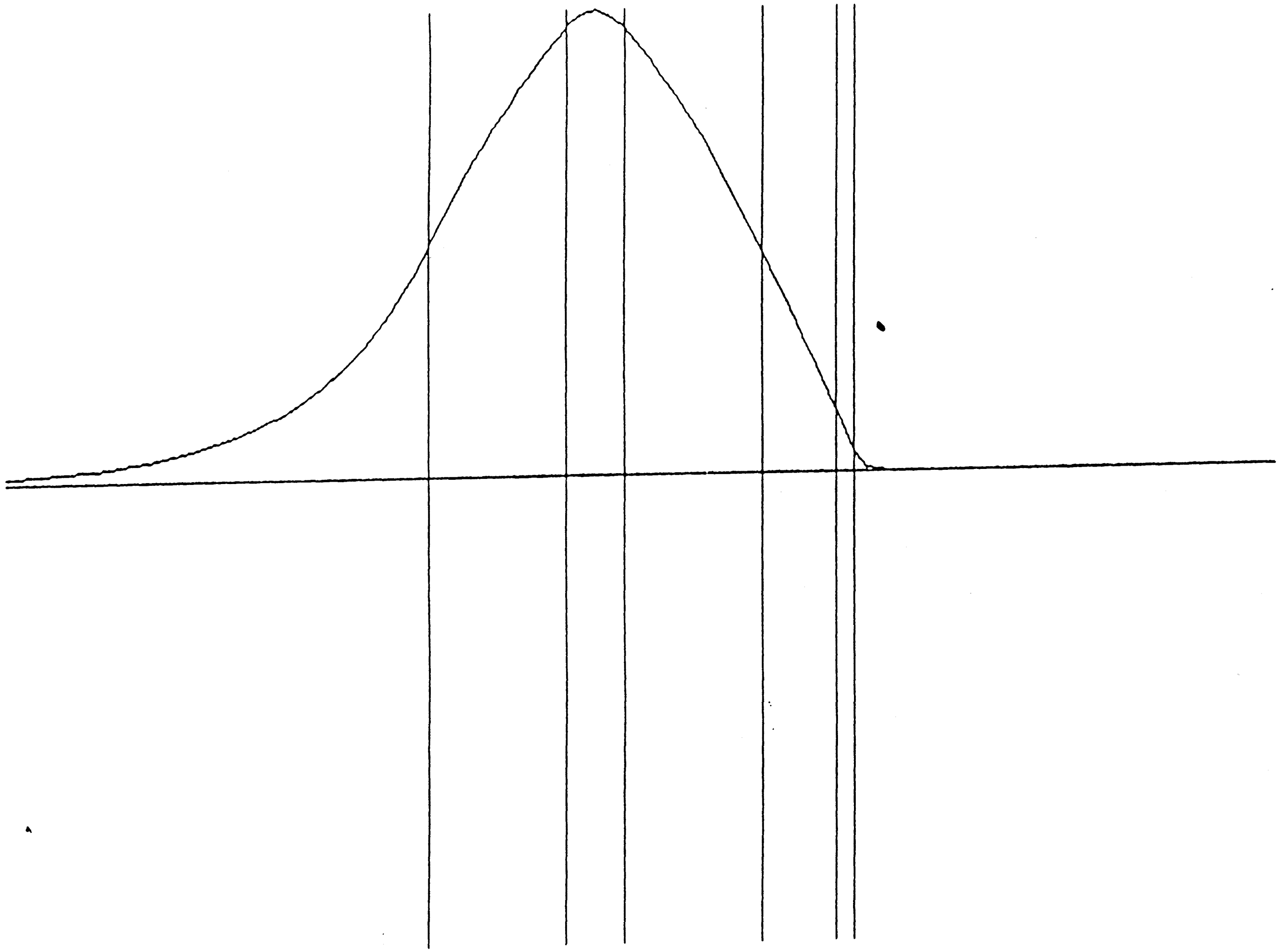

Fig 5.7-Mode profile of MBE#244 single mode waveguide
for $\lambda = 0.98 \mu m$

5.4.1- TE Transmission/Photocurrent

Figure 5.8 shows the TE transmission and photocurrent measurement data taken at various voltages. The transmission and photocurrent data are consistent and show the same location of bandedge and shift with the applied voltage. As observed from these data the absorption onset appears at about 860nm and the transition between no absorption and nearly 100% absorption takes place over a wavelength range of about 30nm. The photocurrent is seen to increase at short wavelengths for higher voltage values. At a wavelength of 855nm the photocurrent shows almost a 50% rise from 0 to 5 volts. The reason for this rise is not clear since the depletion region widths in the n and p regions are much smaller than the width of the intrinsic region[1], and therefore will not have a substantial effect on production of more photocurrent.

The shift of the bandedge seems to have a nonlinear dependence on voltage. Table 5.2 (next page) summarizes the result of this shift with the applied voltage.

TABLE 5.2

APPLIED VOLTAGE VOLTS	BANDEDGE SHIFT Å
1	12
2	31
3	59
4	94
5	141

These bandedge shifts are quite comparable to the shifts observed in similar GaAs/AlGaAs and GaAs/InGaAs structures [9],[10].

Once again, to calculate the absorption coefficient, the confinement factor has to be calculated. Referring to figure 4.2 which shows the structure of this material, it is seen that the Al concentration of the reflecting layer is not specified. Hence, we use a simplified 6 layer structure to calculate the confinement factor. The GaAs substrate of this simplified structure is located below the 1μm AlGaAs layer. Using the waveguid program, the effective index and the confinement factor were calculated to be NE=3.559 and Γ=.748 where Γ is the fraction of power in the MQW region.

After finding the value of the confinement factor, the

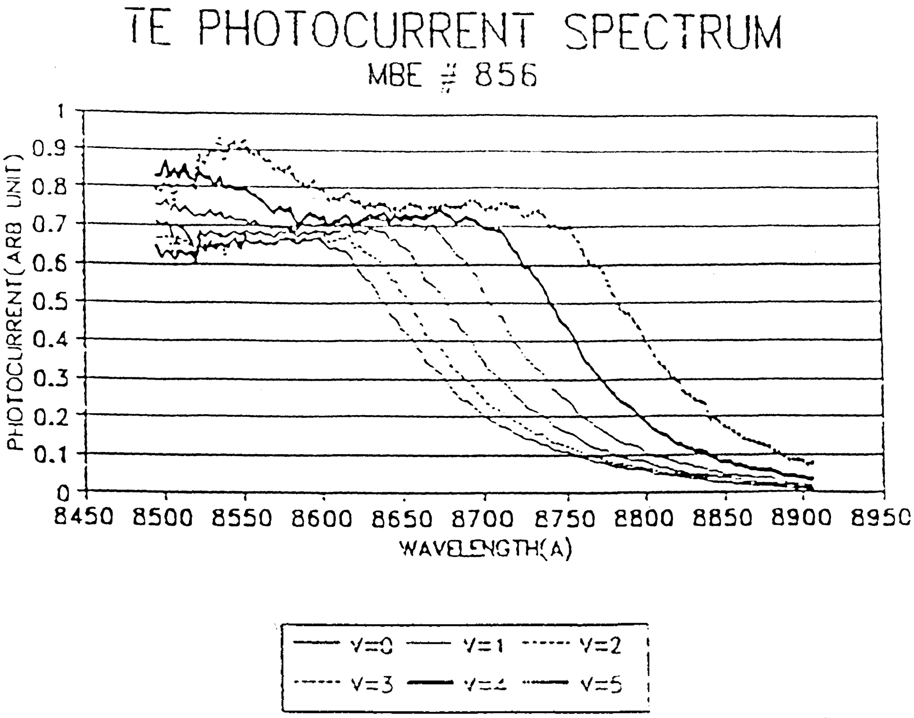

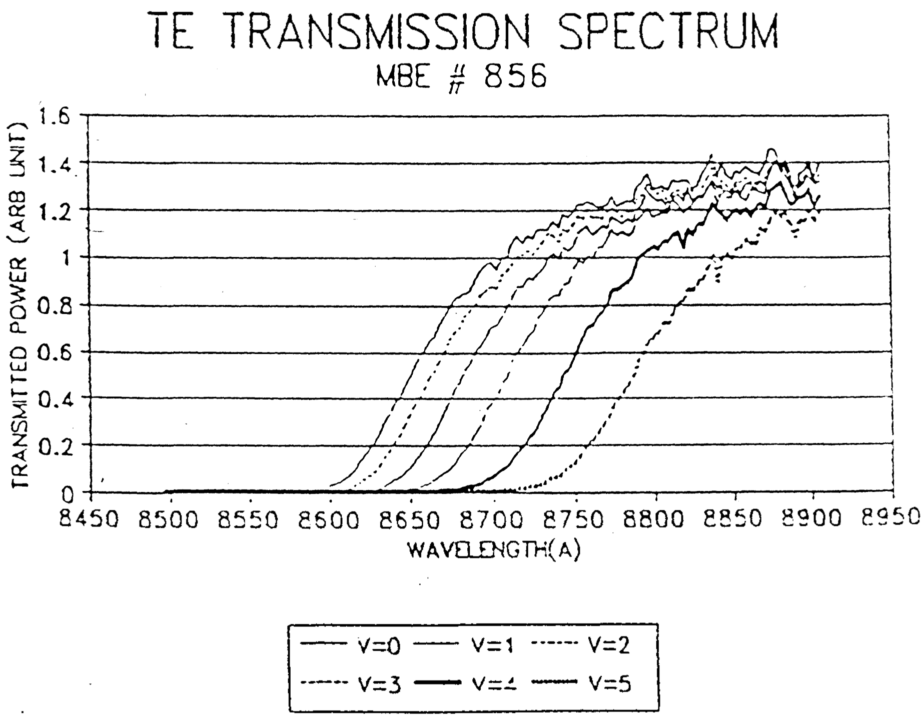

Figure 5.8-Transmission and photocurrent spectra for MBE#856

absorption coefficient was calculated separately from the transmission and photocurrent data. Equation 5-2 is used for $\alpha_{transmission}$ and for $\alpha_{photocurrent}$ the following equation will be used

$$I = I_0(1 - e^{-\Gamma\alpha L}) \tag{5.3}$$

where I_0 is the maximum photocurrent. The results are plotted in figures 5.9 and 5.10 for $\alpha_{transmission}$ and $\alpha_{photocurrent}$, respectively.

Referring to figure 5.10, it is observed that the absorption coefficient values drop for short wavelengths and higher bias voltages like 4 and 5 volts. In order to explain this decrease in the absorption coefficient, equation 5.3 is rearranged to get the value of α given by

$$\alpha = \frac{1}{\Gamma L} \ln \frac{1}{1 - I/I_0} \tag{5.4}$$

where the value of I_0 is always set to be equal to the maximum photocurrent.

Referring to figure 5.8, it is observed that, for low bias voltages (V=0,2), the photocurrent is almost constant in the short wavelength region up to the absorption edge where it drops. The value of I_0 is set to be equal to this constant value and hence the absorption coefficient calculated from 5.4 is constant in this range(Refer to figure 5.10).

For higher bias voltages (V=4,5), figure 5.8 shows that

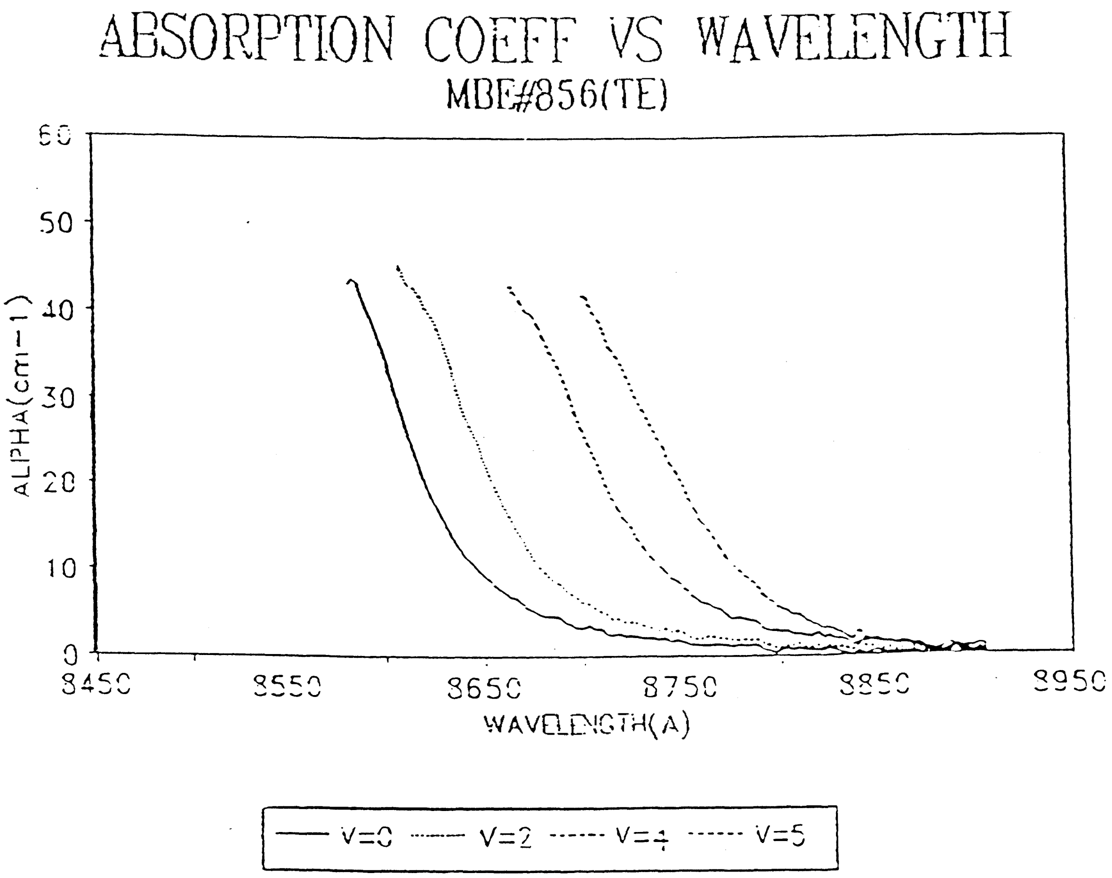

Figure 5.9- Absorption coefficient calculated from transmission data for L=1.5mm and Γ=.748. The values of absorption coefficient for short wavelength region of each curve have not been shown due to their large values.

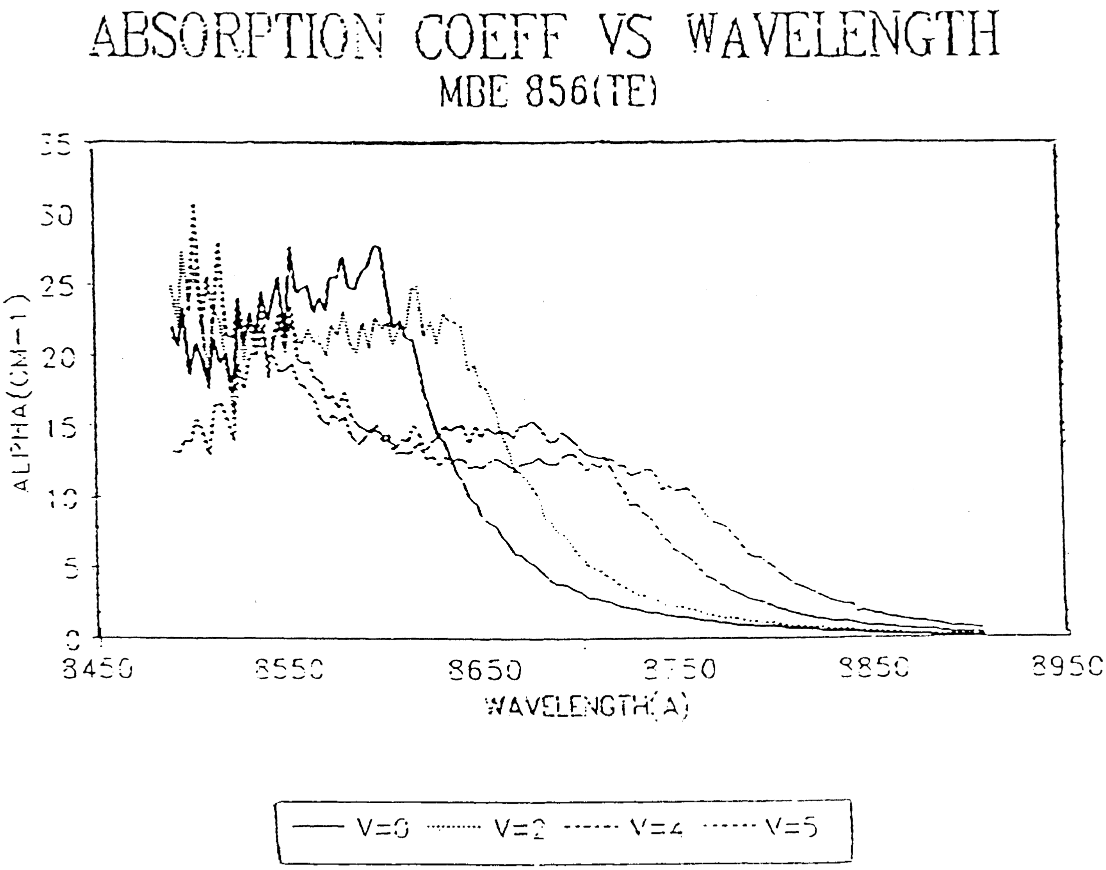

Figure 5.10- Absorption coefficient calculated from photocurrent data for various bias voltages.

the photocurrent drops from a higher to a lower value at short wavelength region before the absorption edge. Since the value of I_0 is set to be equal to the maximum value of photocurrent, the ratio I/I_0 is reduced(for low bias voltages this ratio is nearly 1 at short wavelengths) and hence from 5.4 there will be a drop in the value of α for higher voltages comparing to lower voltages at short wavelengths.

Figures 5.11 and 5.12 show plots of absorption coefficient for various voltages, calculated from transmission and photocurrent data. For V=0,2 (Figure 5.11), there is a good agreement between the two values. For V=4,5 (Figure 5.12), the absorption coefficient was calculated again by setting I_0 equal to the flat part of the photocurrent curve and then compared to transmission values. It is observed that the absorption coefficient values calculated from transmission measurements are higher at shorter wavelengths than those calculated from photocurrent measurements. In both cases the reliability of the α values decreases as α becomes large. However, the values derived from the photocurrent measurements are the least reliable at shorter wavelengths because there was a substantial dark current contribution that made photocurrent values uncertain.

For the Kramers-Kronig calculations (section 5.6), the results had a very small dependence on which measurements were used to determine α. For calculating the on/off ratios

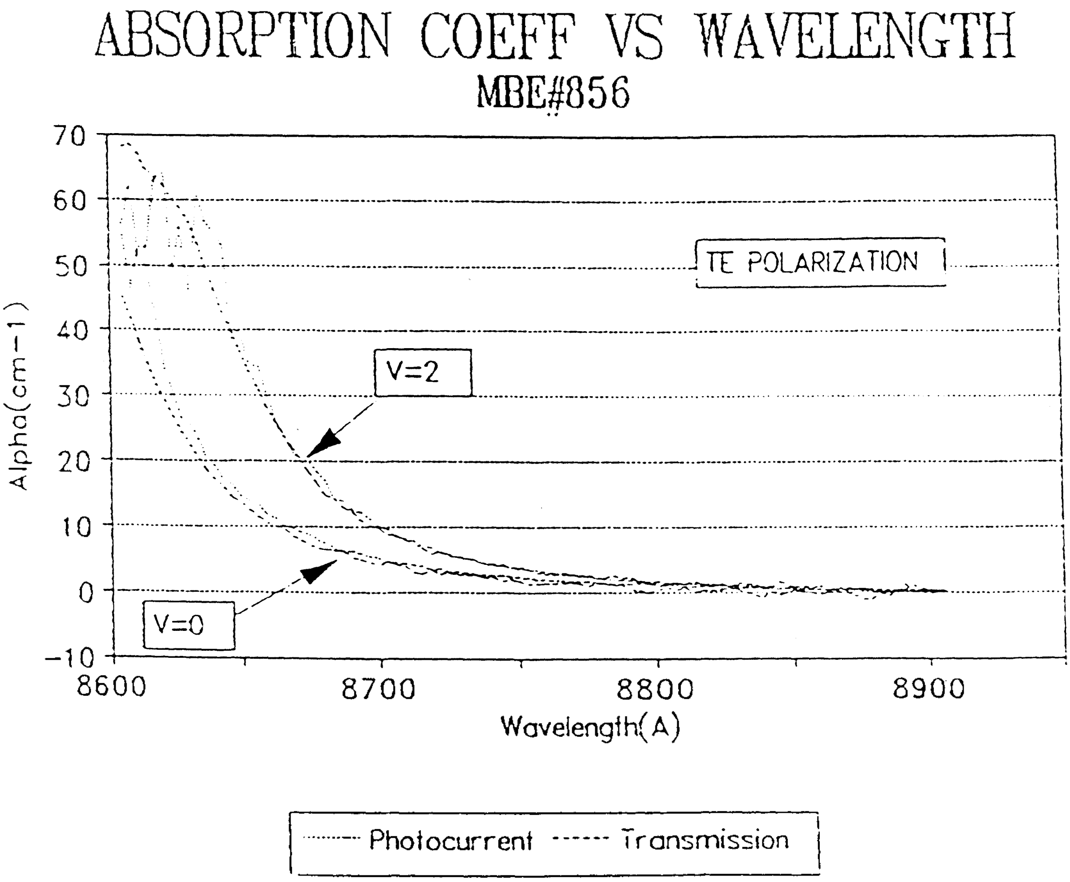

Figure 5.11 - The absorption coefficient values calculated from transmission & photocurrent data are consistent as shown in the figure.

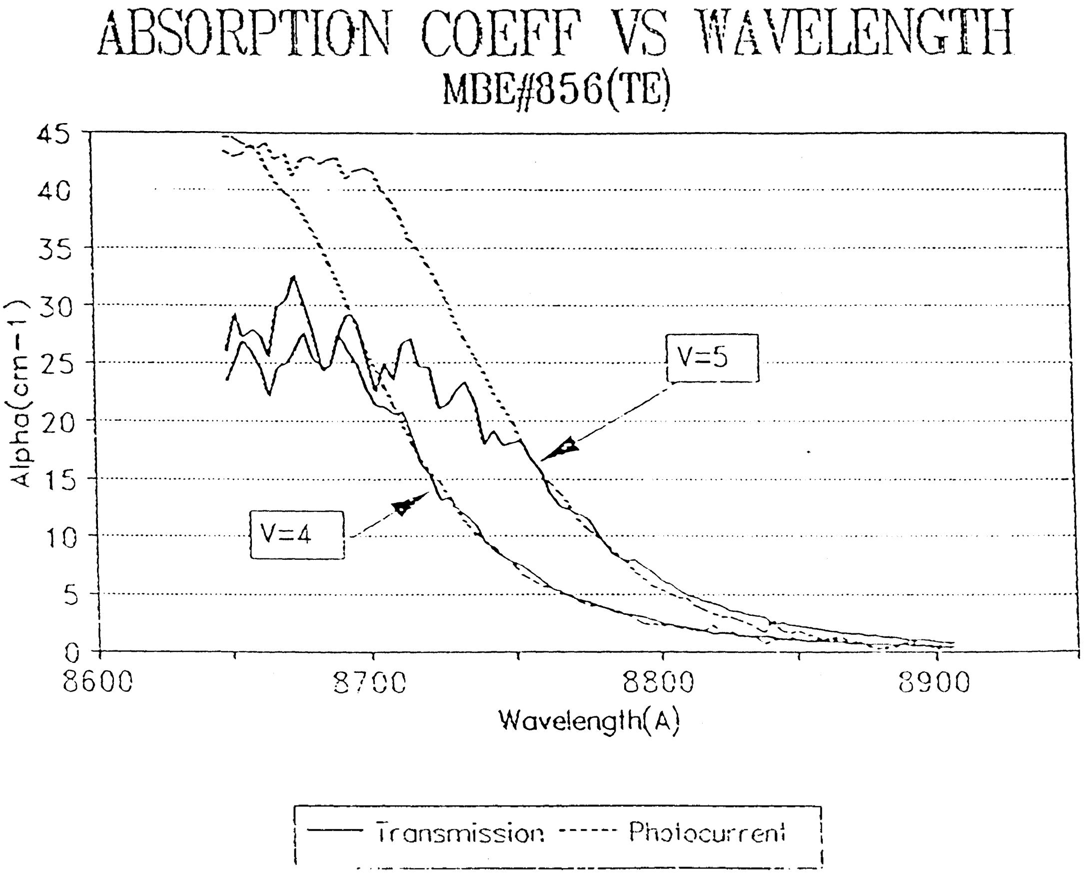

Figure 5.12- Absorption coefficient values calculated from transmission and photocurrent data for 4 and 5 volts.

(section 5.9), $\Delta\alpha$ values from transmission measurements are chosen.

To end this section, it is mentioned that MBE#856 is a single mode waveguide and its mode profile is shown in figure 5.13.

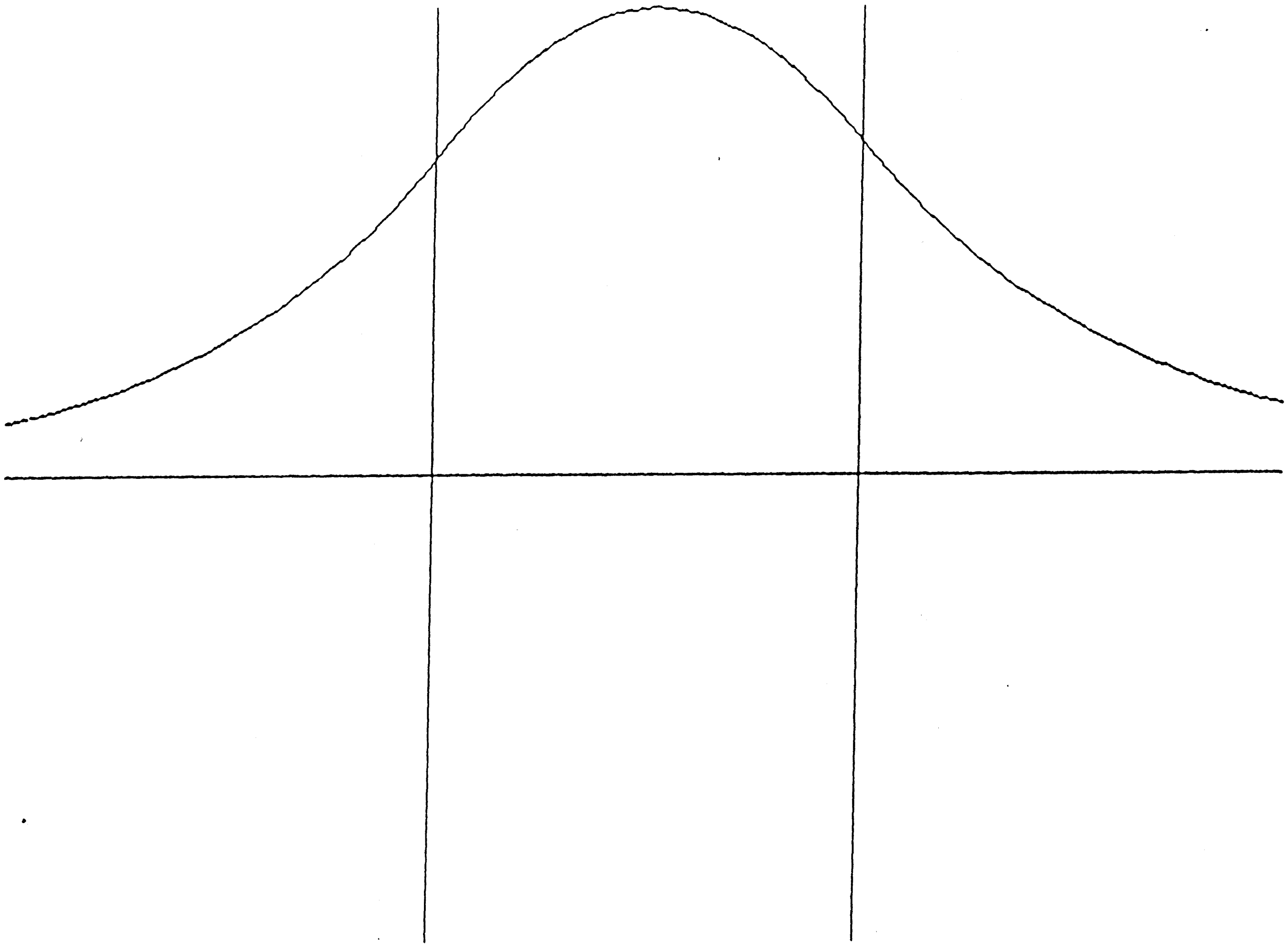

Figure 5.13- Mode profile of MBE#856. The material was approximated as a 3 layer waveguide since the cladding layers are thick enough. $\lambda = 0.87 \mu m$

5.4.2- TM Transmission/Photocurrent

Figure 5-14 is the plot of the transmission and photocurrent spectra for TM polarized light. As mentioned earlier in chapter 2 for TM polarization, only the light-hole transition to conduction band is allowed. Hence the onset of the transmission and photocurrent spectra is expected to be blue shifted as compared to TE polarized light simply because the light-hole energy level is further away from the electron ground state in the conduction band than the heavy-hole energy level and therefore needs a higher energy photon to make the transition. This is what is exactly observed by comparing the transmission onsets in figures 5.8 and 5.14.

The onset of the transmission curve appears at 8550Å for TM polarized light as opposed to 8600Å for TE polarized light which means a 50Å blue shift.

Just like the TE case the TM shift of the bandedge also shows a non-linear dependence on applied voltage. For the physical explanation of this non-linearity one has to refer to theoretical values of absorption coefficient calculated from Airy and Bairy functions [10].

The shift of the bandedge with the applied voltage is tabulated in table 5.3.

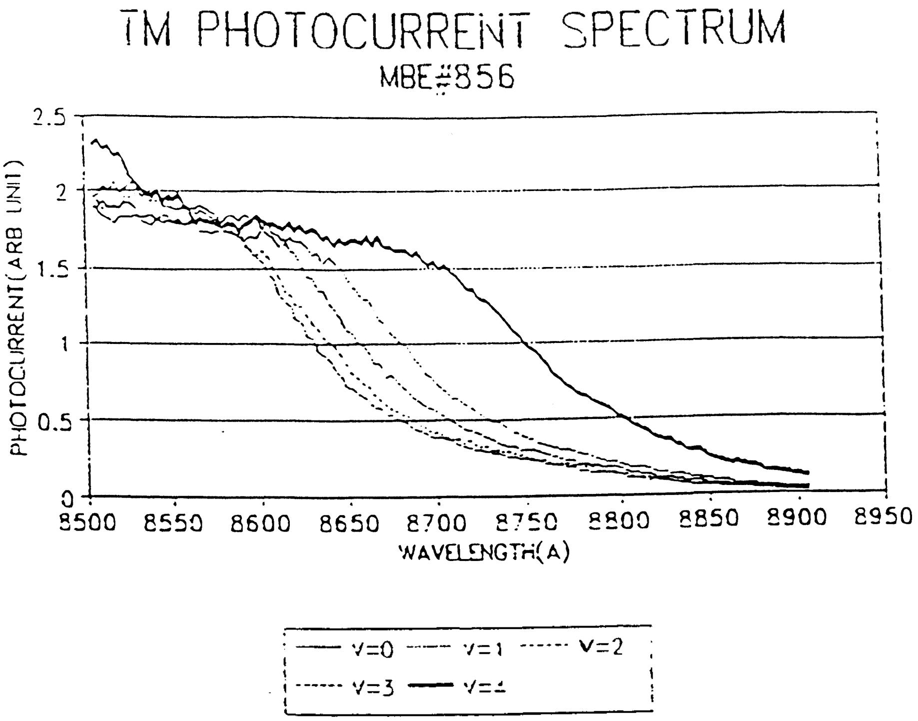

Figure 5.14- Transmission and photocurrent spectra for TM polarized light.

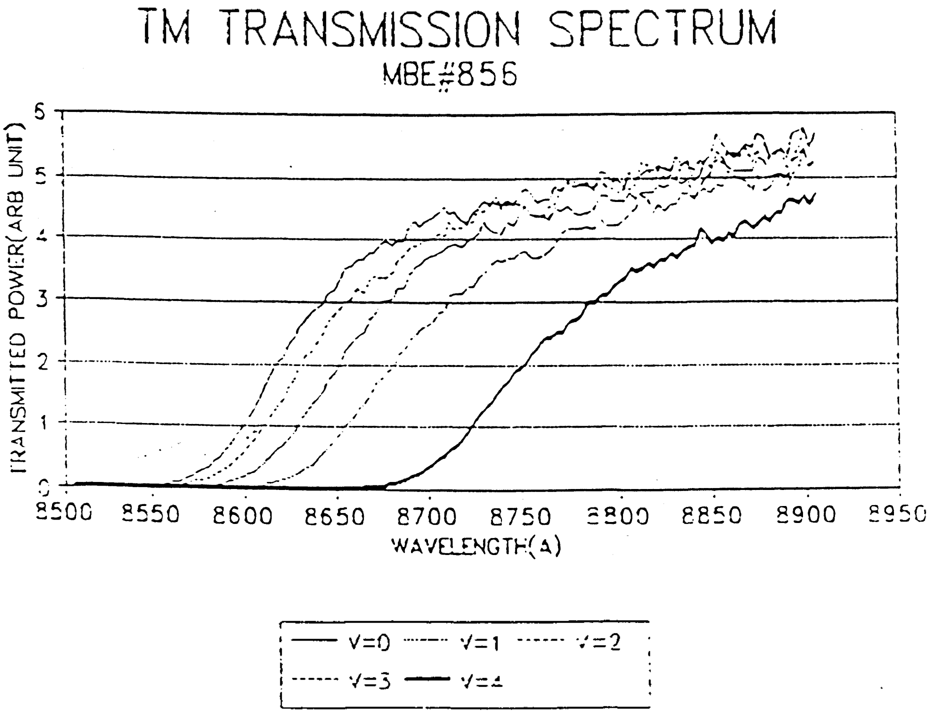

TABLE 5.3

APPLIED VOLTAGE (VOLTS)	BANDEDGE SHIFT (Å)
1	8
2	28
3	50
4	125

Figures 5.15 and 5.16 show plots of absorption coefficients calculated from transmission and photocurrent data respectively. The values of the absorption coefficients from the two separate measurements are compared in figure 5.17 for various bias voltages. Just like the TE case, it is observed that at higher wavelengths, there is a good agreement between the two values.

At shorter wavelengths the transmission values are larger. As mentioned for the TE case, the $\Delta\alpha$ values from transmission measurements are more acceptable than those from photocurrent measurements due to high absorption at short wavelength.

For the TM case no Kramers-Kronig calculations were done.

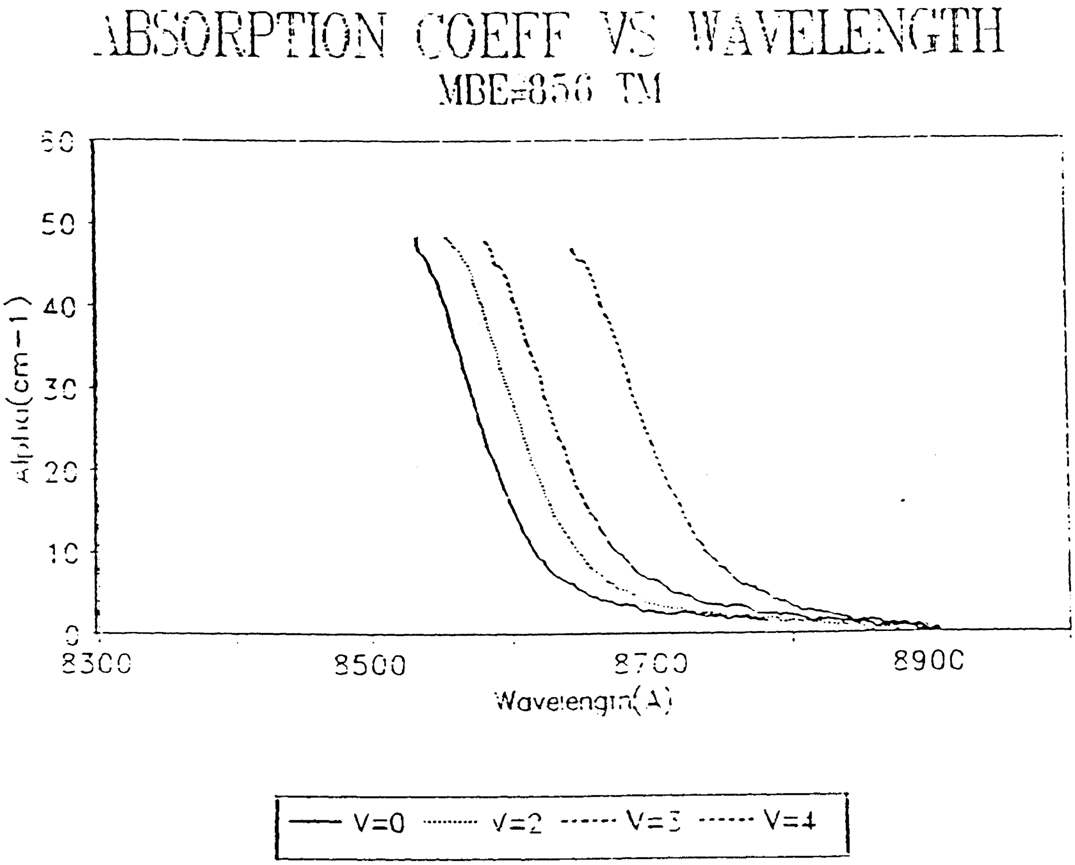

Figure 5.15- Plot of absorption coefficient calculated from transmission data.

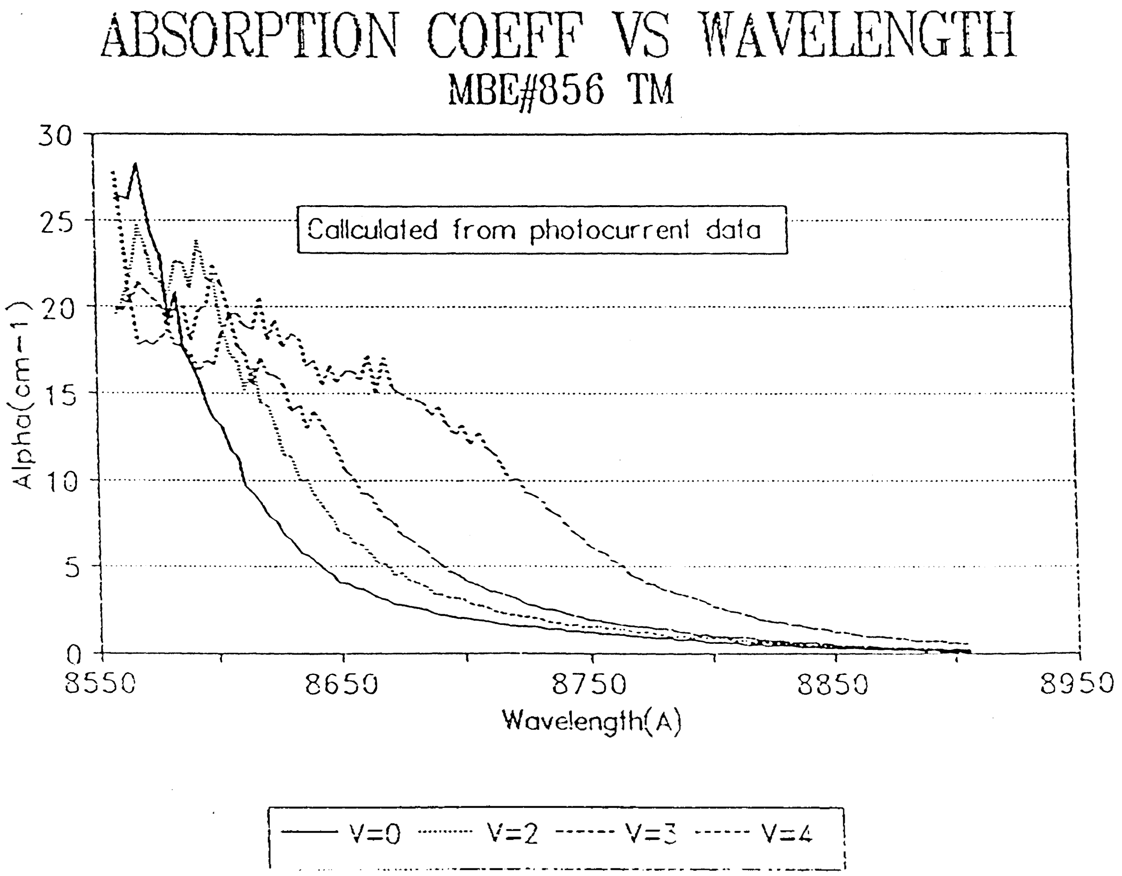

Figure 5.16- Absorption coefficient values calculated from photocurrent data for TM polarization and various bias voltages.

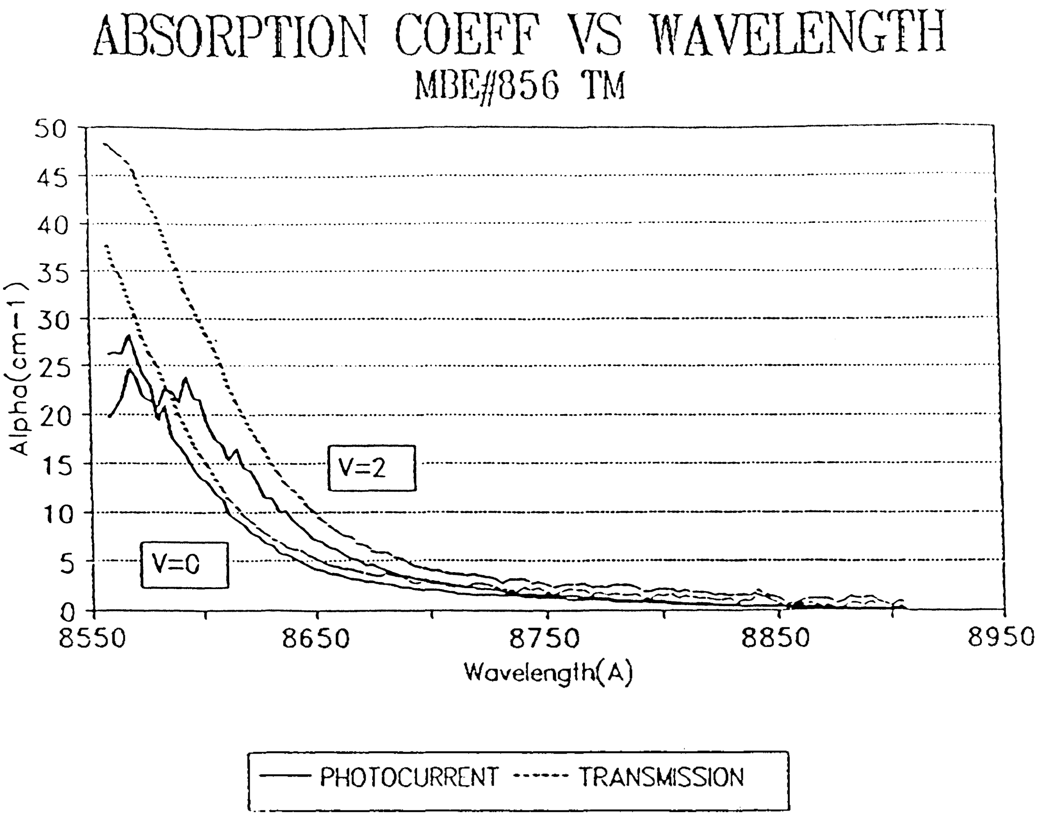

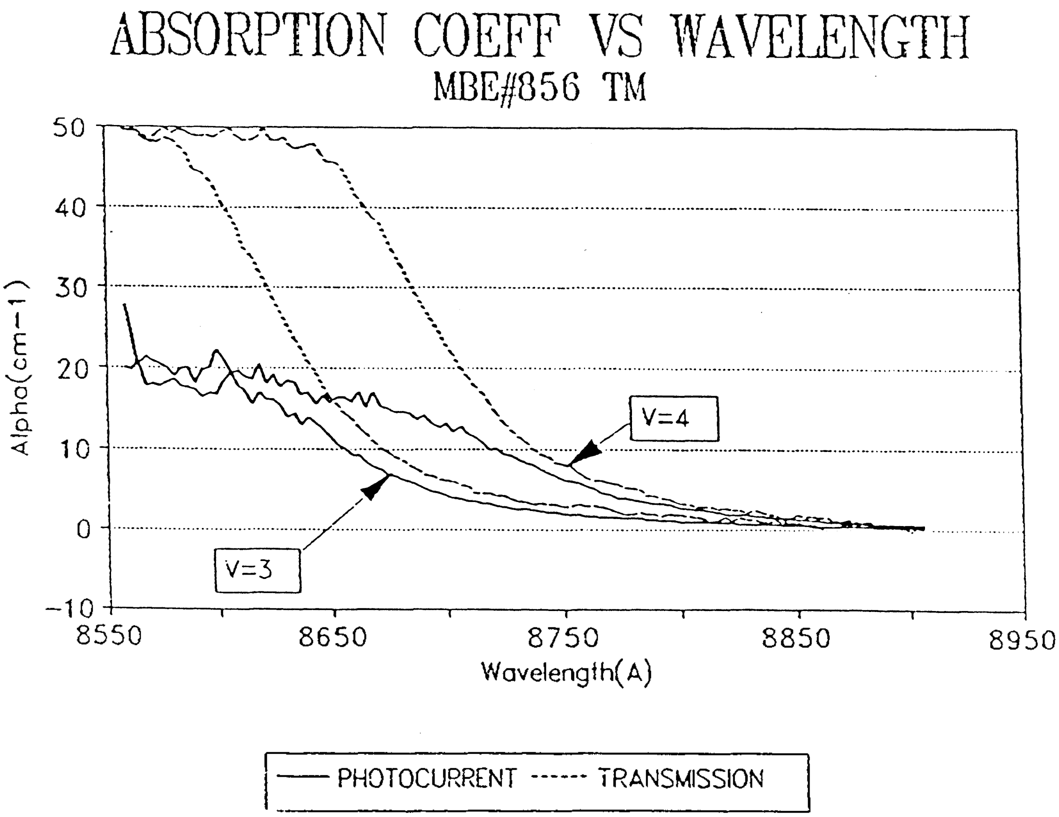

Figure 5.17- Comparison of absorption coefficient values calculated from transmission and photocurrent data at various bias voltages.

5.5- Results of phase shift measurements

We now proceed to describe the results of phase shift measurements for MBE#856.

Figure 5.18 shows the 50 MHz RF signal that has been phase shifted when bias voltages were applied to the p-i-n structure. The scope trace shows the phase shifted signal for the operating wavelength of 871nm and bias voltages of 1 and 2 volts. The darker waveform is the phase shifted signal and the lighter is the beat signal when the sample is unbiased. As is clear from these waveforms the higher the voltage the larger would be the phase shift. The phase shift was observed as a lateral movement of the waveform across the scope screen and was measured directly from the scope trace.

Several measurements were taken for both TM and TE polarized lights and the results are plotted in figures 5.19 and 5.20. These measurements were all taken for a 1.5mm long sample.

The phase shift of a phase modulator is related to the refractive index by the following relation[13]

$$\Delta\Phi = \frac{2\pi}{\lambda}\Delta n_{eff} L \qquad (5.5)$$

where Δn_{eff} is simply equal to $\Delta n\Gamma$, Γ being the confinement factor. This relation is valid when the field is uniform over the waveguiding region which is the case for a practical undoped waveguide[13]. Hence changes of $\Delta\Phi$ can be directly

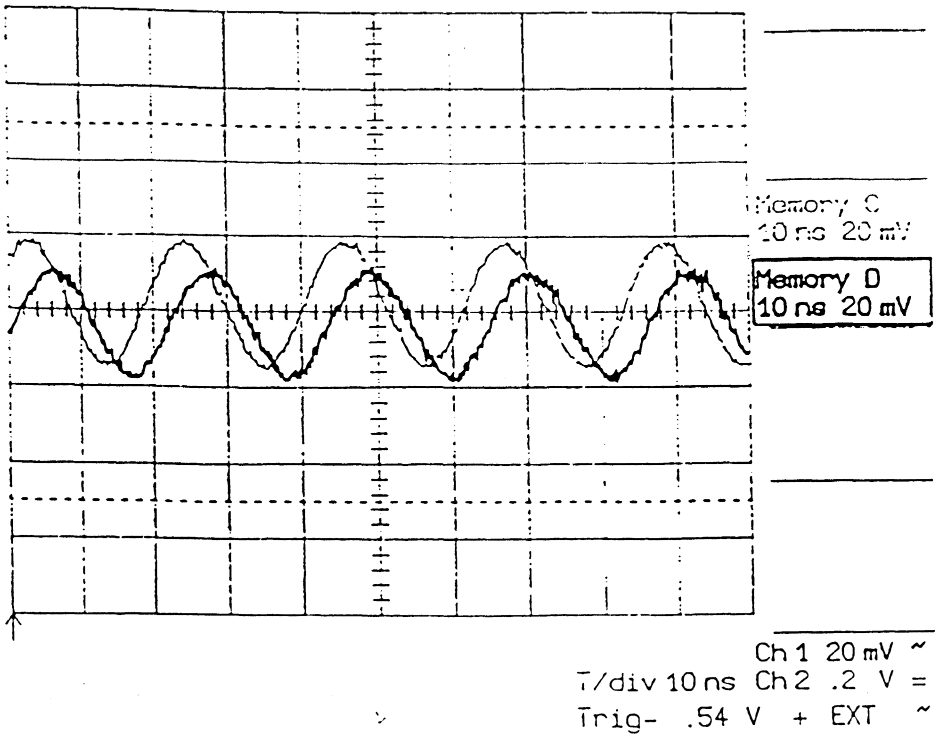

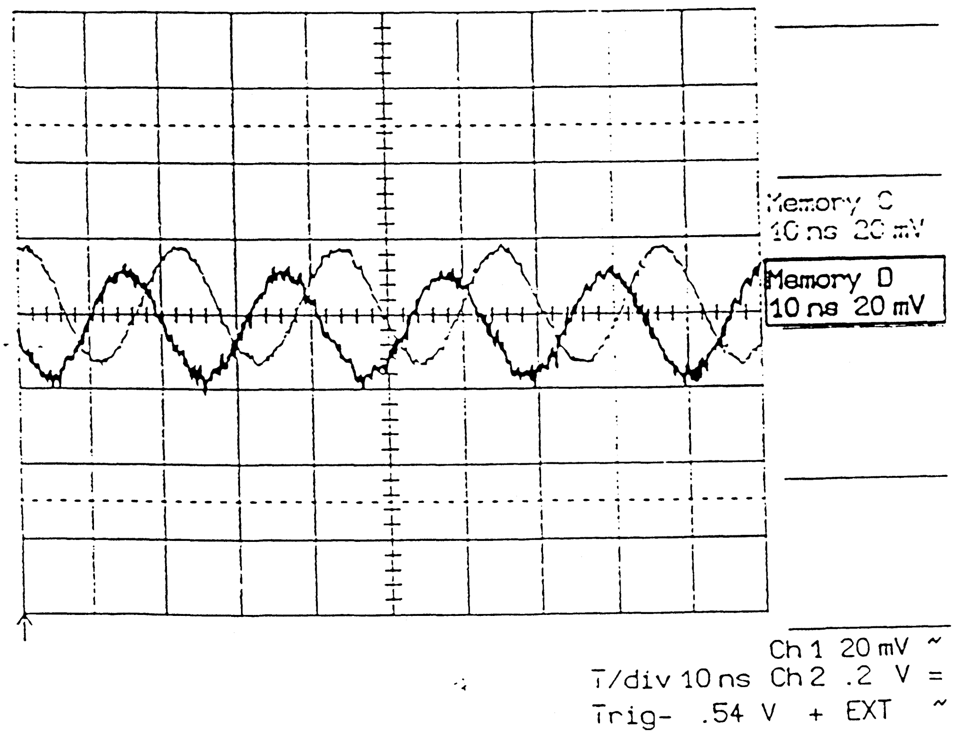

Figure 5.18- Scope trace for electrorefraction phase shift measurements for λ=871nm, V=1 and V=2.

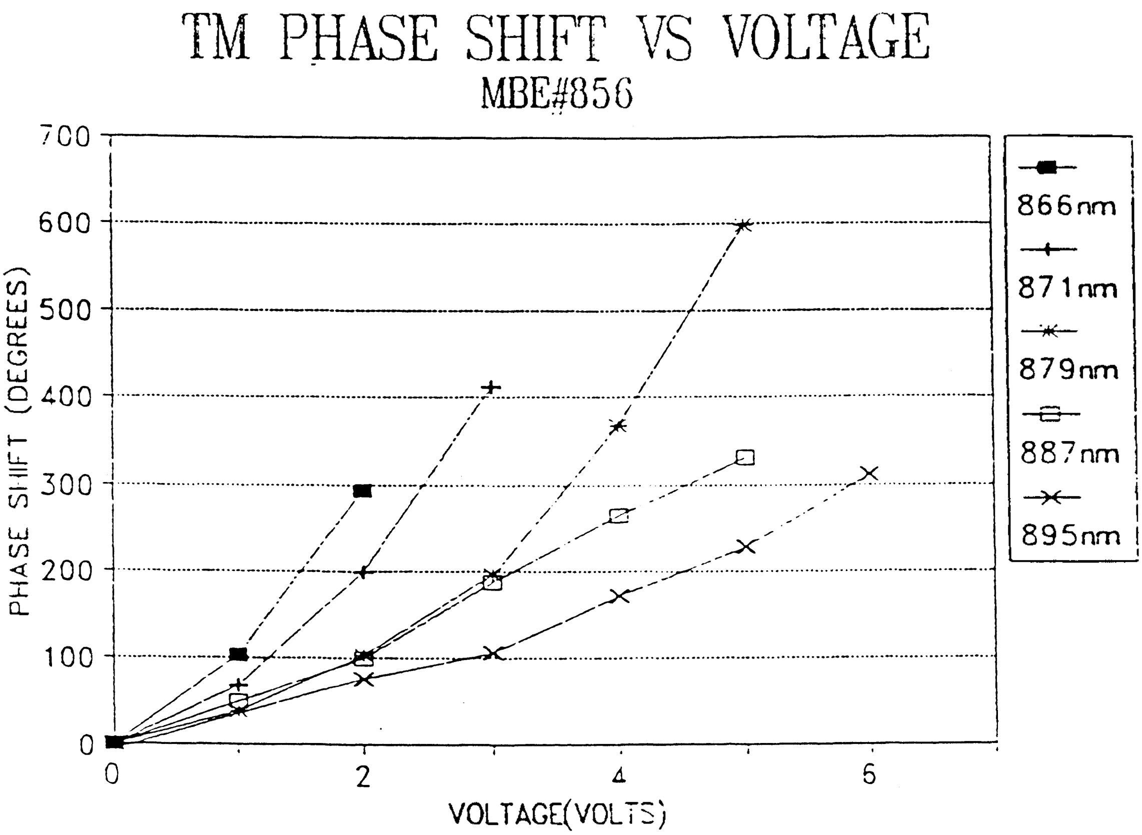

Figure 5.19 -TM phase shift vs voltage for 1.5mm long sample.

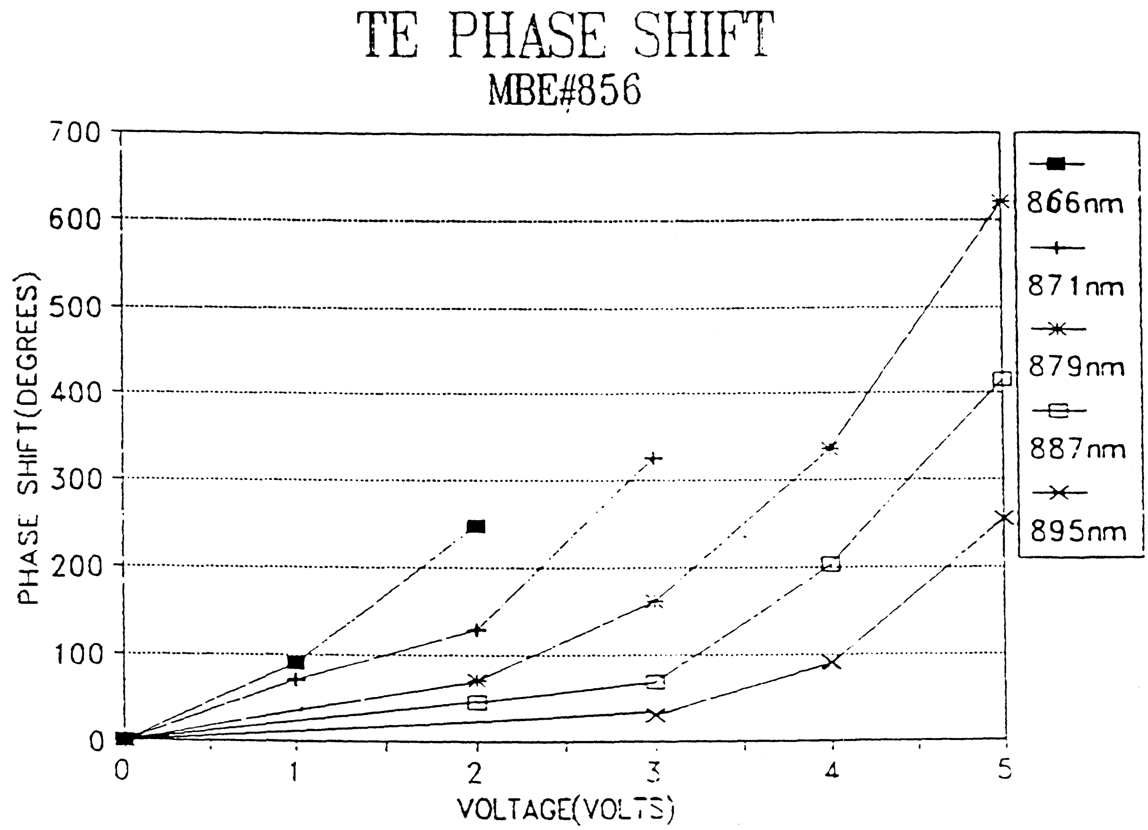

Figure 5.20 -TE phase shift vs voltage for 1.5mm long sample.

converted to Δn change. The phase change values were taken directly from figure 5.20 and using equation 5.5 were converted to index change. Figure 5.21 shows the plot of index change vs electric field at a fixed wavelength of 879nm.

Another useful figure of merit for the phase modulator is $\Delta n/\Delta k$ [14],[6], where k is simply the extinction coefficient which is the imaginary part of the refractive index. The extinction coefficient is related to the absorption coefficient by the following relation

$$k=\frac{\alpha\lambda}{4\pi} \tag{5.6}$$

For the design of a phase modulator it is desired not only to have a large phase shift but also to have small absorption. This is due to the fact that increased absorption is an undesirable effect for the phase modulators. Therefore, it is required to have a large value of $\Delta n/\Delta k$ accompanied by a large Δn value.

Figure 5.22 shows the plot of Δn and $\Delta n/\Delta k$ vs wavelength. For wavelengths closer to the bandgap the index change is larger but also absorption is larger, hence the ratio $\Delta n/\Delta k$ is small. As the wavelength is moved further away from the bandedge, Δn values decrease but the ratio $\Delta n/\Delta k$ would increase. Hence there is a trade-off between the two and the best operating wavelength is the one that ensures both

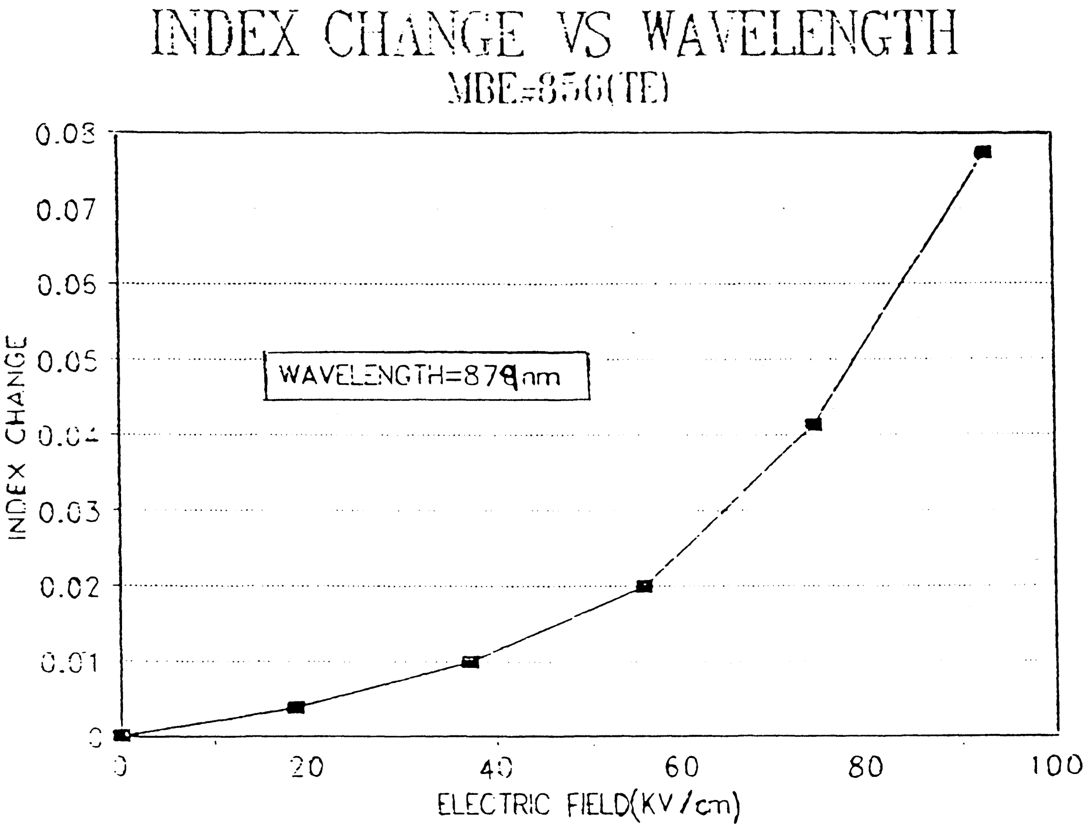

Figure 5.21 - Figure shows change of refractive index with applied electric field at a fixed wavelength of 879nm.

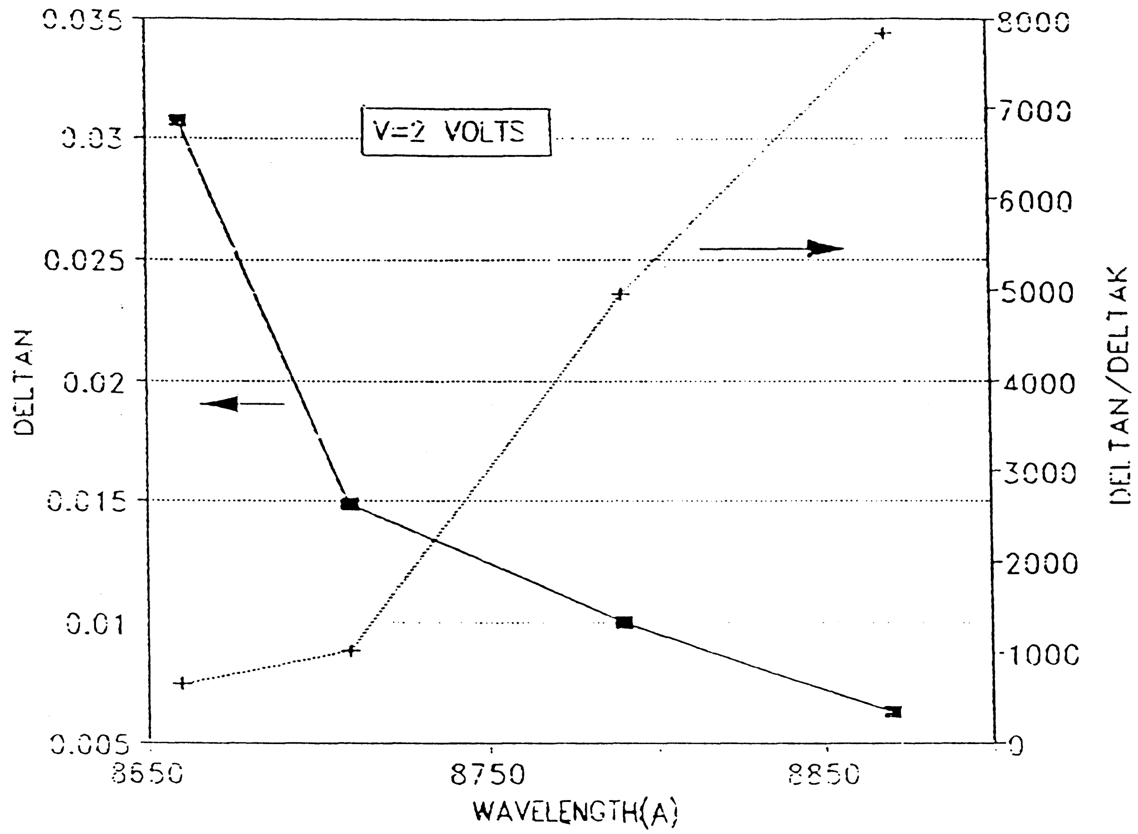

Figure 5.11-Figure shows Δn and $\Delta n/\Delta k$ curves vs voltage for a bias voltage 2 volts.

large Δn and $\Delta n/\Delta k$.

Finally, it is necessary to compare the size of the electrorefractive effect to the calculated electrooptic effect(Refer to chapter 2). For TE polarized light the normalized phase shift at 866nm for 2 volts is 83°/v.mm. This is the maximum value of the normalized phase shift for the TE polarization. At a wavelength of 879nm the normalized phase shift reduces to 27°/v.mm. These values are compared to 19°/v.mm calculated for the electrooptic effect. Hence the electrorefractive effect could be four times larger than the electrooptic effect for MBE#856.

5.6-Kramers-Kronig calculation of theoretical phase shifts

In this section a detailed Kramers-Kronig calculation is performed to calculate the field related index change from absorption coefficient change. The absorption coefficient values have been directly taken from the experimental data (for TE polarization) and no theoretical analysis for prediction of the α values was done. As mentioned in section 5.4 the working values of α were chosen from photocurrent data.

As already described in Chapter 2 the Kramers-Kronig relation is given by equation 2.8. In order to evaluate the integral Simpson's rule was used as the numerical integration method. Equation 2.8 shows that there is a singularity in the integrand. This was dealt with by noting that the sign of the integrand reverses at the singularity. By choosing a grid that places the singularity exactly at the midpoint between two grid points, we are allowed to omit that one cell from the numerical integration. The two halves of that cell have cancelling contributions.

Figure 5.24 shows the theoretical calculation for MBE#856 for TE polarized light and the results are compared with experimental values. As observed in this figure there is a good agreement between theory and experiment.

Figure 5.25 shows the same results for the InP based material. These are the theoretical predictions for a 2mm long sample.

The computer program is given in appendix 1.

5.7-Results of the forward bias pulsed mode of operation

In this section we will describe the pulsed mode of operation that was used to avoid heating effects. A scope trace of this mode of operation was already shown in figure 4-10. In that trace it was observed that the rf power to the acousto-optic modulator was pulsed. The pulse length was 2μs and its amplitude was 6 volts with a duty cycle of 1/100.

The voltage pulses are synchronized to occur near the

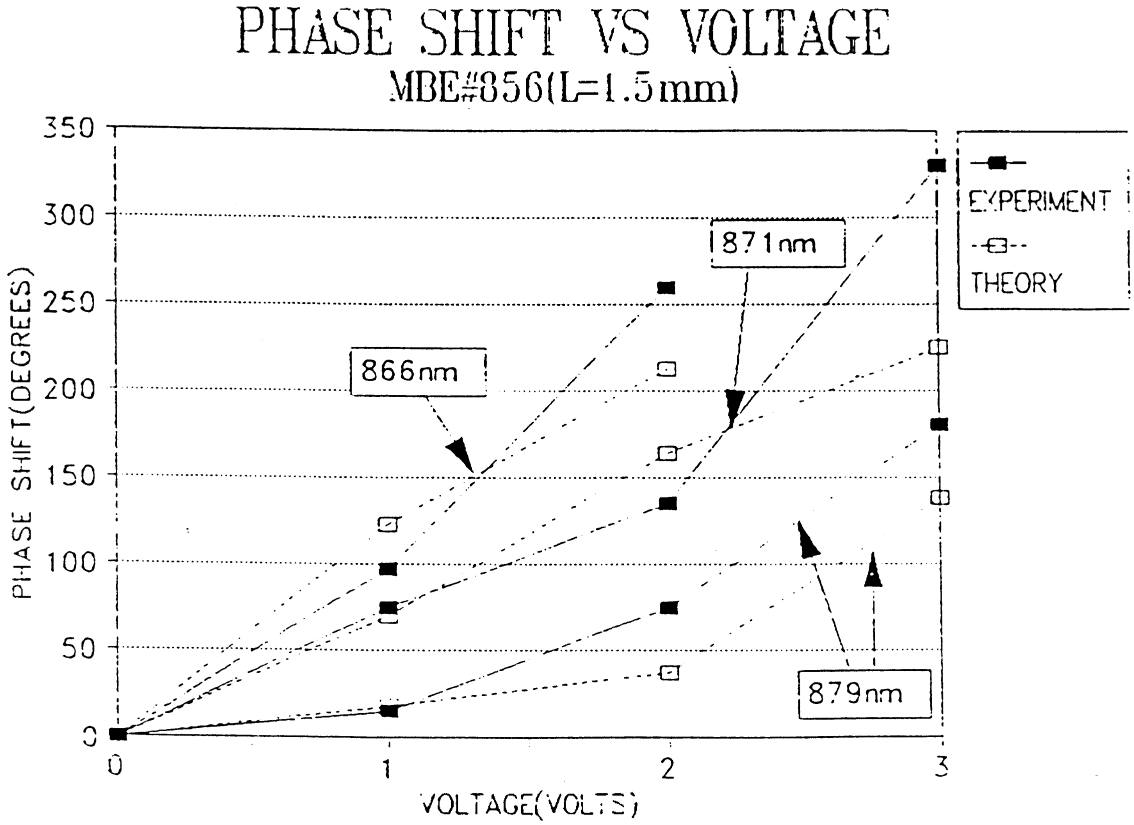

Figure 5.24 Experimental results from phase shift measurements are compared with theoretical results from Kramers-Kronig relation for a 1.5mm long sample and TE polarized light.

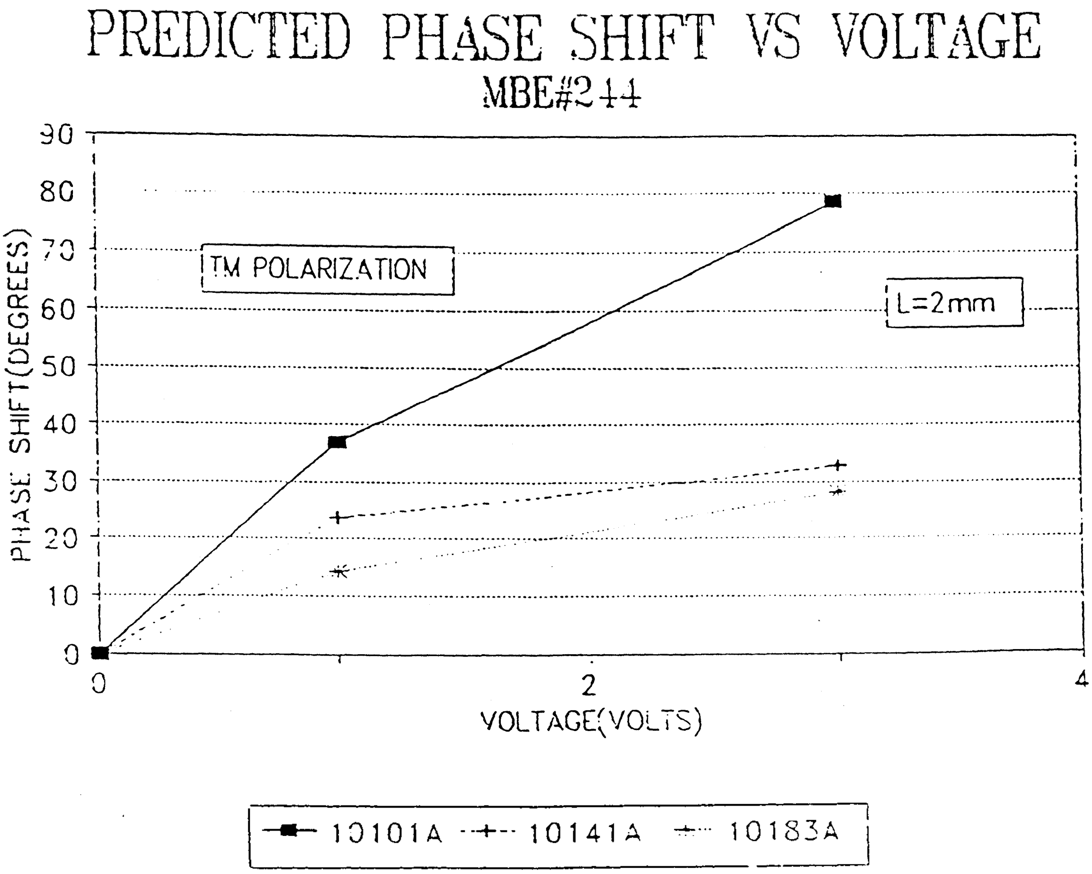

Figure 5.25- Figure shows the predicted values for phase shift for a 2mm long sample and TM polarized light at different wavelengths and bias voltages.

middle of light pulses. As observed in the figure the intensity modulation occurs since the DC light level changes during the voltage pulse. In this case we are interested in phase modulation. As voltage increases the R.F phase is seen to shift only for the "voltage on" part of the light pulse. Zero voltage parts show no phase shift. Hence it was concluded that there was no significant heating.
The "voltage on" part of the light pulse was magnified on the scope and the phase shift measurements were made by changing the amplitude of the low duty cycle pulse applied directly to the sample(refer to figure 4.9). Various measurements were taken at different bias voltages and wavelengths and the results are plotted in figure 5.26. In this figure it is observed that, at a particular current level the phase shift decreases as one moves away from the bandgap towards longer wavelengths. The other feature is that for the same wavelength the phase shift increases with increasing current level. In order to get same phase shift, the current level should increase as one moves away from the bandgap. This is in agreement to the results obtained by Chuang et al[15] which was discussed in section 2.8.

The application of this kind of phase shifter is in devices for use as programmable delay lines in photonic switching systems[15].

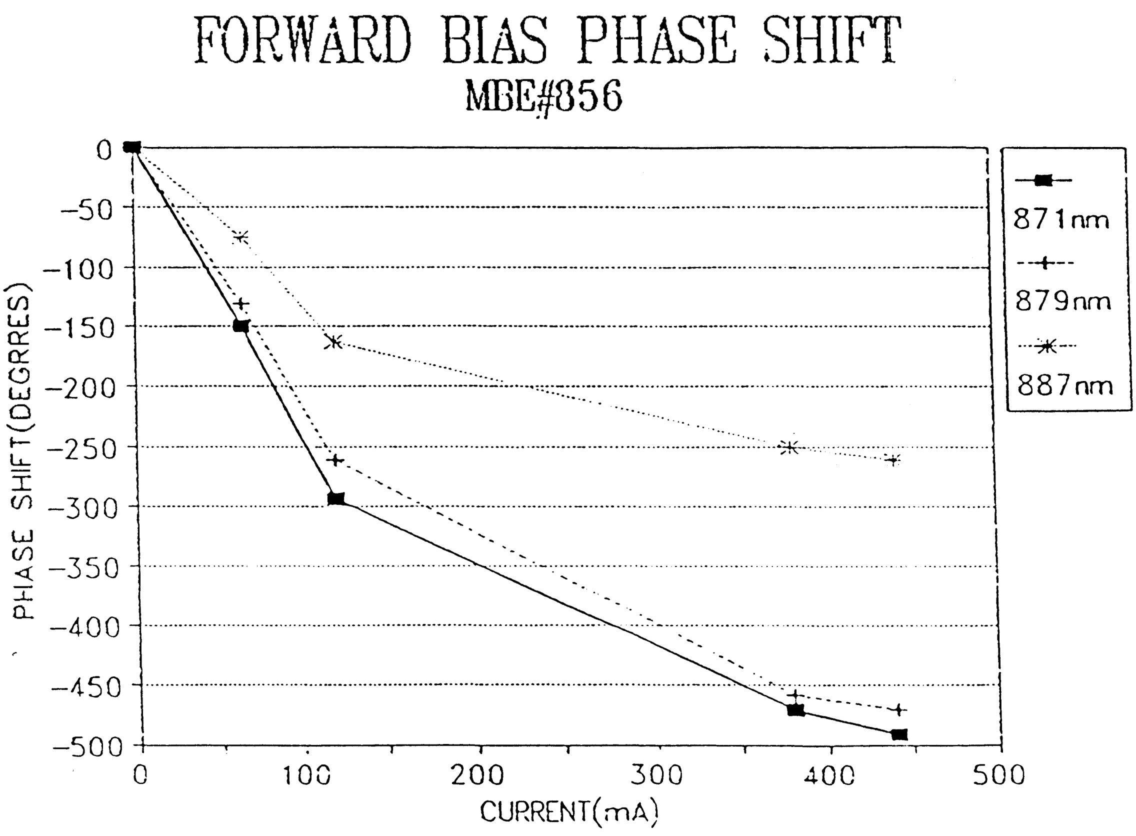

Figure 5.26- Forward bias phase shift measurement results at different current levels and wavelengths.
1.5 mm long sample - TE polarized light

5.8-Lasing operation of MBE#856

One of the interesting experimental results which was obtained for MBE#856 was its lasing operation. As mentioned earlier for this particular sample processing has been done to make rib channels in the waveguide structure (Processing done by Dr Doug Bruce, the research engineer of the group). The channels were typically $3\mu m$ and $10\mu m$ wide. Making channels in this structure causes better carrier confinement and hence lasing operation was expected. Since the active layer of this structure is $.538\mu m$ thick, it is far from being an optimum laser structure.

In order to demonstrate laser operation, a forward bias pulse of amplitude 20V was applied to the sample through a 50Ω resistor and the amplitude was gradually increased. The sample was carefully observed under the microscope with an I.R viewer and at about 30V it started to glow. This glow was obviously due to LED operation since the emanated light had a low intensity and was not uni-directional. At about 40v the emitted radiation suddenly became intense and was observed to be emerging out of the two cleaved edges in a unidirectional way. This was definitely a lasing operation and in order to verify this, the input current was varied and the voltage drop across the 50Ω input resistor was measured from which the input current could be calculated. The intensity of the emitted light was also measured by a photodyne detector and the results are plotted in figure 5.27. The sample contained

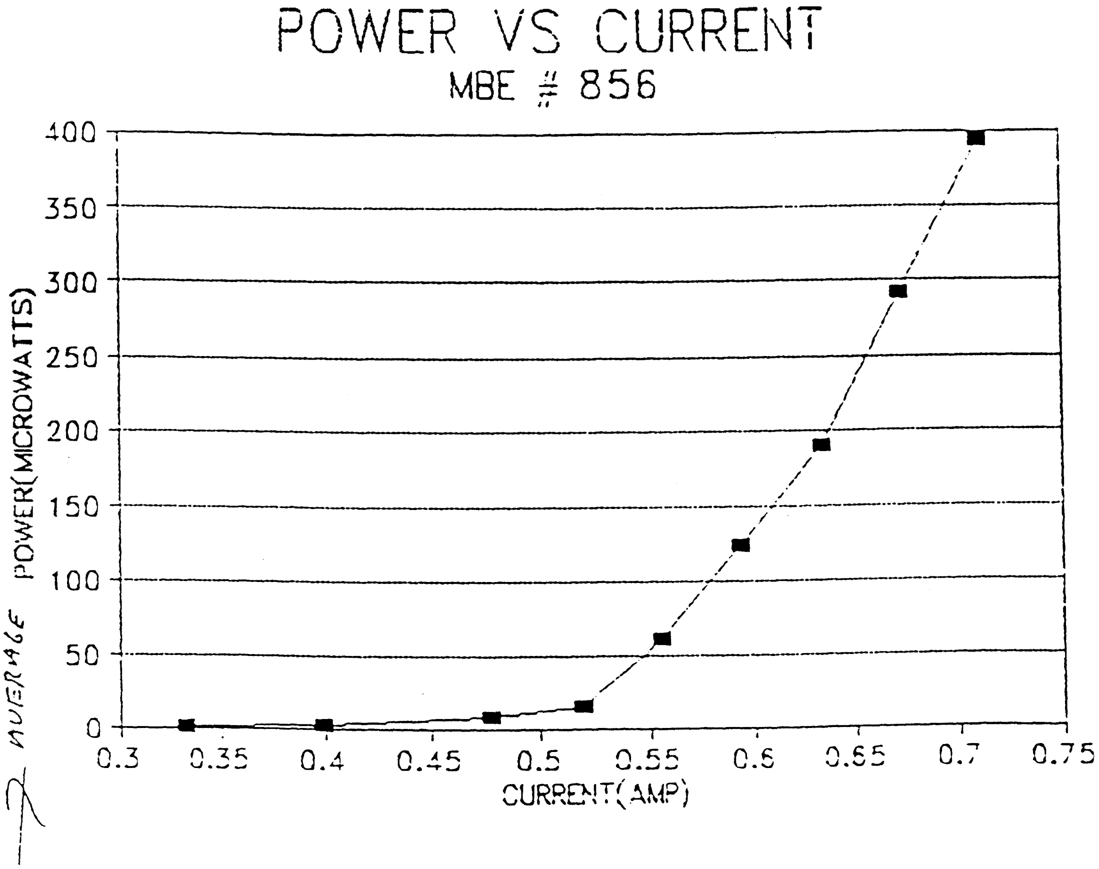

Figure 5.27 The L-I curve depicts the lasing operation for the rib channel waveguide made of MBE#856.

four channels in parallel and the drive current was distributed among all of them. This L-I curve shows that the threshold occurs at about 500 mA and since the duty cycle of the input pulse was 1/100, the power during the light pulse was 40mW.

Next the emitted radiation was directed towards the entrance slit of the monochromator to find the wavelength of emission. A Silicon detector was placed in front of the exit slit and the monochromator was scanned about the wavelength corresponding to the most intense radiation. The output of the detector was recorded by a chart recorder and the results are shown in figure 5.28. As seen in this recorded output the peak of the emitted radiation occurs at 8662Å which is close to the bandgap wavelength of the GaAs well. The spectral width of this profile is 15Å. This narrow spectral width indicates lasing.

Furthermore, the output of the detector was sent to a scope and the wavelength was scanned about the peak position to observe the modes of this laser. For the 1.5mm long sample the modes were not resolvable.

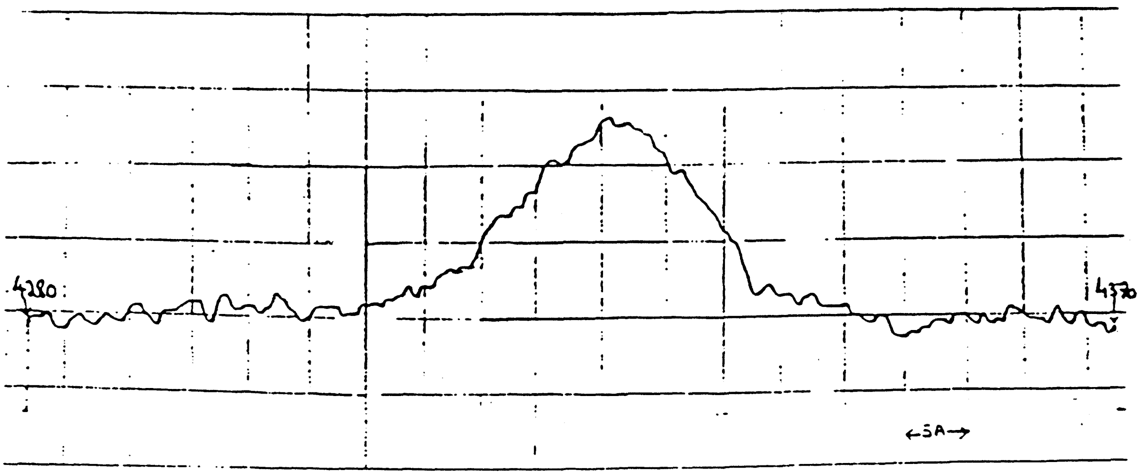

Figure 5.28 - The spectral profile of the emitted laser light.
The FWHM is nearly 15Å.

5.9- Figures of merit

One of the important figures of merit for a waveguide modulator is the insertion loss which is defined as the ratio of output power to the incident input power.

For MBE#856, first the input power and then the light coming through the waveguide were measured. But this ratio would not give the real insertion loss unless the effect of the loss in the input-output microscope objectives are taken into account. Hence, the sample was removed from the space between the two objectives and the input and output powers were measured. To calculate the insertion loss, the ratio of waveguide output to incident power was multiplied by input/output power with the sample removed. The results for operating wavelength of 8700Å are tabulated in table 5.4.

TABLE 5.4

Input power (μW) I_{in}	Waveguide output power (μW) I_{wg}	Output power with sample removed (μW) I_{out}	Insertion loss 10 Log[(I_{wg}/I_{in})(I_{in}/I_{out})] (dB)
670	12	253	13.2

One important figure of merit for an intensity modulator is the extinction ratio which is defined as the ratio of the switched intensity by the zero bias intensity at the same wavelength[11]. The extinction ratio is nearly one at short wavelengths and drops to zero at longer wavelengths. The high extinction ratio at short wavelengths (close to one), comes at the expense of high insertion loss and hence there is trade-off between the two.

In order to find the best operating wavelength for the modulator, another figure of merit has been defined which is called the modulation parameter. The modulation parameter is defined as the ratio of the switched intensity at a particular wavelength by the maximum possible transmitted intensity at very long wavelengths[11]. Figure 5.29 shows the plot of modulation parameter vs wavelength for a 4 volt bias voltage. This plot shows that the optimum operating wavelength for this modulator is around 8700Å where the modulation parameter is maximum.

Table 5.5 lists the figures of merit of MBE#856 at different wavelengths and bias voltages. The $\Delta\alpha$ values were calculated from figure 5.9. It is observed that on/off ratios (Defined as 10 log ($e^{\Gamma\Delta\alpha L}$)) of up to 18 dB are obtained at operating wavelength of 8700Å. This is comparable to an InGaAs/GaAs MQW modulator (20dB)[10] and is higher than that of a bulk AlGaAs/GaAs electroabsorption modulator (13dB) [11].

TABLE 5.5

λ Å	length mm	on/off ratio dB	Γ	$\Delta\alpha$ cm-1	drive voltage volts	insert-ion lossdB
8700	1.5	11.1	.74	23	4	13.2
8700	1.5	18.3	.74	38	5	13.2
8675	1.5	16.9	.74	35	4	—
8750	1.5	9.6	.74	20	5	—

The insertion loss was just measured for 8700Å and for the other two wavelengths (8675Å and 8750Å), no measurements were made.

5.10- Summary of results and conclusions

In this section the results of this chapter are summarized and conclusions are given for the whole thesis. The investigation of this thesis research was on electroabsorption and electrorefraction effects in 2 materials which were MQW waveguides. Photocurrent and transmission measurements were performed on these materials and the effect of TE and TM polarizations were investigated. It was observed that in both materials the TE transmission onset was red shifted with respect to TM. The reason for this red shift was described in terms of light-hole heavy-hole transitions. It was also observed that the absorption edge shifts with the applied voltage which is the manifestation of Quantum Confined Stark Effect.

MBE#244 did not show good switching ratios as observed in the transmission spectrum. The waveguiding was also quite diffuse. The only interesting feature about this material was the large red shift of the absorption edge for the TE polarized light compared to TM. This large red-shift is probably due to the fact that the material is strained.

For MBE#856, on/off ratios of up to 18dB were measured at 8700Å for a 5 volt drive voltage. The absorption coefficients were calculated from both transmission and photocurrent measurements and they were compared to each other and found to be in good agreement. The absorption coefficient values calculated from transmission data were chosen as working values for Kramers-Kronig calculations.

For the electrorefraction part the phase shift measurements were made for MBE#856 using a Mach-Zehnder interferometer and an acousto-optic modulator which produces a 50MHz beat note. Normalized phase shifts of upto 83°/v.mm were found which makes MBE#856 a suitable phase shifter which can be used in integrated optics application.

Kramers-Kronig calculations to find the index change values, using the experimental values of the absorption coefficient showed a good agreement with the measured phase shift results.

A pulsed method of operation was used to measure the forward bias phase shifts. The results were in agreement with a previous work done by Chuang[15].

It was found that a rib channel waveguide processed from MBE#856 lases on forward bias. The L-I curve and the spectral profile of the emitted radiation were plotted and the wavelength of emission was found to be 8662Å with a FWHM of 15Å.

Finally, the figures of merit were calculated which included the insertion loss and the on/off ratio. No measurements for the electrical bandwidth of the modulator were performed.

In conclusion, it was found that MBE#856 could be used as an intensity modulator, a phase modulator, a laser, and a switch and is a useful material for integrated optics applications.

To suggest further work, one can use the absorption coefficient and the phase shift data to design a dual channel coupler and investigate its switching behaviour. This switching can be checked by employing coupled mode theory.■

APPENDIX 1

PROGRAM KRAMERS KRONIG

```
C       Program to calculate the refractive index change from absorption
C       coefficient data by evaluating the Kramers-Kronig integral.
        READ(4,*)L,LAMBDA,N,h,GAMMA
C       L=Length of the sample
C       LAMBDA=Wavelength for which the index change is calculated
C       N=Total number of data points between two chosen wavelength
C       on either side of the bandedge such that deltaalpha values are
C       zero.
C       h=Step size.
C       GAMMA=Confinement factor
        DIMENSION  WL(N),DELA(N),Z(N)
C       WL(N) and DELA(N) are wavelength and change of absorption
C       coefficient values for a particular bias voltage respectively.
        DO 77 I=1,N
        READ (5,*) WL(I),DELA(I)
  77    CONTINUE
        DO 88 J=1,N
C       Refer to the form of Kramer-Kronig integral
        X(J)=WL(J)/LAMBDA
        Z(J)=DELA(J)/(1-X(J)**2)
  88    CONTINUE
C       Sympson's rule was used as the numerical integration method.
C       This rule is given by
C       I=h/3[Y0+4Y1+2Y2+.......+4YN-1+YN]
C       If total number of data points is even,there will be equal number
C       of terms with 2 and 4 as a coefficient.
        K=N/2-2
        SUM1=0
        DO 90 I=1,K
        X1=2*Z(2*I+1)
  90    CONTINUE
        SUM2=0
        DO 91 I=1,K
        X2=4*Z(2*I)
  91    CONTINUE
        SUM=Z(1)+X1+X2+Z(N)
        PIE=3.14
        DELTAN=h/3*SUM/PIE
        DELTAPHI=2*PIE/LAMBDA*DELTAN*GAMMA
        PRINT *,DELTAN,DELTAPHI
        STOP
        END
```

LIST OF REFERENCES

1) Jones,W.B "Optical Fiber Communication Systems", Holt,Rinehart and Winston,Inc. New York, 1988.

2) Yariv,A "Optical Electronics", CBS College Publishing. Japan, 1985.

3) Ghatak,A.K and Thyagrajan,K "Optical Electronics", Cambridge University Press, 1989.

4) Hunsperger,R.G "Integrated Optics, Theory and Technology", Springer-Verlag, New York, 1982.

5) Lee,D.L "Electromagnetic Principles of Integrated Optics", John Wiley & Sons, Inc.,1986.

6) Zucker et al "Electrooptic phase modulation in GaAs/AlGaAs quantum well waveguides". Apply Phys lett 52 (12) 1988.

7) Rod Alferness "Waveguide electrooptic modulators". IEEE transaction on microwave theory and techniques vol MTT-30, No 8, August 1982.

8) Mendoza-Alvarez et al "Analysis of depletion edge translation lightwave modulators". Journal of lightwave technology,vol 6,no 6,June 1988.

9) Mike Daly's Master's thesis.

10) Neil Hunt's PhD thesis.

11) Chippindale's Master's thesis.

12) Walpita,L.M. "Solutions for planar optical waveguide equations by selecting zero elements in a characteristic matrix". Journal of optical society of America. A-2

13) Alping and Coldren "Electrorefraction in GaAs And InGaAsP and its application to phase modulators". J.Appl Phys,Vol 61,No 7, 1 April 1987.

14) Zucker et al " Quaternary quantum wells for electrooptic intensity and phase modulation at 1.3 and 1.55 μm". Apply Phys letters 54(1) 1989.

15) Chuang et al " Current controlled GaAs/AlGaAs MQW phase shifter operating at .9 μm ". Apply Phys.Lett. 59 (19) 1991.

16) Rolland & Mac "High speed bulk InGaAsP-InP electroabsorption modulators with bandwidth in excess of 20 GHz".
IEEE photonics technology letters,vol 2 no 10,1990.

17) Pell,C. "Phased Array Radar", Microwave Exhibitions and Publishers LTD, 1988.

18) Simonis et al " Optical control of microwaves with III-V semiconductor optical waveguides".
IEEE transactiona on microwave theory and techniques, vol 38, no 5, 1990.

19) Wood, T.H. "Multiple Quantum Well waveguide modulators" Journal of lightwave technology.Vol 6. No 6. June 1988.

20) Simonis et al "Optical control of microwave with III-V semiconductor optical waveguides".
Optoelectronic signal processing for Phased Array Antennas II(1990).

21) Tamir,T. "Integrated Optics", Springer-Verlag, 1979.